SHOCK TUBE INVESTIGATIONS OF STRONG SHOCK WAVES IN A CONVERGENT CHANNEL

Thesis by

Robert Earle Setchell

In Partial Fulfillment of the Requirements

For the Degree of

Doctor of Philosophy

California Institute of Technology

Pasadena, California

1971

(Submitted May 28, 1971)

ACKNOWLEDGMENTS

The present research was conducted under the guidance of Professor Bradford Sturtevant, whose insight and encouragement have been sincerely appreciated. In addition, his constructive criticism of the original manuscript led to numerous improvements.

The author wishes to thank Mr. Erik Storm for providing the axisymmetric diffraction solution, and Mrs. Ellen Cummings for typing the original manuscript. It is a pleasure to thank Mrs. Jacquelyn Beard for typing the final manuscript.

The author is indebted to the National Science Foundation for its financial assistance. The work in the GALCIT six-inch shock tube was supported by the National Aeronautics and Space Administration.

Special thanks go to my wife Judy, whose patient sacrifices made this undertaking possible.

ABSTRACT

The behavior of the incident and reflected shock waves in a convergent channel is investigated in order to determine if such a geometrical device could be used as a means of producing high-enthalpy gas samples. A 10^{o} half-angle conical convergence is mounted on the end of a pressure-driven, six-inch shock tube. Using argon at an initial pressure of 1.5 torr, initial shock Mach numbers are varied from 6.0 to 10.2. During each run local shock velocities at several positions along the cone axis are measured using a small, multi-crystal, axial piezoelectric probe inserted from the cone vertex.

The incident shock velocity profiles show that the shock behavior is dominated by multiple diffraction processes which originate at the cone entrance. Sudden increases in shock velocity at certain positions along the axis are observed, corresponding to the intersection of stemshocks formed by Mach reflection on the cone wall. These increases are separated by regions of deceleration and acceleration, corresponding to the growth and decline of a center shock formed by Mach reflection on the cone axis. Near the vertex the shock velocity has increased by as much as a factor of three, indicating that high temperatures and pressures are generated. By varying the initial Mach number and pressure, real gas effects are found to

influence the diffraction process only in a region near the vertex.

Reflected shock profiles show that the shock velocity is nearly constant for much of the convergence length, in contrast to the power-law decline predicted by the similarity solution. During this period the shock propagates into fluid originally set into steady, uniform motion outside the cone entrance. Small variations in the velocity result from weak interactions with localized nonuniformities and secondary waves. Beyond the cone entrance the shock decelerates towards the velocity corresponding to reflection from a plane end wall. A departure from ionization equilibrium is likely near the vertex during the rapid expansion which occurs behind the reflected shock.

TABLE OF CONTENTS

TABLE OF CONTENTS (cont.)

TABLE OF CONTENTS (cont.)

TABLE OF CONTENTS (cont.)

LIST OF FIGURES

LIST OF FIGURES (cont.)

I. INTRODUCTION

For the past quarter century the shock tube has been the primary experimental tool for studies of gases at elevated temperatures. When investigators found that the temperatures required for certain areas of interest involved shock waves too strong to be generated in conventional pressure-driven shock tubes, a number of modifications were introduced.* Most were techniques for heating the driver gas, either by an internal electric discharge, by shock heating (multiple diaphragm shock tube), or by combustion of dilute mixtures of hydrogen and oxygen. An alternate approach used a sudden reduction in the shock tube cross-section, located either at the diaphragm station in order to accelerate the driver gas, or at some position in the test section in order to accelerate the shock wave directly. The introduction of explosively-driven and electromagnetically-driven shock tubes resulted in the production of very strong shock waves.

For most of this period of shock tube development it has been known that shock waves propagating through gradually converging channels tend to strengthen. The flow generated in such a channel is nonuniform and unsteady, and presumably these limitations account for the scarcity

---

*Descriptions of the various modifications, along with corresponding references, can be found in Chapter IV of Reference 1.

of experimental investigations into this behavior. However, the simplicity of a geometrical approach, together with recent interest in nonequilibrium radiation phenomena involving unsteady conditions, indicate that this method of shock strengthening requires further study.

1.1 Motivation for Generation of Strong Shock Waves

Although the shock tube was pioneered by Vieille in 1899 (Ref. 2), modern application of the device began during the Second World War when it was used to calibrate piezoelectric gauges designed for blast wave studies (Ref. 3). Following the war, the shock tube proved useful in studying the reflection of shock waves at oblique surfaces (Refs. 4, 5). Extensive use of the shock tube began in the early 1950's, when experimentalists realized its potential for investigation of high temperature kinetics. The basic appeal of the instrument was the sudden temperature rise associated with the shock front. Through propagation of a plane shock wave of moderate Mach number, a volume of test gas can be heated homogeneously to a temperature of several thousand degrees in a time much less than a microsecond. Since the different degrees of freedom available to gases at high temperatures approach equilibrium at different rates, the shock tube provided a method for studying the various mechanisms for energy

transfer which occur in relaxation phenomena.* Through use of appropriate gas mixtures, chemical reaction rates under the uniform conditions existing behind plane shocks have been measured. The shock tube also has proved useful in investigating thermodynamic properties and equations of state of high temperature gases.

With the production of stronger shock waves the shock tube became a basic tool for the study of radiation physics. Emission and absorption spectra from molecules, atoms, and ions have been measured. Relative and absolute measurement of spectral intensity has provided information on atomic constants and energy levels, transition probabilities, and Stark and Zeeman constants. Gasdynamic processes involving radiative heat transfer, such as the propagation of very strong shock waves (Ref. 8), have been studied. Of more recent interest is the investigation of radiation from gas samples in which significant sustained departures from equilibrium occur. Such samples can be produced through a rapid expansion of shock-heated gas (Refs. 9, 10).

---

*A multitude of shock tube investigations have been reported during the past twenty years. Reviews of measurements not specifically referenced, together with extensive bibliographies, can be found in References 1, 6, and 7.

1.2 Theoretical Solutions for Shock Wave Strengthening in Converging Channels

1.2a Similarity Solution

A similarity solution for the motion of a converging cylindrical or spherical shock wave was obtained in 1942 by Guderley (Ref. 11). In 1954 Butler (Ref. 12) reworked the Guderley solution with improved computational methods and greater emphasis on the reflected shock wave generated by the collapse of the converging shock. The solution assumes that as the shock wave propagates into a uniform, stationary perfect gas its strength continuously increases. When the shock wave collapses on the axis or point of symmetry its strength is singular. Taking the symmetry axis or point to be the origin, then in some neighborhood of this origin the shock wave is sufficiently strong for the pressure and temperature of the gas ahead of the shock to be considered negligible compared with those properties behind the shock. Assuming that this neighborhood is small compared with the dimensions of whatever mechanism generated the shock wave initially, then there are no dimensional parameters in the problem with which to form length or time scales, and only one parameter with the unit of mass (the initial gas density). Consequently the problem can be described as a self-similar motion of the second kind.*

*A discussion of conditions for self-similar motion can be found in Chapter XII of Reference 13.

The solution takes the form

$$u = \frac{r}{t} f(\xi) \quad , \quad p = \rho_o \frac{r^2}{t^2} g(\xi) \quad , \quad \rho = \rho_o h(\xi) \qquad (1)$$

where r is the distance measured from the origin, t is time measured from the instant the converging shock collapses, u is fluid velocity, p is fluid pressure, ρ is fluid density, and ρ_o the initial density. ξ is the similarity variable given by

$$\xi = - \frac{t}{B r^{1/\alpha}}$$

where α is a dimensionless similarity exponent which remains to be determined, and B is a dimensional constant which depends on initial conditions (in the similarity regime the motion has "forgotten" the details of its origin, thus a numerical value for B cannot be found from the equations in similarity form). The converging shock wave is given by $\xi = -1$, thus the shock velocity obeys the power law

$$\text{shock velocity} = \frac{\alpha}{B} r^{-(1-\alpha)/\alpha}$$

The expressions given in (1) are substituted into the unsteady equations of motion (either cylindrically or spherically symmetric) and a set of ordinary differential equations are obtained for f, g, and h. When the

equations are numerically integrated for increasing ξ using the shock conditions at $\xi = -1$ and an arbitrary value of α, a singularity is encountered at a critical value of ξ which corresponds to the characteristic passing through the origin $r = t = 0$. Determination of a unique value for α which eliminates this singularity results in a solution for the flow field between the incident and reflected shock waves.

The reflected shock motion is also assumed to be self-similar with the same similarity exponent α. Thus, the reflected shock trajectory is given by some positive value of the similarity variable, say $\xi = \beta$. To find β, it is first necessary to find solutions to the flow behind the reflected shock which satisfy the boundary condition of zero velocity at $r = 0$. This is done by rewriting the equations in terms of a new similarity variable $\eta = \xi^{-\sigma}$, then performing numerical integration for increasing η using the boundary condition at $\eta = 0$. The parameter σ is chosen so the solution remains regular at $\eta = 0$. A family of solutions results, of which only one permits a matching with the solution for the flow ahead of the reflected shock using the shock jump conditions.

Butler computed the similarity exponent α for the cylindrical and spherical cases for shocks propagating in gases with specific heat ratios of 5/3, 7/5, and 6/5.

The reflected shock position β was found for the spherical case with specific heats ratio 5/3.

1.2b Chester-Chisnell-Whitham Theory

The Guderley similarity solution applies only to cylindrical or spherical shock waves within some neighborhood of the axis or point of symmetry. During the 1950's Chester, Chisnell, and Whitham progressively developed an approximate formulation of the more general case of arbitrary-strength shocks propagating through channels with slowly changing cross-sectional areas.

Chester (Ref. 14) considered the motion of a shock wave through a channel consisting of two uniform sections of nearly equal cross-sectional area joined by a section of gradually changing area. The small area change is assumed to create only small perturbations in the flow behind the shock, and the equations of motion describing the flow can be linearized and solved exactly. The solution shows that the shock is not uniform across the channel after entering the area change, but at any time the shock strength averaged over its area is proportional to the local channel area. Thus, when the shock has passed the area change the average shock strength remains constant. Local variations on the shock surface decrease with time, and eventually a steady state condition is reached in which shock strength is uniform. The relationship between the small change δA

in the cross-sectional area A and the resulting change δM in shock Mach number M has the form

$$\frac{\delta A}{A} = - \frac{2M\delta M}{(M^2-1)K(M)} \tag{2}$$

where $K(M)$ is a slowly varying function that contains the specific heats ratio γ .

Chisnell (Ref. 15) also considered the motion of a shock through two uniform channels separated by a small area change, and by matching steady state flow regions in the distance versus time plane (retaining only terms of the order of the area change δA) an expression equivalent to (2) was obtained. He then extended the result to channels with gradual but finite area changes by taking the limit $\delta A \to 0$ in equation (2) and integrating , thus obtaining an expression in closed form between local channel area and shock Mach number. This procedure is equivalent to representing a finite area change by a series of infinitesimal area changes, and assuming that the interference between successive interactions can be neglected. In addition to the exact integration of (2), Chisnell observed that a simpler approximate relation could be obtained by treating the slowly varying function $K(M)$ as a constant and integrating (2) directly to find

$$A(M^2-1)^{1/K(M)} = \text{constant} \qquad (3)$$

This formula can be applied to converging cylindrical or spherical shocks by considering channels with areas proportional to r^j, where r is the distance of the shock from its axis or point of symmetry, and j equals 1 or 2 for cylindrical or spherical shocks, respectively. In the neighborhood of the origin where the Mach number is large, equation (3) becomes

$$r^j M^{2/K} = \text{constant} \qquad (4)$$

where K is the limiting value of $K(M)$ for very strong shocks given by

$$K^{-1} = \frac{1}{2} + \frac{1}{\gamma} + \left[\frac{\gamma}{2(\gamma-1)}\right]^{\frac{1}{2}}$$

For comparison with the similarity solution equation (4) can be written

$$\text{shock velocity} \propto r^{-jK/2}$$

The exponents $jK/2$ for various values of γ are listed in Table 1 for comparison with Butler's values for $(1-\alpha)/\alpha$. Chisnell explained the close agreement between corresponding values by obtaining a higher-order solution

which considered the modification of the shock motion by re-reflected disturbances. He found that although the disturbances are not small, they tend to cancel each other such that only slight modification results.

Whitham (Ref. 16) obtained the Chisnell relation between shock Mach number and channel area using a significantly different approach. The one-dimensional, unsteady equations of motion are written in characteristic form, and the differential relation which holds along characteristics intersecting the shock wave is applied to the flow quantities immediately behind the shock. Substitution of the Rankine-Hugoniot shock relations (expressed as functions of shock Mach number) results in a first-order equation for Mach number as a function of channel area which can be integrated directly to give a relation identical to Chisnell's. The validity of the method depends upon the smallness of the quantity $\frac{\partial p}{\partial t} + \rho a \frac{\partial u}{\partial t}$ at the shock (p is the fluid pressure, ρ the density, a the sound speed, and u the fluid velocity). Whitham shows that this quantity is zero for one of Chisnell's interactions, and since interference between successive interactions is neglected the results for the two approaches must be identical.

Whitham's method is more general in that it can be applied to shock wave propagation into various kinds of

nonuniform regions. An example of this will be given in Part 4.4b.

1.2c Shock Diffraction Due to an Initial Geometry Change

The Chester-Chisnell-Whitham formulation (hereafter referred to as the CCW theory) assumes that the interaction between the shock wave and the converging channel can be described by the one-dimensional equations of motion. As discussed in Part 1.3, experimental investigations have typically involved contractions of various shapes mounted on conventional shock tubes, and significant two-dimensional effects initiated at the transition from constant-area tube to converging geometry have been observed. These effects are due to Mach reflection of the plane incident shock on the channel walls, a phenomenon known to occur* where shock waves encounter even a slight inclination of channel boundary. In Mach reflection a discontinuity in shock strength and propagation direction occurs at a three shock intersection point (sketched in figure 30) which moves away from the channel wall as the main shock progresses. The two-dimensional nature of the shock diffraction results in local perturbations in the flow behind the shock, and the question arises as to the applicability of a one-dimensional

*A number of investigations of regular and Mach reflection of shock waves at inclined surfaces were made following World War II. A good example is Reference 5.

theory. Although previous investigators noted the occurrence of shock diffraction, they failed to address this question when comparing their results with the CCW theory.

1.3 Previous Experiments

The first experimental investigation of shock strengthening in converging channels was made by Bird (Ref. 17). Using argon at an initial pressure of 24 torr, shocks of Mach number 2.3 - 2.6 were passed through two-dimensional converging channels with various wall shapes. A schlieren system and drum camera were used to measure the shock speed along the channel centerline. Bird found that smooth, gradual contractions produced the largest shock velocity increases, which were within 20% of the predictions of the CCW theory. He also observed an apparent discontinuity in shock speed on some of his streak photographs, which he concluded was the intersection point of Mach reflections from the nozzle walls.

Similar drum camera techniques were used by Belokon' et al. (Ref. 18) and McEwan (Ref. 19). Using high-energy electric discharges Belokon' propagated extremely strong shocks (up to M = 67) in air into a two-dimensional wedge contraction. By examining the light emitted from the wedge vertex a rough estimate of temperature was made, and the device was suggested as a source of high-intensity

radiation. McEwan made streak photographs and sequential photographs of relatively weak shocks in air propagating into a two-dimensional parabolic contraction. Measurements of shock velocity using the streak records were claimed to show increases greater than predicted by the CCW theory, and McEwan suggested an optimum geometry might be found. Both Belokin and McEwan noted Mach reflection effects.

A nonoptical method of measuring shock strengthening was used by Russel (Ref. 20) and Dvir et al. (Ref. 21). In these investigations shock velocities were measured in a constant-area channel downstream of a conical convergence, and estimates of the shock velocity at the convergence exit were obtained by extrapolation. Russel's extrapolated values were below the CCW predictions, and the differences increased with increasing shock Mach number and decreasing pressure. Better agreement was obtained by using real-gas equilibrium conditions instead of ideal gas shock relations when applying Whitham's method. Dvir also found shock velocities that were less than predicted values.

The only nonoptical measurement of the shock trajectory inside a contraction was a preliminary investigation by Storm (Ref. 22) which led to the present work. A 17.5° half-angle conical convergence was mounted on the end of a three-inch diameter shock tube, and measurements were made of the shock transit time from a thin film gauge on

the straight shock tube to a piezoelectric pressure transducer located within the cone. By varying the transducer position along the cone axis between successive firings of the shock tube, a distance versus time trajectory for the shock motion within the cone was obtained. A definite shock acceleration was observed, but experimental scatter due to insufficient repeatability of the shock tube prevented accurate shock velocity measurements. The data did indicate the arrival on the cone centerline of at least one stemshock corresponding to Mach reflection on the convergence walls.

1.4 Goals of the Present Investigation

The present work is an experimental investigation into the behavior of strong shock waves in a convergent channel. The investigation is directed towards determining if such a geometrical device can be used to produce samples of high-enthalpy gases. In order to improve upon previous efforts, the first objective is the development of a new technique for accurately measuring shock wave velocity along the convergence centerline. Such measurements can be compared to the similarity/CCW predictions, and the extent to which the expected shock diffraction at the convergence entrance influences the shock behavior can be determined. By varying the strength of the initial shock and the initial gas pressure, the altering of the shock behavior by real gas

effects can be observed. Estimates of thermodynamic conditions immediately behind the incident shock can be obtained from calculated equilibrium conditions behind plane shocks of comparable strength, and fitting the similarity solution to the measured shock trajectories results in a qualitative description of how these conditions change in time. Since the convergence used is terminating, measurement of reflected shock trajectories can provide further insight into the state of the shocked gas. Any evidence of a rapid expansion in the hot gas behind the reflected shock would suggest the possibility of creating sustained nonequilibrium conditions.

II. EXPERIMENTAL APPARATUS AND PROCEDURE

2.1 The GALCIT Six-inch Shock Tube

The experiments were performed in the GALCIT* six-inch shock tube (Ref. 23), a facility designed for the production of strong shock waves under very reproducible conditions (a feature essential for the measurement technique used). The basic shock tube system consists of a 6' long, 6.5" diameter driver section, a diaphragm-transition section, and a 36' long, 6" diameter test gas section (figure 1). The entire tube is type 321 stainless steel with a 0.5" nominal wall thickness, and the inside surface is honed to a mirror finish. The reproducibility of the shock waves is achieved through a carefully designed diaphragm opening mechanism. A hydraulic system clamps the diaphragm in the diaphragm-transition section, and a set of crossed knife blades mounted across the transition section uniformly cuts the diaphragm as it bulges under pressure. The various diaphragm bursting pressures are repeatable to within 4 psia or less, resulting in shock waves with Mach numbers reproducible to within 1%.

The vacuum system consists of two mechanical pumps and a liquid nitrogen cold-trapped oil diffusion pump.

---

*Graduate Aeronautical Laboratories, California Institute of Technology

The test section can be evacuated to a pressure of 5×10^{-5} torr in one-half hour, then with pumps off the leak/outgassing rate is less than 1×10^{-3} torr per hour. A thermocouple gauge and a cold-cathode ionization gauge are used to monitor the vacuum level. Initial test gas pressure is set using a calibrated control volume (1/30 of the test section volume) connected to a 0-50 torr, bellows-type Wallace and Tiernan gauge. Incident shock velocities are measured using two platinum thin film heat transfer gauges mounted flush with the shock tube wall.

In the present investigation room temperature helium or hydrogen is used as the driver gas to produce Mach number 6.0 to 10.2 shock waves in argon. The initial test gas pressure was typically 1.5 torr, although some measurements were made at lower pressures.

2.2 The 10° Half-angle Conical Convergence

The circular cross-section of the GALCIT six-inch shock tube, together with machining considerations, dictated that a conical geometry be used for the area contraction. The experiments of Bird (Ref. 17), as well as a preliminary analysis of possible shock diffraction effects, led to the conclusion that the convergence angle should be as small as possible. The choice of 10° as the cone half-angle is a compromise between small angle and machining costs.

In the final design the cone consists of two sections

(figure 2). The first section, which comprises 60% of the convergence length, was made by electroplating nickel to a 3/8" thickness onto an aluminum mandrel (a procedure suggested by Professor Donald E. Coles). The principal advantage of this unique process is that the inside surface of the nickel section has the mirror finish of the mandrel, which was relatively easy to machine. The initial radius change on the mandrel (and thus on the nickel section) was smoothed over a $\pm$0.5" axial distance in the hope of reducing shock diffraction effects. The initial diameter of the nickel section matches the final diameter of the shock tube to within 0.001". The second cone section was made from 2024 aluminum bar stock using conventional machining methods. The minimum diameter of the second section is 1/8", giving an overall area reduction of 2300:1. A 1/8"-diameter hole remains at the vertex to allow insertion of instrumentation. The initial diameter of the second section matches the final diameter of the first section to within 0.001". The two sections are joined to each other and to the shock tube by means of collars and alignment rims. A vacuum seal is obtained at all joints by using neoprene O-rings.

2.3 Multi-crystal Axial Piezoelectric Probes

The basic deficiency of previous investigations is the lack of accurate shock velocity (and thus shock

strength) measurements within the area contraction. The only method that had been used was to measure the slopes of shock trajectories on distance versus time streak photographs obtained with a schlieren system and drum camera. This graphical differentiation procedure is subject to large errors, and is insensitive to small, localized variations in shock velocity. A better method of measuring shock velocity was obviously required in the present investigation in order to achieve the objective of a precise determination of shock behavior.

2.3a Probe Design and Construction

The device designed to produce accurate shock velocity measurements in the 10^{o} conical convergence is shown in figure 3. Suitably named a "multi-crystal axial piezoelectric probe", the instrument consists of two or more PZT-5* cylindrical tubes 0.043" in length contained within a 0.124" diameter axially-symmetric support structure. Conducting epoxy is used to fasten the inside surface of each crystal to separate 0.094" o.d. stainless steel support tubes 0.30" in length. Electrical leads are soldered onto the inside surfaces of the support tubes. A "basic two-crystal unit" is formed when a 0.094" i.d. fiber-filled phenolic tube having a precisely measured

*A lead zirconate/lead titanate piezoelectric ceramic manufactured by the Clevite Corporation.

length (0.367" typically) is used to join two crystal support tubes (figure 3). The probe used in most measurements has two such units, with their crystal-pair midpoints located 1.997" apart. Fastened on the front of the probe is a sharp (7^{o} total vertex angle) conical aluminum tip with a rounded shoulder. The probe shaft is a 0.120" o.d. stainless steel tube 11" in length. At the rear of this shaft are a 0.60" diameter aluminum collar used in locating crystal positions within the cone (described in Part 2.3b), and a 7-pin miniature connector to which the internal electrical leads from each crystal are soldered. The remainder of the support structure consists of a series of 0.124" o.d. stainless steel and phenolic tube segments connected by means of 0.094" o.d. stainless steel support tubes. A standard epoxy is used to fasten all components of the support structure, and to fill the interior of the probe shaft at the rear end to ensure a vacuum seal. The electrical path for the piezoelectric crystals is completed by using either silver print or conducting epoxy to paint conducting paths from the external crystal surfaces to the stainless steel probe shaft (which serves as a ground).

The probe is inserted into the cone at the vertex and positioned along the axis of symmetry. In order to

isolate the probe from stress waves in the cone walls* the shaft is entirely supported by three neoprene O-rings contained within an aluminum "probe holder" (figure 2). At maximum extension the tip of the probe is measured to be within 1/16" of the cone centerline, corresponding to a maximum angular deflection of less than $1/4^{o}$. For measurement of incident shock velocities near the cone entrance the second section of the cone is removed, and the probe inserted through an end wall fastened to the main cone section. The probe holder attaches to this end wall by means of an adapter.

2.3b Shock Velocity Measurements

The piezoelectric crystals are polarized between the inside and outside diameters. Thus, the radial compression produced by the shock pressure jump generates a sequence of signals as the shock passes the crystal positions along the probe. Shock velocities are determined by measuring the time interval between signals produced by the adjacent crystals in a "basic two-crystal unit". Since the velocity determined in this manner is an average over the distance between crystal positions, it is advantageous to have

*When the diaphragm bursts, stress waves generated in the shock tube walls propagate down the tube at a velocity considerably higher than typical initial shock velocities.

the crystals as close together as possible. The separation distance of 1cm* used in all crystal pairs is a compromise between a small averaging distance and sufficiently long time intervals to ensure adequate resolution. These intervals were typically in the range 1.6 - 5.5 microseconds, and the time resolution (discussed in Part 2.4) sufficient to obtain velocities accurate to 3% or better.

Typical probe responses for several different shock Mach numbers are shown in figure 4. The signals are unamplified, and no impedance-matching circuitry is used. Initial rise times are typically 0.4 microseconds and the initial ringing has a frequency of approximately 1.5 MHz.** The standard convention used in reading the crystal responses is to measure the time interval between the first positive peak on each signal (a detailed analysis of the probe response can be found in Appendix A.3). An exception to this is necessary at very high shock Mach numbers, when the fundamental mode of crystal response changes (shown in the third picture in figure 4). The modified convention is then to measure the time interval between the first small negative peak on each signal, and this necessitates a small time interval correction (discussed in Part 2.4).

---

*The distance corresponds to 0.023 of the cone length.

**The weak precursor oscillation shown on the bottom traces is a signal induced by the response of the adjacent crystal (upper traces).

When construction of the first probe was completed, it was tested in the straight shock tube where reference shock velocities could be measured with thin film gauges (the cone was removed and the probe mounted on a plane end wall). The first measurements gave velocities that were 7 - 11% lower than the reference values, indicating that a significant interaction between the shock wave and the probe was occurring. This interaction effect was believed to be primarily a result of the diffraction of the plane shock by the conical tip of the probe*. To alleviate the problem, the original probe tip (23° total vertex angle, 0.65" long) was replaced by the sharper, longer tip shown in figure 3 (7° total vertex angle, 2.83" long). This geometry change reduced the differences between the reference velocities and the probe-measured velocities to 1 - 4%, as shown in figure 5. In this figure the symbols V_{s_1} and V_{s_2} refer to velocity measurements made with the first and second crystal pairs, respectively.

The probe enables the measurement of shock wave velocity at two locations along the cone centerline during each firing of the shock tube. To obtain a complete shock velocity versus distance profile, it is necessary to make a large number of runs under identical initial conditions

*Mach reflection occurs, and a weak reflected shock remains attached to the probe tip.

while varying the probe position within the cone*. When adjusting the probe position the individual crystal locations relative to the cone must be found. A vernier caliper with 0.001" divisions is used to set the distance between the front face of the aluminum collar on the probe shaft and the rear face of the probe holder (figure 2). This effectively determines the crystal positions relative to the probe holder, since the distances from the aluminum collar to the various crystals were accurately measured during construction. Knowledge of the cone dimensions then allows the calculation of the crystal positions relative to either the cone entrance or the virtual vertex. Since the initial radius break at the entrance was smoothed during construction, it is necessary to define an "effective" cone entrance as the virtual location of the wall slope discontinuity. The distance from the "effective" entrance to the probe holder is found using the cone vertex angle and the dimensions of the second cone section. In this manner the crystal positions within the cone can be determined to within 0.002" relative to previous settings, and to within 0.005" relative to the probe holder. The distance from the probe holder to the "effective" cone entrance can be calculated to within 0.015".

---

*The extreme repeatability of conditions in the GALCIT 6" shock tube allows this approach to be used.

2.4 Data Reduction

To obtain a velocity value from an oscillogram displaying the responses of two adjacent crystals (figure 4), it is necessary to accurately determine the time interval between a consistent point on each signal, then divide this time by the corresponding distance traveled by the shock. As mentioned in Part 2.3b, the standard convention used in reducing most pictures is to measure the time between the first positive peak on each trace. Since this peak is believed to correspond to the instant when the shock arrives at the rear face of the cylindrical crystal (discussed in Appendix A.3), the appropriate distance used in computing the velocity is the length of the phenolic spacing tube plus the length of the second crystal. This distance is measured to within $\pm$0.001" for each crystal pair during construction.

To account for inaccurate oscilloscope sweep rates and horizontal drift of the beams, the time intervals are measured in a roundabout way. Timing marks placed simultaneously on both beams at the start of the sweep are used as an absolute time reference. The location of these timing marks and the initial positive peaks are scribed on the oscillogram, then the distance from the timing mark to the first positive peak on each trace is measured under magnification using a scale with 0.02" divisions. These distances

are converted to oscilloscope grid lengths by measuring the grid divisions on the oscillogram using the same scale. The grid scale numbers are then converted to times by using accurate sweep rate calibrations for each beam (made periodically during running by means of a Tektronix model 180A Time Mark Generator). The time interval is finally determined by subtracting the time from the timing mark to the initial positive peak on the first trace from the corresponding time on the second trace. The estimated accuracy for this reduction procedure is ± 0.05 microseconds for a typical 4 microsecond time interval. The marking and reading of the pictures must be done by hand, but the remainder of the manipulation is done by computer. The times from each crystal signal, together with delay times and vernier caliper readings, are also used to produce distance versus time shock trajectory data.

Two modifications to the data reduction procedure are required under certain conditions. The first involves a change in the basic crystal response mode when the shock Mach number is very high (shown in the third picture in figure 4). As discussed in Appendix A.3, it is believed that when the shock velocity is above a certain limit the crystal response changes from a longitudinal ringing mode to a radial ringing mode. The limiting velocity is not the same for all crystals, and at some shock speeds mixed-mode

oscillograms result. One consistent feature of crystal responses at higher shock velocities (just prior to and after the mode switch) is a small initial negative peak. The time difference between this negative peak and the first positive peak of the longitudinal mode can be measured for a small range of shock velocities, and is found to be nearly constant for each crystal. Thus, when the longitudinal mode is no longer visible in one or both traces on an oscillogram, the modified convention is to measure times to the initial negative peak and then add the small time differences previously determined.

The second modification required is a result of coating the entire surface of the probe with a thin layer of conducting epoxy when measuring very high shock velocities. The coating is necessary to protect the probe from the high temperatures produced by very strong shocks, but has the effect of attenuating the shock velocity along the probe surface (probably due to the local effect of increased surface roughness). By comparing identical measurements made with and without the probe completely coated, it was found that a $1.3 \pm 0.1\%$ attenuation occurred at the first crystal-pair position, and a $3.8 \pm 0.2\%$ attenuation occurred at the second crystal-pair position. A weak Mach number dependence was also indicated. To compensate for this attenuation when reducing data obtained with the probe coated, correction factors of 1.3% and 3.8% were added.

These corrections could be 1% low at the highest measured velocities due to the Mach number dependence.

III. RESULTS

In the first phase of the experiment the incident shock wave behavior was investigated by obtaining complete profiles of the centerline shock velocity along the length of the convergence. For the first profile a relatively low initial shock Mach number was used in order to minimize deviations from ideal gas behavior (present theoretical approaches assume a perfect gas). A second profile was then obtained using a much higher initial shock Mach number in order to observe the effects of relaxation and radiation processes. Finally, the effects of varying the initial shock Mach number and initial test gas pressure were studied at particular locations on the shock velocity profiles.

The piezoelectric probe was found to be sufficiently sensitive to respond to the weaker pressure jump associated with the reflected shock wave. Consequently, in the second phase of the investigation a complete profile of the centerline reflected shock velocity was obtained for each of the two primary conditions used in the first phase. The behavior of the reflected shock as it emerged from the cone entrance was observed using a piezoelectric probe with a much longer support shaft.

Estimates of actual gas conditions immediately behind the incident shock were obtained from calculations of the

equilibrium conditions behind plane shocks of comparable strength. To determine qualitatively how the gas properties vary in time after the incident shock has passed, the similarity solution (discussed in Part 1.2a) was fitted to the incident shock profiles. Fluid velocity, pressure, temperature, and density were computed numerically along particle paths for the flow between the incident and reflected shock waves.

3.1 Velocity of the Incident Shock Wave

3.1a Mach Six Initial Shock

For the first incident shock velocity profile a low initial Mach number and a relatively high initial test gas pressure were needed to minimize deviations from perfect gas behavior. It was necessary to compromise the low Mach number requirement, however, due to the minimum pressure jump requirements for adequate probe response (a minimum pressure rise of 50 torr was found to be necessary for good signals). The conditions chosen were an initial Mach number of 6.0 in argon at an initial pressure of 1.5 torr. At this pressure real gas effects are negligible for shock Mach numbers below nine.

The results of the measurements are shown in figure 6. V_s is the local shock velocity measured along the cone axis with the probe, V_o is the initial shock velocity, x is the distance from the cone entrance, and L is the total convergence length (from the entrance to the virtual

vertex). All data points are shown in figure 6 to illustrate the small experimental scatter. The most striking characteristic immediately apparent is that a gradual, monotonic increase in shock velocity does not occur, but instead there are a number of small intervals in which the shock experiences very rapid acceleration. The region between two of these sudden jumps is characterized by an initial deceleration interval followed by a gradual acceleration. The measured velocity for the first 30% of the convergence is the same as the initial shock velocity. Near the cone vertex the shock velocity has increased by a factor of three.

The data displayed in figure 6 indicate that Mach reflection of the initially plane shock occurs on the convergence walls, and the subsequent diffraction processes dominate the shock behavior throughout the convergence length. The first velocity jump shown in figure 6 corresponds to the arrival of the three-shock intersection point at the cone axis (sketched in figure 7). Beyond this point Mach reflection of the stemshock on the cone axis occurs (a previously unobserved effect), and a "center shock" (actually the new stemshock of the Mach reflection on the axis) progressively grows until it fills the cone cross-sectional area. At this time the entire diffraction process repeats, with Mach reflection on the cone walls followed by Mach

reflection of the stemshock on the cone axis. The cycle apparently continues until the cone vertex is reached.

The positions along the cone axis where stemshock intersections occur (hereafter referred to as intersection points) and the magnitudes of the corresponding velocity jumps can be determined more accurately by examining the individual piezoelectric crystal responses. As a particular crystal is moved past the intersection point on successive runs a marked increase in signal amplitude occurs. The intersection point position can thus be pinpointed (typically to within $\pm$.04") and runs made with a crystal-pair located on either side to determine the velocity jump. In figure 8 the intersection point positions are indicated with a dashed line. For this figure overlapping measurements have been averaged and data corresponding to intersection points occurring within a crystal-pair location have been eliminated.

The measured velocity just before each jump and the velocity increase across each jump are plotted versus intersection point position using logarithmic scales in figure 9. V_o is the initial shock velocity, V_s^- is the velocity immediately before the jump, and V_s^+ the velocity immediately after. Theoretical values from an approximate solution of the shock diffraction process (due to Mr. Erik Storm) are included in the figure, and will be

discussed in Part 4.2. The measured jumps in shock velocity appear to be nearly constant, while the velocity values immediately before an intersection point apparently have a simple power law dependence on intersection point position. The nearly equal logarithmic spacing of the intersection points indicates that the position of a given point (relative to the cone vertex and normalized by the cone length) is proportional to the position of the previous point.

3.1b Mach Ten Initial Shock

For measurement of a second shock velocity profile the initial conditions were altered so that "real gas effects" on the shock diffraction process could be observed. The initial test gas pressure was again 1.5 torr (measurements to study the effect of initial pressure variations will be described in Part 3.1c), but the initial shock Mach number was increased to 10.2. As discussed in Part 3.3a, for this initial Mach number significant electronic excitation and ionization should occur in the shocked argon beyond the first intersection point.

All data points obtained in this measurement are shown in figure 10. The general features of the profile are the same as the Mach six case up to the third intersection point, after which considerable differences are apparent. Figure 11 shows the same data with the intersection points located, overlapping measurements averaged, and data

corresponding to intersection points occurring within a crystal-pair position eliminated. The dashed line in this figure indicates the results of the Mach six measurements for comparison. Beyond the third intersection point the high Mach number data show a rapid decline in the shock velocity. The velocity jump at the fourth intersection point is very weak, and a fifth intersection point is not observed (in both cases the measurements terminate at $x/L = 0.95$). The locations of the first two intersection points are the same, while the third and fourth points are displaced slightly.

The jump in shock velocity at each intersection point and the velocity immediately before each jump are plotted versus intersection point position on logarithmic scales in figure 12. The velocity jumps are not constant in this case, but instead decrease progressively. The measured velocities just prior to intersection points deviate slightly from the simple power law dependence on intersection point position found with the Mach six initial shock data.

3.1c Effects of Varying Initial Mach Number and Test Gas Pressure

The shock diffraction theory (Appendix B) predicts that at any particular location in the cone the measured shock velocity should scale with the initial velocity. Because the theory assumes ideal gas behavior, a breakdown

in the scaling is expected at higher Mach numbers when real gas effects become important. The shock velocity profiles in figure 11 show that increasing the initial Mach number from 6.0 to 10.2 results in a significant scaling breakdown only after the third intersection point. Since the local Mach number jumps from 19.1 to 23.2 at this intersection point in the Mach ten case, the profiles do not accurately indicate the local Mach number where real gas effects begin to alter the shock diffraction pattern. In order to examine the dependence on local Mach number more precisely a series of measurements were made holding the probe at fixed locations while varying the initial shock Mach number between 6.0 and 10.2. The initial pressure was again 1.5 torr. The results are shown in figure 13, where measured velocity normalized by initial velocity is plotted as a function of initial shock Mach number for three locations along the cone axis. As might be expected from figure 11, no significant variations are observed except at a position between the third and fourth intersection points. At this location the scaling begins to fail at a local Mach number between 18.7 and 19.8.

Because real gas effects are enhanced by reducing the initial gas pressure (Refs. 24, 25), the measurements shown in figure 13 were repeated for the last two probe positions using an initial pressure of 0.5 torr. The results are shown in figure 14. At a position between the

second and third intersection points the measured velocities are nearly the same as in the higher pressure case, though a slight rise with increasing initial Mach number is indicated. At a position between the third and fourth intersection points the measured velocities are substantially lower and show no variation with initial Mach number. The highest local Mach number measured at this location is 21.1.

3.2 Velocity of the Reflected Shock Wave

The incident shock velocity profiles show that multiple Mach reflection processes are initiated at the cone entrance and continue until the cone vertex is reached. An interesting question arises as to whether the shock wave retains a two-dimensional character upon reflection, or instead appears like a spherical shock emanating from a point source. Whatever the nature of the shock immediately after reflection, its subsequent behavior is determined by the divergent geometry and the complex flow generated by the incident shock. Although the nature of this flow can only be inferred from an investigation of the reflected shock behavior, such an investigation was undertaken in the hope of contributing to a qualitative understanding of the way gas properties change in time after the incident shock has passed. Measurement of reflected shock velocity profiles began after the piezoelectric

probe was found to be capable of responding to the weaker pressure jumps associated with the reflected shock. Since complete incident shock profiles were determined at an initial pressure of 1.5 torr in argon using initial shock Mach numbers of 6.0 and 10.2, these conditions were chosen for the reflected shock measurements.

3.2a Mach Six Initial Shock

The results of the velocity measurements made using a Mach six initial shock are shown in figure 15. The data points are averaged from two or three runs, and the error bars indicate the experimental scatter. The measurements for $x/L > 0.3$ were made with the four crystal probe described in Part 2.3, while the measurements for $x/L < 0.3$ were made using a probe constructed with a 22" shaft containing only one pair of crystals. V_{RS} is the measured reflected shock velocity, and V_E is the velocity of a shock reflecting from a plane end wall under the same initial conditions. The numerical value for V_E results from calculations of equilibrium conditions in argon by Arave and Huseby (Ref. 25), in which electronic excitation and single ionization are taken into account.* For the initial conditions used in this measurement, V_E is 6.6% less than the corresponding ideal gas reflected shock velocity.

---

*The use of real gas values for V_E was suggested by Dr. J. E. Broadwell.

The first feature of the data in figure 15 is the absence of values for $x/L > 0.84$. Measurements were attempted in this region, but no detectable signals corresponding to shock propagation were observed. The measurements shown for $x/L > 0.80$ are characterized by very weak probe signals. The second feature of the data is the velocity variation which occurs in the region $0.55 < x/L < 0.84$, and to a lesser degree near the cone entrance. Between these two regions the measured velocity shows a surprisingly slow deceleration, decreasing by only 11% over a distance of half the convergence length. Beyond the cone entrance the shock deceleration increases, and the measured velocity appears to be approaching the value for shock reflection from a plane end wall.

The reflected shock was also observed using the two platinum thin film gauges located 13.3 cm and 23.3 cm from the cone entrance. The last datum point on figure 15 was obtained with these gauges, the position shown corresponding to the midpoint 18.3 cm from the cone entrance. This value is necessarily an average over the 10 cm spacing between the gauges. Typical thin film responses produced by the reflected shock are shown in figure 16a. The unsteady oscillations in the signals following the reflected shock are characteristic of these gauges when the gas is partially ionized (Refs. 26, 27), and thus indicate that upon emergence from the cone the reflected shock is strong

enough to produce at least a small degree of ionization. The small "dips" indicated on the first oscillogram in figure 16a are a consequence of radiation emitted from the cone vertex region after the reflection of the incident shock. These will be discussed further in Part 4.4d.

A final feature of the $M_o = 6.0$ reflected shock measurements is shown in figure 17, which is a distance versus time plot of the incident and reflected shock waves. In the region $0.74 < x/L < 0.92$ a second reflected shock is clearly visible in piezoelectric probe responses recorded using a slower oscilloscope sweep rate. As the parallel trajectories in the figure indicate, the measured velocity of this shock is nearly the same as the primary reflected shock velocity. The probe signal corresponding to the second shock is weak for $x/L < 0.80$, and for $x/L < 0.74$ the signal can not be seen. The dashed-line curves in figure 17 are approximate particle paths calculated from the Guderley similarity solution (discussed in Part 3.3b).

3.2b Mach Ten Initial Shock

The results of reflected shock velocity measurements made using an initial shock Mach number of 10.2 are shown in figure 18. The data points are averages over two or three runs, and error bars indicate typical scatter. The notation is the same as in figure 15, but V_E is now the

calculated (real gas) velocity of a shock reflecting from a plane end wall under the present initial conditions. For this case V_E is 45.9% less than the corresponding ideal gas reflected shock velocity. The dashed line in figure 18 indicates the results of the Mach six initial shock measurements for comparison

The general features of the Mach ten initial shock measurements are similar to those found in the lower Mach number case. Near the cone vertex rapid variations in velocity are observed, but these variations are smaller and occur closer to the vertex. Unlike the Mach six case, the reflected shock is easily detectable up to $x/L = 0.95$ (the probe measurement limit). The velocity is again nearly constant over a large fraction of the convergence length, and beyond the cone entrance a more gradual deceleration towards the velocity value for shock reflection from a plane end wall is indicated.

Considerable difficulty was encountered in observing the reflected shock with the thin film gauges due to spurious signals occurring prior to the reflected shock arrival. These large-amplitude, unrepeatable signals indicate charged particles are present, produced either by photoionization or by photoemission from the film. A consistent signal caused by radiation emitted from the hot gas at the cone vertex (upon reflection of the incident shock) preceeded the irregular signals, as shown in figure 16b.

A distance versus time plot of the incident and reflected shock trajectories is shown in figure 19. In contrast to the Mach six case, a second reflected shock could not be detected. The dashed-line curves in the figure are approximate particle paths calculated from the similarity solution (Part 3.3b).

3.3 Flow Conditions Behind the Incident Shock Wave

The measurement of incident and reflected shock velocity profiles determines the dynamic behavior of strong shock waves in the conical convergence. Although these measurements are the primary objective of the experiment, the underlying motive is to ascertain if such a convergence can be used to produce high-enthalpy gas samples. For this, corresponding estimates of thermodynamic conditions in the shocked gas are necessary. Efforts to make these estimates are restricted by the complex nature of the flow generated by the incident shock. Nevertheless, a qualitative description of the flow between the incident and reflected shock waves can be obtained from perfect gas and equilibrium normal shock conditions, and from the Guderley similarity solution. Similar means for obtaining estimates of conditions behind the reflected shock are not available.* A brief discussion of possible conditions in this region is given in Part 4.4d.

---

*The similarity solution for the flow behind the reflected shock is not applicable (discussed in Part 4.4a).

3.3a Normal Shock Equilibrium Conditions

When the incident shock is at any position along the cone centerline (except near an intersection point), the thermodynamic conditions closely behind the shock should be approximated by the conditions behind a plane shock with the same Mach number. For an initial pressure of 1.5 torr, ionization is negligible in argon when local Mach numbers are less than nine, and the plane shock conditions are given by the ideal gas Rankine-Hugoniot equations. At higher Mach numbers the "frozen" conditions immediately behind the shock are still given by the ideal gas equations, but a relaxation region follows in which equilibrium ionization is established. Equilibrium conditions beyond the relaxation region can be calculated numerically. The accuracy in using these one-dimensional calculations to estimate experimental conditions depends upon whether the corresponding length of the relaxation region is small compared to local cone and shock diffraction dimensions.

By combining the methods of statistical thermodynamics with the gasdynamic conservation laws, Arave and Huseby (Ref. 25) calculated equilibrium properties of argon across incident and reflected normal shock waves. Only single ionization and excitation to the first few electronic energy levels were taken into account, but these approximations are reasonable for the range of Mach numbers measured in the cone. Since the calculations are made

for initial pressures of 0.1, 1.0, and 10 torr, interpolation is necessary to find conditions corresponding to an initial pressure of 1.5 torr. The resulting values for the equilibrium temperature ratio T_2/T_1* , pressure ratio p_2/p_1 , and degree of ionization α are plotted as functions of shock Mach number in figure 20. Indicated in the figure are the range of local Mach numbers observed in the measurement of the two incident shock velocity profiles, and the particular Mach numbers found at certain positions along the cone centerline (approximate midpoints between stemshock intersection points). At a position between the third and fourth intersection points ($x/L = 0.86$) the predicted temperatures behind the incident shock for the initial Mach number six and ten cases are 11,000°K and 14,100°K respectively, the corresponding pressures are 0.487 and 1.325 atmospheres, and the degrees of ionization are 0.075 and 0.346.

The curves in figure 20 furnish estimates of conditions closely behind the incident shock provided the length of the relaxation region is small compared to local cone and shock diffraction dimensions. Theoretical and experimental studies of the relaxation region behind strong shocks in argon (Refs. 28, 29) show that the relaxation distance decreases with increasing Mach number and initial pressure.

---

*The subscripts "1" and "2" denote conditions ahead of and behind the advancing normal shock, respectively,

Table 2 lists relaxation distances and times (laboratory frame of reference) for the Mach numbers measured in the two incident shock velocity profiles at the four particular positions indicated in figure 20. The cone radius and the distance to the previous intersection point at each of these positions are also listed for comparison. In the Mach six case the relaxation distances are large compared to the experimental dimensions, indicating that the thermodynamic variables behind the incident shock do not attain the predicted equilibrium values before compressive changes resulting from the converging geometry occur. In the Mach ten case the relaxation distances are smaller than the experimental dimensions for positions beyond the second intersection point, and estimates from figure 20 should be more accurate.

3.3b Similarity Solution for Flow in Convergence

Because the normal shock calculations only provide estimates of conditions directly behind the incident shock, it remains to determine how these conditions vary in time after the shock has passed. The similarity solution described in Part 1.2a produces a complete description of the flow field behind a spherical shock imploding in an ideal gas. The assumptions of spherical symmetry and perfect gas behavior prevent a quantitative description of the flow produced in the experiment, but the solution still provides a qualitative picture of the expected compression

resulting from the conical geometry.

The solution is formulated using the independent variables r and t', where r is distance from the point of symmetry, and t' is time measured from the instant of collapse of the imploding shock. In the experiment the more practical variables are distance measured from the cone entrance, x, and time measured from the shock arrival at the cone entrance, t. The two sets of variables are related by

$$r = L - x , \quad t' = t - t_A$$

where t_A is the time required for the incident shock to propagate the length of the cone. The results of Butler's calculations (Ref. 12) are in the form u/U_o' and a/U_o' at a fixed r_o, plotted as functions of t'/t_o'. u is the fluid velocity, a is the local sound speed, U_o' is the shock velocity at the position r_o, and t_o' is the time at which the shock reaches r_o. The last three values are related by $t_o' = Br_o^{1/\alpha}$, where B is as yet undetermined. To use the solution it is necessary to pick an initial shock position (r_o , t_o') and either the shock velocity at this position or t_A. Some flexibility thus exists in fitting the solution to the experimentally-determined incident shock trajectory. The exponent in the power-law dependence of shock velocity on position (which is a fundamental result of the solution) is not affected by the fitting.

Figure 21 shows various fits of the similarity solution to the Mach six incident shock data. x_o/L and T_o are the normalized initial shock position and time chosen, U_o is the shock velocity at the cone entrance (either chosen or fixed once t_A is chosen), and T_A is simply t_A normalized. All times are normalized by L/V_o, where V_o is the measured shock velocity at the cone entrance. Matching the position and velocity at the cone entrance (curve 1) results in a predicted shock that is faster for most of the cone length, and thus arrives at the vertex sooner. Matching the position at the entrance and the final arrival time t_A (curve 2) results in a predicted shock initially slower than observed, but again progressively faster near the vertex. Matching the position at an intermediate point within the cone (midway between the first two stemshock intersection points) and the final arrival time results in a much slower predicted shock at the cone entrance, but a better fit near the vertex (curve 3). The last matching method is the most appropriate, since the similarity solution is valid only in some neighborhood of the point of symmetry.

Using the fitting conditions for the third curve in figure 21 and Butler's calculations for fluid velocity behind the incident shock, particle paths were computed by numerically integrating

$$\frac{dx}{dt} = u(x,t)$$

for $x(t)$. Examples of the resulting particle paths are shown in figures 17 and 19*. Each computation is terminated by the arrival of the reflected shock as predicted by the similarity solution, which characteristically occurs earlier than the observed reflected shock. Fluid temperatures along a particle path follow from Butler's computed values for sound speed. Pressures and densities are found by noting that the quantity p/ρ^{γ} is constant along a particle path (since entropy is constant along a particle path), where p is the pressure, ρ the density, and γ the specific heats ratio. For a given particle path the value of p/ρ^{γ} can be found from the shock jump conditions using the shock velocity at the initial particle path position. Knowing the sound speed $\left(\sqrt{\gamma p/\rho}\right)$ at each point along the path then allows solution for p and ρ .

The results of these calculations are shown in figures 22 - 25. In figure 22, fluid velocity along several particle paths is plotted as a function of time. u_{2_o} is the fluid velocity behind the Mach six initial shock, while $(x/L)_I$ and $(x/L)_R$ are the initial and final particle positions. Along each of the paths a fluid particle

*The similarity solution was fitted to the Mach ten incident shock data to obtain the particle paths shown in figure 19.

experiences a gradual acceleration followed by a rapid deceleration. This behavior is accentuated near the vertex. Fluid pressure along the same particle paths is plotted on semi-logarithmic scales in figure 23. The monotonic rise in pressure becomes quite steep near the vertex, with a fluid particle initially shocked at $x/L = 0.76$ experiencing a factor of 14 increase. Temperature also rises considerably along particle paths, as shown in figure 24. The fluid particle starting at $x/L = 0.76$ experiences a factor of 2.8 increase during the compression. The variation of fluid density along a particle path is very similar to temperature, with the same particle experiencing a factor of 4.5 increase. In figure 25, fluid velocity, pressure, and temperature are plotted versus cone position at the instant the shock reaches the cone vertex. Conditions near the cone entrance are not shown, since the similarity solution can only be applied to fluid particles originally located within the convergence.

The calculations shown in figures 22 - 25 provide a qualitative description of the compression which follows the $M_o = 6.0$ incident shock. Only scale changes result from similar calculations using a fit to the $M_o = 10.2$ incident shock, since the Guderley solution assumes ideal gas behavior. Because of increasing ionization in the experimental flow, the actual temperature rises during the

compression should be smaller than the predictions of the similarity solution, and the density increases should be somewhat larger. The actual pressure changes are probably comparable.

IV. DISCUSSION

4.1 Comparison of Incident Shock Behavior with One-Dimensional Theories

The Guderley similarity solution and the Chester-Chisnell-Whitham theory (in the strong shock limit) predict that shock velocity varies with distance from the cone vertex (r) according to the power law

$$\text{shock velocity} \propto r^{-n}$$

where the exponent depends only on the specific heats ratio, γ . Butler's calculation of the similarity solution gives $n = 0.45269$ for argon ($\gamma = 5/3$), while the CCW theory predicts $n = 0.45211$. The CCW formulation requires that the initial shock velocity at the cone entrance be specified, whereas an undetermined constant and a different time origin in the similarity solution allow some flexibility in choosing the initial conditions.

In figures 26 and 27 the similarity and CCW solutions are compared with curves representing the incident shock data and the shock diffraction solution (discussed in Part 4.2). Because shock velocity is plotted as a function of distance from the vertex on logarithmic scales, the similarity and CCW curves appear as straight lines. The "#3 fit" of the similarity solution refers to the matching conditions chosen for the third curve in figure 21, in which measured arrival times at the midpoint between the first

two intersection points and at the vertex are used to fit the solution to the incident shock trajectory. Such a fit is a better approximation near the vertex, where (in the absence of real gas effects) the validity of the similarity assumption improves. The same V_o is used to normalize both the CCW and similarity velocity values, and consequently the similarity solution is shifted downward (the "#3 fit" gives a lower initial velocity). The CCW curve in figure 26 shows the effect of correcting the local channel cross-sectional area for the area of the piezoelectric probe. The correction is negligible for $x/L < 0.90$, and at $x/L = 0.95$ only a 4% velocity increase results.

A fundamental difficulty in comparing the experimental results and the one-dimensional theories arises from the fact that the measured values are centerline velocities of a shock wave with distinct two-dimensional variations over its surface (which persist until the cone vertex is reached), whereas the theories assume a uniform shock producing one-dimensional flow. A question that comes to mind is whether the one-dimensional theories still approximate the shock strength averaged over its surface area. Knowledge of only the centerline shock velocity is insufficient to determine such an average, but a qualitative estimate can be made by noting that the stemshock formed in Mach reflection possesses higher local velocities than the original shock. At a position approximately midway between two successive

intersection points, the center shock formed by Mach reflection on the cone axis (figure 7) occupies the entire cross-sectional area. Since variations in Mach number over the center shock surface should be small compared to the changes which occur at a three-shock intersection, the measured velocity at this position should be close to an averaged value. Between such a midpoint and the next intersection point the growing stemshock contributes higher local velocities towards an average, and the centerline velocity in this region will be less than an averaged velocity. Between a midpoint and the previous intersection point the center shock is itself a stemshock formed by Mach reflection on the cone axis, and centerline velocities in this region will be greater than an averaged value. By such arguments it follows that an experimental curve of shock velocity averaged over the shock surface area would be "smoothed out" and appear more like the power-law curves in figures 26 and 27. The mean slope of the smoothed curve would be somewhat less than the theoretical slope, since the measured velocities at positions midway between intersection points fall progressively below the corresponding theoretical values.*

---

*A rough calculation for an averaged shock velocity up to the first intersection point, in which the stemshock is assumed straight with a uniform Mach number equal to that at the wall (given by the diffraction solution described in Appendix B), predicts a smoothly rising shock velocity which remains within 3% of the CCW theory.

4.2 Comparison of Incident Shock Behavior with an Axisymmetric Shock Diffraction Solution

The measurements of centerline shock velocity should be more properly compared with a theoretical model which takes into account the cyclic pattern of stemshock growth and reflection. Since significant difficiencies remain in theoretical descriptions of the simpler problem of Mach reflection on a plane wedge, an accurate analysis of the shock diffraction in the cone is not feasible. However, an approximate solution capable of predicting the basic diffraction characteristics observed in the experiment has been formulated by Mr. Erik Storm, using a theory on shock dynamics by Whitham (Refs. 30, 31). A preliminary description of this solution can be found in Reference 22, but a complete account remains to be published. A summary of Storm's solution can be found in Appendix B.

Comparisons between the incident shock measurements and the diffraction solution (for centerline shock velocity) are shown in figures 9, 12, 26 and 27. The shock diffraction is assumed to begin on a discontinuous change in wall slope at the cone entrance, whereas the actual slope change at the entrance was intentionally smoothed during construction. This may account for the predicted stemshock intersections occurring slightly sooner than observed. The theoretical velocity jumps at the intersection points are considerably larger than the measured values, but

display the constancy shown by the $M_o = 6.0$ results. The solution closely predicts the observed power-law dependence of V_s^- (the velocity immediately before a jump) on distance from the cone vertex. By assumption, the theoretical intersection points have nearly equal logarithmic spacing comparable to that found experimentally. The observed deceleration of the center shock following each stemshock intersection is qualitatively predicted, but the subsequent acceleration prior to the next intersection point is not. This contrast is a consequence of assuming that rays normal to the center shock remain straight (Appendix B). A basic difference between the solution and the experiment is the necessity of having a finite diameter probe present in carrying the theoretical calculation past the first stemshock intersection. In the experiment the diffraction process was found to be insensitive to the presence of the probe at an intersection point*. Since the theoretical model assumes perfect gas behavior, the increasing disparities between the calculation and the measurements for $M_o = 10.2$ are expected.

---

*Due to the large spacing between the crystal pairs in the probe, it was possible to measure the velocity at certain points (such as $x/L = 0.51$) with the first stemshock intersection occurring on the probe, and then repeat the measurement with the probe beyond the intersection point. The resulting velocity values were always within the scatter shown in figures 6 and 10.

4.3 Real Gas Effects on the Shock Diffraction Process

The approximate diffraction solution predicts that the incident shock velocity at any location in the cone should scale with initial velocity. This feature of the solution follows from the use of the CCW area - Mach number relation in the strong shock limit (Appendix B). As stated by Whitham in his development of the diffraction theory (Refs. 30, 31), the shock wave should pass through the same sequence of positions for all initial Mach numbers, the only difference being a proportionate change in the time scale. This conclusion is subject to the validity of the perfect gas assumption used in the analysis. Since real gas effects will alter the basic area - Mach number relation (discussed in Part 4.3a), a breakdown in the velocity scaling is expected for sufficiently strong shocks. It is therefore surprising that for $M_o = 10.2$ the diffraction pattern is unchanged except near the vertex $(x/L \geq 0.84)$ where local Mach numbers are very high $(M \geq 19)$, even though considerable ionization (>5%) should occur beyond the first intersection point $(x/L \geq 0.30)$. This result will be investigated in the following sections.

4.3a Relaxation Effects

The calculated equilibrium conditions shown in figure 20 deviate from corresponding ideal gas curves for Mach numbers above 9, commensurate with the onset of significant

ionization. Equilibrium temperatures progressively fall below the ideal gas values as Mach number increases, while equilibrium pressures and densities are progressively higher. Russel (Ref. 20) used calculated equilibrium conditions instead of ideal gas jump conditions in applying Whitham's method for obtaining the one-dimensional area - Mach number relation. The resulting Mach number increase predicted for a particular area reduction was considerably less than that given by the ideal gas formula. Since the area - Mach number relation is the essential fluid mechanics result used in the diffraction solution, it should be possible to use a "real gas" relation obtained in this manner to modify the diffraction analysis. The required computational effort was not undertaken, since the anticipated result would show a progressive departure from initial velocity scaling at any position as the initial Mach number is increased. Such behavior would be inconsistent with the experimental results shown in figures 13 and 14.

The persistent scaling of the measured shock velocities indicates that the wave propagation and diffraction are insensitive to the relaxation processes in the shocked gas. This uncoupling of shock velocity and thermodynamic equilibration intuitively seems to be a consequence of the unsteady nature of the wave motion. To examine this possibility, local relaxation times can be compared with time scales

associated with the changes in shock velocity. Relaxation times for steady, plane shock propagation* can be taken from the results of Petschek and Byron (Ref. 28), but some uncertainty exists in choosing appropriate time scales for the unsteadiness of the shock motion. If the shock displayed continuous acceleration as predicted by the one-dimensional theories (Parts 1.2a, 1.2b), a suitable time scale would be $t_s = V/(dV/dt)$, where V is the local shock velocity. Using the similarity results discussed in Part 1.2a, it follows that $t_s \propto R/V$, where R is the local cone radius. Choosing R/V as the time scale for shock velocity changes, comparisons with relaxation times can be made for the Mach numbers measured at various positions in the cone. If τ denotes the relaxation time (laboratory reference frame) behind a shock with constant velocity V, then the relaxation distance (laboratory reference) is $\ell = V\tau$. An equivalent comparison is therefore between relaxation distance and cone radius. As mentioned in Part 3.3a, the ratio of relaxation distance to cone radius is greater than one for the entire $M_o = 6.0$ incident shock velocity profile, and for positions prior to the second intersection point in the $M_o = 10.2$ profile. The comparison of these characteristic lengths (or times) proves to be more interesting for

*In laboratory frame of reference, with an assumed impurity level of 5×10^{-5}.

measurements made near the vertex where the scaling breakdown occurs. For an initial pressure of 1.5 torr, the ratio of relaxation distance to cone radius at $x/L = 0.86$ is less than one for local Mach numbers above ~18, and greater than one for lower Mach numbers (values listed in Table 3). As shown in figure 13, the velocity scaling begins to fail at this position when the local Mach number reaches ~19. For an initial pressure of 0.5 torr, this ratio at the same position is greater than one for all Mach numbers measured (up to M = 21). Figure 14 shows that the velocity scaling in this case persisted (although an initial pressure effect apparently decreased the scaling factor).

These comparisons suggest that perfect gas scaling continues as long as relaxation processes proceed slowly relative to changes in the shock velocity. The eventual breakdown in scaling apparently occurs when the relaxation becomes sufficiently rapid so that equilibrium conditions "catch up" to the shock and modify its motion. However, the fact that scaling persists in the $M_o = 10.2$ measurements beyond the second intersection point (where relaxation distances are less than local cone dimensions) indicates that this simple comparison of the chosen time scales is probably an over-simplification, and additional physical processes could be involved.

4.3b Radiation Effects

The high Mach numbers measured in the convergence indicate that the shocked gas should radiate strongly upon reaching equilibrium. The energy flux associated with this radiation is probably sufficient to cause considerable cooling of the equilibrium region.* Absorption of the radiation by the cold gas ahead of the shock can influence the shock motion by effectively changing the test gas initial conditions. Analytic studies of steady shock propagation with radiative heat transfer (for example, Ref. 33) show that temperature, pressure, density, and fluid velocity are all increased in front of the shock over a distance of the order of the absorption mean free path. For argon the radiation flux consists primarily of visible and near-ultraviolet continuum radiation (Ref. 32), and corresponding photon mean free paths are quite long (~1 meter for 1.5 torr initial pressure). It therefore seems unlikely that radiative preheating directly effects the incident shock motion, although a focusing of the radiation by the conical geometry could intensify preheating near the vertex.

The incident shock behavior can be influenced by radiation effects in an indirect manner. It was suggested in Part 4.3a that perfect gas scaling persists as long as

*Wong and Horn (Ref. 32) found experimentally that for a Mach 16 shock in argon at 3 torr, radiative cooling rapidly reduced the equilibrium degree of ionization from 16% to 10%.

relaxation proceeds slowly compared to changes in the shock velocity. Any mechanism which will increase relaxation rates near the cone vertex should enhance the scaling breakdown which occurs in this region. Such a mechanism can result from the production of free electrons ahead of the incident shock by photoionization and by photoemission from the cone walls. In the absence of precursor electrons, the first stage of the relaxation process involves the production of a small degree of ionization ($\sim$ 10% of the equilibrium value) by relatively inefficient atom-atom collisions (Ref. 29). After approximately four tenths of the total relaxation time, a second stage begins in which ionization proceeds by inelastic electron-atom collisions. The ionization rate in this regime depends upon the rate at which electrons acquire energy through elastic collisions with ions. The presence of precursor electrons at the shock front will therefore reduce the time required for the first relaxation stage, and if a significant number are fairly energetic ($\geq$ 1eV) the ionization rate in the second stage will be increased.

Figure 13 shows that at $x/L = 0.86$ the velocity scaling begins to fail when local Mach numbers reach ~19. In order to have an initial degree of ionization corresponding to 10% of the equilibrium value behind a Mach 19 normal shock (1.5 torr initial pressure), a precursor electron number density of approximately 10^{15} cm^{-3} is required at the shock front. Reasonable estimates of

precursor levels in the convergence due to photoionization are difficult to make, since experimental and theoretical nvestigations of photoionization in argon have been restricted to steady propagation of normal shocks at lower Mach numbers. For example, Lederman and Wilson (Ref. 34) measured electron number densities less than 10^{10} cm^{-3} at the front of a Mach 13.4 shock (1 torr initial pressure). Theoretical descriptions by Ferrari and Clarke (Ref. 35) and by Dobbins (Ref. 36) predict precursor levels several orders of magnitude below experimental values. On the basis of what information is available, it seems doubtful that photoionization alone could produce sufficient precursor electrons to significantly reduce relaxation times. The importance of wall reflectivity has been pointed out by Dobbins, however, and a focusing effect due to the conical geometry could therefore enhance photoionization in the vertex region.

An additional source of precursor electrons is photoemission from the cone walls. Although suggested by Hollyer in one of the earliest reports of precursors in shock tubes (Ref. 37), photoemission has not been carefully investigated. The importance of this process in the present experiment is indicated by the fact that photons resulting from electron-ion recombination to the ground state have energies that are large ($\geq$13.9eV) compared to the work function of the

aluminum cone (4.1eV). Although Wong and Horn (Ref. 32) felt this ultraviolet radiation could be neglected, the analysis of Dobbins shows it to be important at high Mach numbers. Because the absorption mean free path for this radiation is relatively short*, significant precursor levels resulting from photoemission should occur only near the vertex. In this region the combination of photoionization and photoemission is probably sufficient to reduce relaxation times, and thus contributes to the breakdown in velocity scaling.

4.4 Reflected Shock Behavior

4.4a Comparison with Similarity Solution

The reflected shock velocity measurements are compared with corresponding curves given by the Guderley similarity solution in figure 28. The theoretical curves are obtained by fitting the similarity solution to the incident shock data in a manner that matches shock velocities near the cone vertex (described in Part 3.3b). The measured values for the initial Mach number six and ten cases, as well as the similarity values, are normalized by their respective initial shock velocities and plotted versus distance from the vertex using logarithmic scales. The similarity curves appear as straight lines, since the solution predicts that

*At $x/L = 0.86$, the ratio of cone radius to photon (15.75eV) mean free path is ~2 for 1.5 torr initial pressure.

the shock velocity varies with distance from the vertex according to the power law

$$V_{RS} \propto r^{-n}$$

where $n = 0.4527$. The measured velocities obviously do not display a power law behavior, but rather remain nearly constant for much of the convergence length. This contrast is a consequence of fundamental differences between the experimental flow conditions and the conditions assumed in the similarity analysis for the reflected shock.

The primary difference leading to the observed behavior is illustrated in figures 17 and 19. The first particle path shown in each figure is the approximate trajectory of a fluid particle initially located at the cone entrance. This path represents a boundary separating fluid initially outside the convergence and fluid involved in the incident shock diffraction. For $x/L < 0.66$ (approximately) in the $M_o = 6.0$ case, and $x/L < 0.75$ in the $M_o = 10.2$ case*, the reflected shock propagates into fluid originally set into uniform motion by the plane, constant-strength initial shock wave outside the cone entrance. In the similarity analysis the fluid in these regions has supposedly undergone a gradual, continuous compression after initially experiencing a much weaker shock, resulting (apparently) in conditions ahead of the reflected shock that progressively

*Indicated by the dashed lines in figure 28.

deviate from the actual flow conditions. Figure 18 shows that these regions correspond to the intervals in which the measured velocities are nearly constant.

Additional differences are important in the region near the cone vertex. The similarity solution assumes that an infinitely thin shock reflects at the point of symmetry, and as a result the initial reflected shock velocity is singular. The significance of having a finite shock thickness is shown by the numerical calculations of Payne (Ref. 38), in which an artificial diffusion term is included in the equations of motion to simulate the effects of viscosity and heat conduction. For an imploding cylindrical shock initiated at a radial position $r = R$, the incident shock calculations agree with the theory until $r/R \sim 0.08$.* At the axis the singularity is replaced by finite flow conditions, and the initial reflected shock velocity is comparable to the velocity of the incident shock at $r = R$. The reflected shock displays very little deceleration until $r/R \sim 0.5$, after which its velocity falls rapidly. Although Payne's calculations assume cylindrical symmetry, these results are qualitatively similar to the observed reflected shock behavior in the vertex region.** In the experiment the reflection actually occurs at the vertex of

---

*The shock thickness in the calculations is typically $\sim 0.02R$.

**This point was suggested by Professor G. B. Whitham.

a locally annular contraction because of the presence of the piezoelectric probe.

4.4b Reflected Shock Propagating into Steady, Subsonic Flow

In part 4.4a it was pointed out that during the portion of the reflected shock trajectory in which the shock velocity is nearly constant, the shock propagates into fluid originally set into uniform motion outside the cone entrance. If a simplified model is assumed for the subsequent flow of this fluid, an analytical description of the reflected shock motion can be obtained. The accuracy of this description depends upon both the flow model and the procedure by which the shock motion is determined.

The Mach number of the flow behind the incident shock is 1.26 in the $M_o = 6.0$ case, and 1.31 in the $M_o = 10.2$ case. At these Mach numbers, the supersonic flow near the shock tube wall cannot be turned through the 10^o angle at the cone entrance by means of a stationary, oblique shock. Consequently, as the initial shock enters the cone an upstream-facing shock locally normal to the wall must form outside the entrance*. An unsteady sonic surface behind this shock separates subsonic flow adjacent to the wall from

*This shock is the extension of the third (reflected) shock in the initial Mach reflection occurring within the convergence.

the central supersonic stream. The size of the subsonic region increases as the upstream-facing shock propagates outward from the cone entrance, eventually intersecting upon itself at some position on the shock tube axis. A flow model which assumes that a uniform subsonic region is created by a plane upstream-facing shock is pictured in figure 29. The upstream shock is assumed to propagate at a constant velocity U, resulting in a subsonic flow which subsequently undergoes a steady, isentropic compression in the convergence. Prior to the sonic point for this flow, the reflected shock is assumed to be at an initial position x_o/L with an initial velocity V_{RS_o}.

The corresponding reflected shock motion is found by using Whitham's one-dimensional method (discussed in Part 1.2b) in a manner suggested by Chester (Ref. 39). The differential relation which holds along characteristics overtaking the reflected shock trajectory is applied to the flow conditions immediately behind the shock. The Rankine-Hugoniot relations are used to couple these conditions to the known distribution of flow variables in the steady compression ahead of the shock. The result is a first-order, ordinary, nonlinear differential equation for shock Mach number (or velocity) as a function of position that can be numerically integrated.* The curves shown in

*Details of the formulation can be found in Ref. 39.

figure 29 were obtained by performing the integration for several possible steady flow situations ahead of the $M_o = 6.0$ reflected shock. M_U is the Mach number of the upstream-facing shock, M_5 the Mach number of the steady flow entering the convergence, and $M_{RS}(x_o)$ the initial Mach number of the reflected shock. The initial position and velocity of the reflected shock are chosen to match the $M_o = 6.0$ measurements.

The theoretical curves show a gradual shock deceleration in contrast to the constancy of the observed velocities, but the agreement is still far better than with the similarity solution. The M_U values listed indicate that the upstream-facing shock must be fairly strong $(M_U \sim 2)$ in order for the predicted sonic point of the subsonic compression to be sufficiently near the cone vertex. The initial rise shown in two of the curves results from starting the reflected shock close to the sonic point. It should be noted that Whitham's method neglects modification of the shock motion by re-reflected disturbances (Ref. 16), and in the assumed flow model such disturbances could be important.

4.4c Interactions with Localized Nonuniformities and Secondary Waves

As the incident shock propagates towards the cone vertex, the multiple stemshock growth and reflection process creates a number of local regions within the shocked gas distinguished by sharp gradients in the fluid properties. The gradients in these regions are a result of the discontinuity in shock strength and propagation direction which occurs at the three-shock intersection point in Mach reflection. As sketched in figure 30, a contact surface (OC) is formed which separates fluid that has passed through the original and reflected shocks from the fluid that has passed through the stronger stemshock. Temperature and density are discontinuous across the contact surface, while pressure and flow direction are continuous. Referring to the symbols used in figure 30, the solution of the two-dimensional three-shock theory* for Mach reflection of a Mach six initial shock on a 10^{o} wedge gives the following:

$$T_4/T_3 = \rho_3/\rho_4 = 1.092 \ , \ p_3/p_2 = 1.181$$

$$\chi = 29^{o}\text{-}58' \ , \ \beta = 77^{o}\text{-}54' \ , \ \zeta = 33^{o}\text{-}35'$$

where T is temperature, ρ density, p pressure, and the subscripts refer to the numbered regions in the figure. This solution predicts a 10% difference in temperature and

*The formulation and necessary assumptions in the three-shock theory are outlined in Ref. 40.

density across the contact surface, which should be a good approximation for the first Mach reflection in the convergence until $x/L \sim 0.15$. Beyond this position the axisymmetry results in a rapid increase in the stemshock Mach number near the three-shock intersection (Appendix B), and the differences across the contact surface increase accordingly. A new Mach reflection process begins when the stemshock reaches the cone axis, as shown in figure 31. The incident shock and stemshock roles reverse, and a new contact surface (O'P) is formed between the three-shock intersection and a point (P) moving along the cone axis. Because the contact surface formed by the original Mach reflection (PC) intersects the axis at the same point, this point (hereafter called the contact surface intersection point) separates fluid regions having considerable temperature and density differences. The temperature discontinuities diffuse as the intersection point is convected towards the vertex, and it thus appears to the centerline reflected shock as a small region in which temperature falls rapidly.* The resulting perturbation to the reflected shock motion should be qualitatively similar to the refraction of a plane shock wave by a contact surface separating regions of unequal temperature

*Because of the deceleration of the center shock (M'), the reflected shock experiences a gradual temperature rise prior to this region.

(Ref. 41). The result for the appropriate case is a transmitted shock with a higher Mach number but lower velocity. The centerline reflected shock velocity measurements should therefore show a small interval of deceleration corresponding to the shock passing through each contact surface intersection point.*

The positions where these interactions occur can be estimated from the particle paths shown in figures 17 and 19. The second path in each figure indicates the approximate trajectory of the first contact surface intersection point. In the $M_o = 6.0$ case, this particle path reaches the reflected shock trajectory at $x/L = 0.76$. The reflected shock velocity measurements in figure 15 show a pronounced deceleration starting at $x/L = 0.74$ and ending at $x/L = 0.60$. The last two particle paths in figure 17 indicate that the remaining contact surface intersection points are compressed into the region near the vertex where the piezoelectric probe could not detect the reflected shock. In the $M_o = 10.2$ case, the second particle path reaches the reflected shock trajectory at $x/L \sim 0.82$ (extrapolating from the path termination). The velocity measurements in figure 18 show a small deceleration starting

*Contact surface intersection points are formed at each stemshock intersection point along the cone axis. A corresponding situation occurs on the cone wall (at D in figure 31) as a result of Mach reflection of the center shock on the wall.

at $x/L = 0.83$ and ending at $x/L = 0.75$. The remaining intersection points are compressed beyond $x/L = 0.90$, where too few measured velocities are available for comparison.

The second reflected shock observed in the $M_o = 6.0$ measurements could be the result of a similar interaction in which a sharp gradient in the degree of ionization is also involved. Figure 20 indicates that significant ionization occurs in the fluid shocked beyond the third stemshock intersection point in the $M_o = 6.0$ case, and beyond the first intersection point in the $M_o = 10.2$ case. The particle paths in figures 17 and 19 show that the fluid in these regions is compressed into the final 6% of the convergence in the first instance, and into the final 20% in the second. If a distinct boundary* exists between the region of ionized gas and the adjacent region of cooler, un-ionized gas, the reflected shock will experience a fairly strong interaction. Since the shock passes from a hot gas to a cooler gas at the boundary, the reflected wave in the interaction is probably a shock (as would be the case in one dimension). This secondary shock implodes upon the vertex, reflects, then propagates outward behind the

*Prior to the compression, the boundary corresponds to the contact surface formed at the first stemshock intersection point (PO' in figure 31) where center shock Mach numbers are high enough to produce significant ionization.

primary shock. The process is similar to the generation of secondary shocks when spherical blast waves are produced by detonating finite-diameter spherical charges (Ref. 42). The short interval (~20μsec) between the two shocks in the $M_o = 6.0$ measurements indicates that this interaction must occur very close to the vertex, in accordance with the predicted location of the ionization boundary. In the $M_o = 10.2$ case the region of ionized gas near the vertex is much larger, since the ionization boundary coincides with the first contact surface intersection point. Figure 18 shows only a weak perturbation to the shock velocity at this interaction $(x/L \sim 0.80)$, indicating that the boundary is less distinct. A second reflected shock in this case would therefore be weaker and much farther behind the primary shock (3 to 4 times the $M_o = 6.0$ interval). Although reflected shock measurements which scanned a long time interval after the primary shock failed to show a second shock, the piezoelectric probe may have been too insensitive for detection.

A final source of perturbations to the reflected shock motion is the secondary wave structure generated by the incident shock diffraction. This structure consists of the third (or reflected) shocks formed during each Mach reflection cycle (R and R' in figures 30 and 31, respectively). Simple estimates of the strength of these

waves* show that interactions with the reflected shock should be fairly weak. It can be speculated that the velocity variation observed near the cone entrance in the $M_o = 6.0$ measurements results from such an interaction.

4.4d Thermodynamic Conditions Behind the Reflected Shock

Reasonable estimates of fluid properties behind the reflected shock can not be made from knowledge of only the shock velocity. Approximate upper and lower bounds for the thermodynamic conditions in this flow, however, can be found by using the measured initial and final incident shock Mach numbers as initial conditions for plane reflection of a uniform shock. Equilibrium properties behind plane reflecting shocks in argon have been calculated by Arave and Huseby (Ref. 25) for initial Mach numbers up to 25. In the $M_o = 6.0$ case, the incident shock Mach number at the last measurement position $(x/L = 0.95)$ is $M \sim 18$. For an initial pressure of 1.5 torr and shock Mach number of 18.0, the calculated equilibrium temperature, pressure, and degree of ionization behind a plane reflecting shock are $17{,}600^{\circ}K$, 10.14 atm, and 0.555, respectively. The corresponding conditions for an incident shock Mach number of 6.0 are $7860^{\circ}K$, 0.465 atm, and 0.002. In the $M_o = 10.2$

*The solution of the two-dimensional three-shock theory for the $M_o = 6.0$ case predicts that the third shock has a normal Mach number of 1.07.

case, the final measured Mach number is $M \sim 20$*. Using this value as the incident shock Mach number in plane reflection, the calculated equilibrium temperature, pressure, and degree of ionization are 19,200°K, 14.10 atm, and 0.706, respectively. The corresponding conditions for an incident shock Mach number of 10.2 are 12,100°K, 1.49 atm, and 0.102. Because the reflected shock velocities measured at the cone entrance are considerably higher than the velocities for reflection from a plane end wall (Part 3.2), the lower limits estimated in this manner are probably too low for the fluid properties in the convergence during the time span of the reflected shock measurements. The upper limits should also be somewhat higher, since these estimates fail to consider the compression behind the incident shock in the vertex region.

The thermodynamic conditions near the vertex change considerably during the expansion following incident shock reflection, as indicated by the plane reflection calculations. At the start of the expansion the temperature and electron number density** are quite high, and relaxation processes should be sufficiently rapid for the gas to remain in ionization equilibrium. A subsequent departure from ionization equilibrium occurs if ionization rates fall

---

*Assuming the speed of sound in the test gas has not changed due to radiative preheating.

**Electron number densities are $>10^{18}$ cm^{-3} for both the $M_o = 6.0$ and 10.2 cases, excluding contributions from photoionization and photoemission.

below recombination rates as the temperature and density change. A simple argument by Zeldovich and Raizer (Ref. 13) indicates that such a departure will occur if temperatures fall to fairly low values during a rapid expansion. The ionization rate depends exponentially on temperature as $e^{-I/kT}$, where I is the ionization potential (15.75eV for argon) and k is Boltzmann's constant. For $kT<<I$ the exponential dominates a power-law density dependence, and the ionization rate is very sensitive to decreases in temperature.* On the other hand, recombination processes generally have power-law dependences on temperature and density. Zeldovich and Raizer thus conclude that ionization processes will essentially stop at some time during the expansion, after which the degree of ionization falls with temperature following a power law (while the equilibrium value decreases exponentially). Except at low electron number densities, the predominant recombination mechanism in argon involves three-body collisions (with an electron acting as the third body). In an analysis of this recombination process in supersonic nozzle flows, Bray (Ref. 43) showed that the recombination rate includes a factor which increases exponentially as the electron temperature falls. As a result, the degree of ionization does not "freeze suddenly" during a rapid expansion, but rather decays

*$kT << I$ during the expansion in the experiment, since $I/kT > 10$ near the vertex at the start of the expansion.

gradually at a rate somewhat less than if equilibrium were maintained.

In three-body recombination the electron is captured by the ion into one of the upper levels of the atom. The bound electron then descends down the atomic energy levels very rapidly due to inelastic electron collisions and spontaneous radiative transitions. A portion of the potential energy I from the recombination is thus released in the form of line radiation. The ultraviolet radiation corresponding to transitions to the ground state is the probable source of the thin film gauge signals marked "1" in figure 16a and "2" in figure 16b. These signals are characteristic of such gauges when charged particles are present in the neighboring gas (Refs. 26, 27). The start of the signals coincides with the reflection of the incident shock at the vertex, indicating that radiation from recombination behind the reflected shock is either photoionizing the gas adjacent to the gauge, or causing photoemission from the platinum films. The duration of the signal could be a measure of the time required for recombination to diminish to negligible proportions, and as such would be a rough estimate of the time scale of the expansion. Using the upper and lower bounds obtained from plane reflection calculations, and the signal durations measured from the oscillograms in figures 16a and 16b, an order of magnitude

estimate of the mean cooling rate during the expansion is found to be $\sim 10^8$ $^oK/sec$.

Rapid expansion of a shock heated gas has been suggested by Hurle and Hertzberg (Ref. 9) as a means of producing a population inversion between two electronic energy states. The two states must be optically connected, and the upper state must have a radiative lifetime that is considerably longer (several orders of magnitude) than the lifetime of the lower state. The expansion must be sufficiently rapid to preserve the initial population of the upper state while the lower state decays by emission. If these conditions are satisfied, the population of the lower state will be governed by radiative transitions from the upper state, and a degree of inversion approximately equal to the ratio of the lifetimes of the two states will result. Hurle and Hertzberg calculated that cooling rates of the order of 10^9 $^oK/sec$ could be obtained by expanding shock-heated gas through a slit orifice in a shock tube end wall. This was felt to be sufficient for inverting two electronic states in xenon having radiative lifetimes of 10^{-6} sec and $\sim 10^{-9}$ sec, but experimental efforts to verify the inversion were unsuccessful. In the present experiment the estimated cooling rate behind the reflected shock is an order of magnitude less than that of Hurle and Hertzberg, indicating that the expansion is probably too slow to produce inversions between electronic states. This is certainly true for

the Ar^+ electronic states used in argon-ion discharge lasers, since the upper laser levels in these systems have radiative lifetimes of only 7-10 nsec (Ref. 44). A more likely application of the expansion in the convergence would be the production of population inversions between vibrational energy levels in a shock-heated molecular gas. Such inversions have been successfully produced (Ref. 10) using an expansion from a slit orifice in the manner proposed by Hurle and Hertzberg.

V. CONCLUSIONS

The shock velocity measurements have produced a comprehensive description of the shock dynamics within the convergence, and enabled estimates to be made of the thermodynamic conditions created near the vertex. The incident shock profiles show that the shock behavior is dominated by cyclic diffraction processes which originate at the convergence entrance. Each diffraction cycle is characterized by Mach reflection on the cone wall followed by Mach reflection on the axis. The two-dimensional nature of these processes restricts comparison with the Chester-Chisnell-Whitham and similarity theories, but the basic features of the incident shock profiles are predicted by an approximate axisymmetric diffraction solution due to Storm. Real gas effects, introduced by increasing the initial Mach number and decreasing the initial pressure, alter the incident shock behavior only in a region near the vertex where ionization rates become very rapid. Radiative preheating and the reduction of relaxation times by precursor electrons probably contribute to the sudden decline in shock velocity observed in this region.

The reflected shock profiles show that the shock velocity is nearly constant for much of the convergence length, in contrast to the power-law decline predicted by the similarity solution. During this period the shock

propagates into fluid originally set into steady, uniform motion outside the cone entrance. Small variations in the velocity result from weak interactions with localized nonuniformities and secondary waves. Beyond the cone entrance the shock decelerates towards the velocity corresponding to reflection from a plane end wall.

As a device for generating high-enthalpy gas samples, the conical convergence can produce a small region of very hot, highly compressed fluid near the vertex. Thermodynamic conditions in this region are nonuniform and unsteady, but estimates indicate that temperatures considerably higher than the typical range of conventional, pressure-driven shock tubes can be achieved. A departure from ionization equilibrium is likely near the vertex during the rapid expansion which occurs behind the reflected shock, but the production of inverted populations in electronic energy states is doubtful. A possible application of this expansion is the production of population inversions in the vibrational energy levels of molecular gases.

APPENDIX A

MULTI-CRYSTAL AXIAL PIEZOELECTRIC PROBES

A.1 Background

In principle, the simplest means of measuring shock wave velocity is to determine the time required for the shock to travel between two positions a known distance apart. This has traditionally been the standard procedure in shock tubes, with either thin film heat-transfer gauges or piezoelectric pressure transducers used as sensing elements mounted flush with the tube walls. In the present investigation the rapid changes in shock velocity that were anticipated ruled out these conventional techniques, and a new approach was necessary.

The conical geometry suggested some type of probe that could be inserted at the vertex and positioned continuously along the axis of symmetry. Liepmann and Vlases (Ref. 45) used a piezoelectric disc mounted on the end of a thin rod to detect the shock arrival at various radial positions in an inverse pinch shock tube. Such a probe produces a large local perturbation in the shock motion, however, since the disc axis is perpendicular to the shock. This is unimportant when using a single probe to determine only the shock arrival at the disc position, but prevents the use of two adjacent probes at different radial positions in order to measure a local shock velocity. The present

investigation apparently required a single, sharply-tipped probe containing two or more piezoelectric crystals. This led to consideration of other available crystal geometries, and radially polarized cylindrical tubes (commonly used in underwater acoustic transducers) appeared as the obvious choice. Although the standard diameters of commercially produced piezoelectric tubes are too large for use in the conical convergence, tubes with sufficiently small diameters were fortunately found in a miscellaneous stock list.

A.2 Details of Probe Construction

The final probe configuration used for most measurements is shown in figure 3. As might be expected, this design evolved from a number of successive modifications which proved to be necessary during the initial testing of the probe in the straight shock tube. The design is by no means optimum, but additional modifications would not significantly improve the probe performance.

The primary components in the probe are the PZT-5* cylindrical tubes. When obtained from the manufacturer these crystals are typically 1/8" in diameter, 1/8" long, and have a 0.018" wall thickness. Because the PZT-5

*A lead zirconate/lead titanate piezoelectric ceramic manufactured by the Clevite Corporation, Cleveland, Ohio.

ceramic is rather brittle, machining is not possible. Each crystal is first cut into two tubes 1/16" in length by continuously scoring around the circumference with a razor blade. The tube length is then reduced to 0.043" by grinding the end faces flat (perpendicular to the cylinder axis) using fine grit emory paper. The inside diameter is increased to 0.094" by lapping using a tapered brass rod. A finished crystal is mounted on a 0.094" o.d. stainless steel support tube (cut from hypodermic tubing stock) using a conducting epoxy that will cure at room temperature. The support tubes are approximately 0.30" in length and have a 0.012" wall thickness. Prior to crystal attachment a length of #30 enameled copper wire is soldered onto the inside diameter of the support tube. A "basic two-crystal unit" (figure 3) is formed by joining two crystal support tubes with a 0.124" o.d., 0.094" i.d., fiber-filled phenolic tube machined from 3/16" rod stock. The length of the phenolic spacing tube is precisely measured before assembly, since this length determines the interval over which shock velocities are measured. The other phenolic tubes shown in figure 3 are made similarly, and the remaining stainless steel tubes are cut from available stock sizes. The aluminum tip and collar are machined from rod stock.

When all the components are completed, the entire probe is epoxied* together simultaneously while clamped in

*Resiweld adhesive 7004, produced by the H.B. Fuller Company.

two directions using straight metal strips. This is done to prevent probe curvature resulting from the compounding of individual tolerances. The probe is then polished with fine grit emory paper until all component junctions are smooth. A short length of #30 wire is soldered from the inside diameter of the stainless steel shaft to one pin on a 7-pin miniature connector. The electrical leads from the individual crystal support tubes are soldered to remaining pins on the connector, which in turn is epoxied to the rear of the aluminum collar. The probe construction is completed by using either silver print or diluted conducting epoxy to paint the outside surfaces of the crystals and conducting paths from the crystals to the stainless steel shaft.

The probe shown in figure 3 took between two and three weeks to complete. Increased machining proficiency would have reduced the construction time considerably. The total cost of the materials used was less than $20.00.

A.3 Analysis of Probe Response

A piezoelectric material is characterized by an electro-mechanical coupling, in which strain produced by the application of an external force results in a net electrical charge displacement. Conversely, the application of an electrical field produces a deformation of the material specimen. Ferroelectric materials, such as the PZT-5 cylindrical tubes used in the probes, are both piezoelectric

and pyroelectric. The latter classification describes crystals containing dipoles within the unit cells, and having the property that heating causes a charge displacement. When an external field is applied to a sufficiently heated ferroelectric crystal a number of dipoles become aligned with the field, and upon cooling a preferred polarization axis remains. In this manner the probe crystals were polarized radially during production. The temperature at which a ferroelectric material can gain (or lose) an imposed polarization is called the Curie point. For PZT-5 this temperature is above 350^{o}C, which is sufficiently high for the transient thermal loading typical of most shock tube applications. As an electrical source a piezoelectric crystal behaves like a voltage generator in series with a high capacitance. The output impedance is typically quite high (approximately 2000 ohms for a probe crystal), and cathode-follower circuits are commonly used to match the impedances of connecting cables. This was not done for the probe crystals.

Static relations between applied stresses and resultant voltages for a variety of crystal geometries and polarizations can be obtained by combining manufacturer's specifications (for example, Ref. 46) and elastic theory solutions (for cylindrical tubes, Ref. 47). For a PZT-5 cylindrical tube with outer radius b, inner radius a, and shielded ends, the open circuit output voltage V as a

function of externally applied pressure p is predicted to be

$$V = \pm 32.4\ bp\left[\left(\frac{b-a}{b+a}\right) - 0.435\right] \text{ millivolts}$$

where a and b are in centimenters, p is in millimeters of mercury, and the sign depends upon the polarization direction. Using the dimensions of the probe crystals, this gives

$$V = \pm 1.51\ p \text{ millivolts}$$

This formula is inaccurate, since the inside diameter of the crystal is fastened to a stainless steel support tube. This effectively reduces the inner radius a, resulting in a smaller numerical factor on the right-hand side. The factor vanishes if the ratio $a/b = 0.394$ (the crystal dimensions give $a/b = 0.758$). The support tubes apparently lowered the effective value of the ratio close to this limit, for the crystals were found to be practically insensitive to static pressure changes. The probe signals displayed no DC shift when subjected to a uniform radial compression after shock passage, as shown by the characteristic responses in figure 4.

The signals in figure 4 are transient, high frequency oscillations corresponding to fundamental ringing modes of the piezoelectric crystals. This ringing results from the

shock acting like a stepload moving along the finite cylinder length. A theoretical analysis of the signal generated by the shock during its transit along the crystal would be quite difficult, due to the cylindrical geometry and the uncertain boundary conditions. Most theoretical work on stresses produced by moving loads has been limited to very simple geometries and load distributions (Refs. 48, 49). A response analysis, therefore, must be confined to identifying the observed modes of crystal oscillation, and determining the shock position relative to the crystal for some characteristic point on the probe signal.

For simpler geometries, natural ringing frequencies can be predicted if the crystal dimensions and acoustic wave speeds are known. In a piezoelectric ceramic like PZT-5 a large number of acoustic speeds can be defined, depending upon the type of wave and its orientation with respect to the polarization axis. For the present considerations the relevant speeds* in cm/μsec are as follows (Ref. 46):

V_1 = velocity of dilatational wave parallel to polar axis (no boundary conditions) = 0.380

V_2 = velocity of shear wave perpendicular to polar axis with particle displacement parallel to polar axis (infinite plate) = 0.226

*Assuming open external circuit conditions

V_3 = velocity of shear wave parallel to polar axis = 0.226

V_4 = velocity of Rayleigh surface wave (longitudinal wave in limit of small wave length) = 0.210

V_5 = velocity of longitudinal wave perpendicular to polar axis (infinite plate) = 0.312

These standard wave speeds are for idealized geometries, and can only be used for estimates when considering the cylindrical piezoelectric tubes. An additional complication is the mismatch in acoustic impedance which occurs at every crystal surface. Nevertheless, approximate ringing frequences can be defined as follows:

$$f_1 = V_1/2\tau = 4.96 \text{ MHz}$$
$$f_2 = V_2/2h = 1.04 \text{ MHz}$$
$$f_3 = V_3/2\tau = 2.96 \text{ MHz}$$
$$f_4 = V_4/2h = 0.96 \text{ MHz}$$
$$f_5 = V_5/2h = 1.43 \text{ MHz}$$

where τ and h are the crystal wall thickness and length, respectively. f_1 and f_3 correspond to radial ringing modes, while the remaining frequencies are for longitudinal (axial) modes.

The initial response of the probe crystals can be classified according to the local shock velocity. For velocities less than 0.25 cm/μsec (Mach numbers below 7.8)

the time from the first observable response to the first positive peak (initial rise time) is considerably longer than the time required by the shock to traverse the crystal length (shock traverse time). The initial ringing frequency is nearly constant for each crystal, though varying between crystals from 1.43 MHz to 1.59 MHz*. For shock speeds between 0.25 cm/μsec and 0.45 cm/μsec (Mach numbers less than 14) the initial rise times are comparable to the shock traverse times, and the ringing frequencies are unchanged. As shock velocities increase above 0.45 cm/μsec the response of the crystals progressively changes. The initial rise time decreases more rapidly than the shock traverse time. A small negative peak appears prior to the first positive peak, and a high-frequency ringing becomes superimposed on the 1.5 MHz signal. For velocities above 0.65 cm/μsec (Mach numbers above 20) the response is completely dominated by the high-frequency ringing, which varies between crystals from 5.6 to 6.0 MHz.

By comparing the observed ringing frequencies with the resonant frequencies predicted by the approximate acoustic speeds, certain conclusions can be made. For most of the shock velocities measured in the experiment the fundamental crystal response is a longitudinal (axial)

---

*The convention used in obtaining these values is to measure the oscillation period between the first two positive peaks on an oscillogram trace (figure 4).

ringing mode, with the corresponding acoustic velocity slightly higher than V_5 . For the highest shock velocities the fundamental response changes to a radial mode, with the corresponding acoustic velocity somewhat larger than V_1 . In the narrow range of shock speeds for which two modes are superimposed, the time required for the shock to traverse the crystal length is nearly equal to the period of radial ringing. For lower velocities the shock traverse time is longer than the radial ringing period, and for higher velocities the traverse time is less. Thus, the ratio of shock traverse time to radial ringing period apparently determines when the fundamental response mode changes. The long initial rise time at the lower velocities appears to consist of the shock traverse time preceded by a period in which signals are generated by precursor disturbances in the probe. For shock wave velocities above 0.25 cm/μsec the shock is apparently "supersonic" with respect to the velocity of these disturbances, and the rise time primarily depends upon the shock traverse time. The fact that the signal prior to the first positive peak is strongly shock velocity dependent, while after this peak little dependence is apparent, indicates that the first positive peak corresponds to the shock arrival at the rear crystal face. This is the basic assumption used in the data reduction, and the test measurements shown in figure 5 verify that it gives consistent results. The small initial

negative peak, which is used for data reduction at higher shock velocities (Part 2.4), must be associated with the shock arrival at the front crystal face. By adding a fixed correction when measuring times to this signal, the variation in shock traverse time is neglected. Over the range of velocities for which this convention is used this corresponds to an error of ± 0.03 μsec, or at most 2%.

A.4 Shock Diffraction Effects

In order for the piezoelectric probe to accurately measure shock velocity at one or more positions, the interaction between the shock wave and the probe must not significantly perturb that portion of the shock running along the probe surface. This interaction consists of Mach reflection of the shock on the conical probe tip, followed by an "expansion" of the stemshock at the tip shoulder. In the initial process the locus of successive three-shock intersection points forms a constant angle χ with the probe axis (as in the two-dimensional case shown in figure 30). The stemshock is curved, and decreases in strength from the cone surface to the intersection point. When the stemshock reaches the tip shoulder, an "expansion" characteristic of shock diffraction at a convex corner occurs. The expansion effects a growing portion of the stemshock, in which Mach numbers are reduced.

Whitham (Ref. 31) considered the diffraction of strong shock waves by slender bodies. He found that for a high

initial Mach number M_o and small cone angle θ_w, the stemshock Mach number at the cone surface M_w is given by

$$\frac{M_w}{M_o} - 1 = \theta_w^2 \left[\log \frac{1}{\theta_w} - 0.619 \right]$$

For the 7^o total-angle tip used in the final probe design, this formula predicts $M_w/M_o = 1.008$. Beyond the tip shoulder the local shock Mach number will drop due to the "expansion", perhaps undershooting the expected final value of $M_w = M_o$. Since Whitham's formula predicts a Mach number increase at the cone surface of less than 1%, it is doubtful that larger deviations will occur after the shock passes the tip shoulder. The measurements shown in figure 5 confirm the small magnitude of the shock velocity perturbations.

APPENDIX B

AN AXISYMMETRIC SHOCK DIFFRACTION SOLUTION DUE TO E. STORM

The diffraction of a plane shock wave in a conical convergence is obviously a complex process involving a number of two-dimensional wave interactions. An accurate analysis that takes into account all possible factors (such as secondary waves, re-reflected disturbances, and real gas effects) is simply not feasible. Whitham (Refs. 30, 31) developed an approximate theory for investigating shock diffraction problems in which disturbances to the flow are treated as a wave propagation on the incident shock. In two-dimensional problems the successive shock positions and rays locally normal to these positions are used as orthogonal coordinates. One relation between the local shock Mach number and the distance between adjacent rays follows from geometry, and a second is obtained from the CCW theory by assuming that adjacent rays act like channel walls. Combining the two relations results in a second-order hyperbolic equation which displays wave motion analogous to one-dimensional, unsteady gasdynamics. Mach reflection at a wall inclination appears as a compressive wave on the incident shock, and because of nonlinearities the wave breaks to form a "shock-shock". This shock-shock is in fact the three-shock intersection point, and the theory is correct to the extent that effects of the reflected (third) shock can

be ignored. In three-dimensions the formulation is basically the same, except Cartesian coordinates prove to be more practical.

Following Whitham's approach, Mr. Erik Storm obtained an approximate solution for the axisymmetric diffraction of a normal shock entering a conical convergence. A preliminary description of the solution can be found in Reference 22, but a complete account has not been published. This appendix will be confined to a summary of the basic equations and assumptions. The motion of the shock is described by the form

$$a_o t = \alpha(x,r) \quad .$$

where a_o is the sound speed in the undisturbed gas, x is distance along the axis of symmetry, r is radial position from this axis, and $\alpha(x,r)$ defines the shock position at a particular time t. If M is the local shock Mach number and $\theta(x,r)$ is the local angle between a ray and some fixed direction (parallel to the cone axis), then

$$\alpha_x = \frac{\cos\theta}{M} \quad \text{and} \quad \alpha_r = \frac{\sin\theta}{M}$$

so that

$$\frac{\partial}{\partial x}\left(\frac{\sin\theta}{M}\right) - \frac{\partial}{\partial r}\left(\frac{\cos\theta}{M}\right) = 0 \qquad (1)$$

If A is proportional to the area of a ray tube, Whitham's geometrical relation in axisymmetric coordinates takes the form

$$\frac{\partial}{\partial x}\left(\frac{r\cos\theta}{A}\right) + \frac{\partial}{\partial r}\left(\frac{r\sin\theta}{A}\right) = 0 \tag{2}$$

Considering a small ray tube intersecting the surface of successive shock-shock positions (hereafter called the shock-shock trajectory), the continuity of α and the conservation of $\frac{M\nabla\alpha}{A}$ results in the following jump conditions:

$$\tan(\theta_1-\theta_o) = -\frac{\left((M_1/M_o)^2-1\right)^{\frac{1}{2}}\left(1-(A_1/A_o)^2\right)^{\frac{1}{2}}}{1+(A_1M_1/A_oM_o)} \tag{3}$$

$$\tan(\chi-\theta_o) = \left(\frac{(M_1/M_o)^2-1}{1-(A_1/A_o)^2}\right)^{\frac{1}{2}} \tag{4}$$

where the subscripts "o" and "1" refer to conditions before and after the shock-shock trajectory, respectively, and $\chi(x,r)$ is the local angle between the trajectory and the reference direction used in defining θ. A final relation between A and M follows from the CCW theory in the strong shock limit:

$$A/A_o = (M_o/M)^n \;;\quad n = 2\sqrt{\frac{\gamma-1}{2\gamma}} + 1 + \frac{2}{\gamma} + \frac{1}{\gamma}\sqrt{\frac{2\gamma}{\gamma-1}} \tag{5}$$

After using (5) to eliminate A, (1) and (2) form a set of equations for the two dependent variables M and θ, subject to the jump conditions (3) and (4) and the boundary condition at the wall ($\theta = \theta_w$). To solve this system of equations, numerical techniques employing the method of characteristics are necessary (analogous to the methods used for two-dimensional, steady, supersonic flow).

In his solution Storm avoids the formidable computational work required to solve Whitham's full equations. Equations (1) and (2) in characteristic form become:

$$d\theta + \frac{\sqrt{n}}{M} dM + \frac{\tan\theta}{\sqrt{n}\tan\theta + 1} \frac{dr}{r} = 0 \qquad (6)$$

$$\text{on} \qquad \frac{dr}{dx} = \frac{\sqrt{n}\tan\theta + 1}{\sqrt{n} - \tan\theta}$$

and

$$d\theta - \frac{\sqrt{n}}{M} dM + \frac{\tan\theta}{1 - \sqrt{n}\tan\theta} \frac{dr}{r} = 0 \qquad (7)$$

$$\text{on} \qquad \frac{dr}{dx} = -\frac{1 - \sqrt{n}\tan\theta}{\sqrt{n} + \tan\theta}$$

Equation (7) is a differential relation that holds on characteristics which originate at the cone wall and arrive at the shock-shock. Following the method used by Whitham is his formulation of the CCW theory (Ref. 16), Storm applies this equation to the conditions immediately behind the shock-shock trajectory. These conditions are then related to the initial conditions by means of the

jump relations (3) and (4). No rigorous justification for this procedure is attempted, but it is suggested by an extension of the analogy between two-dimensional shock diffraction on a wedge and the steady one-dimensional piston problem. In this analogy the fixed wedge angle (in a Cartesian plane) corresponds to the constant piston velocity (in a distance versus time plane), and the resulting constancy of the shock-shock angle χ corresponds to the steady velocity of the piston-driven shock wave. When extended to the axisymmetric case, this analogy calls for the shock-shock trajectory to behave like the shock produced by a converging cylindrical piston. This in turn suggests the application of Whitham's method. The solution for the first shock-shock trajectory reduces to solving:

$$\frac{r}{R} = \exp - \left[\int_{Z_{2-D}}^{Z} g(u) \left(G(u) + \frac{\sqrt{n}}{u} \right) du \right] \tag{8}$$

with $$g(u) = \sqrt{n} + \frac{u(u^{n-1}+1)}{\sqrt{u^2-1}\,\sqrt{u^{2n}-1}} ,$$

$$G(u) = \frac{u^{n-1}+1}{\left(u^{n+1}+1\right)^2} \frac{\sqrt{u^2-1}}{\sqrt{u^{2n}-1}} \left[n + u^2 \frac{u^{2n}-1}{u^2-1} + (n-1) \frac{u^{2n}-1}{u^{n-1}+1} \right],$$

$$Z = \frac{M_1(x,r)}{M_o} , \quad Z_{2-D} = \frac{\cos(\chi_{2-D} - \theta_w)}{\cos \chi_{2-D}}$$

where R is the initial cone radius, u is simply an integration variable, and χ_{2-D} is given by Whitham's solution for shock diffraction on a 10° half-angle wedge. The computational procedure is as follows:

1. A series of values for M_1/M_o are chosen, and equation (8) is integrated numerically to find the corresponding r/R.
2. For each pair of values for M_1/M_o and r/R, χ follows from equations (4) and (5).
3. For each set of M_1/M_o, r/R, and χ values, the corresponding x/R is obtained from

$$\frac{x}{R} = \int_{r/R}^{1} \frac{1}{\tan\chi}\, d(r/R)$$

These computations give the shock-shock trajectory and the stemshock Mach number along this curve. The ray inclination along the trajectory (θ_1) is found at each point using equation (3). The results show that χ, M_1, and θ_1 all increase monotonically as the cone axis is approached. In the limit $r/R \to o$, χ and θ_1 approach $\pi/2$ and $M_1 \to \infty$. This singular behavior only appears for extremely small values of r/R. The stemshock Mach number adjacent to the wall can be estimated by applying equation (5) to a ray tube bounded by the wall and a neighboring ray. The initial inclination of this ray is taken to be the first value of θ_1 found in the computation, and the area of the ray tube

at any position follows by assuming the ray remains straight. The result is a gradual monotonic rise in the Mach number for increasing x.

A number of assumptions are necessary in order to continue the solution beyond the first stemshock intersection point. To avoid the singularity at $r/R = 0$ the stemshock must intersect on a finite radius boundary. In the calculations this boundary is taken to be the surface of the piezoelectric probe. Using the computed values of M_1 and θ_1 at this position, a locally plane stemshock is assumed to diffract two-dimensionally on the probe surface. This gives the initial conditions required for the computation of the second shock-shock trajectory. For convenience a coordinate system centered at the first intersection point is now used. The method of solution is the same, but the procedure is complicated considerably by the fact that the initial Mach number and ray direction at the shock-shock are unknown. Storm estimates these quantities by assuming that rays remain straight between the first and second shock-shock trajectories. The initial Mach numbers along the second trajectory then follow from corresponding values along the first using the CCW area - Mach number relation. The Mach number of the center shock along the probe surface is found by applying the relation to an adjacent ray tube, again assuming that the bordering ray remains straight.

The numerical calculation is arbitrarily discontinued when the second shock-shock trajectory reaches the cone wall. Subsequent cycles of Mach reflection on the cone wall followed by Mach reflection on the axis can be approximated by assuming that in each cycle the center shock is initially plane and uniform. The diffraction is then a duplication of the first cycle, and the initial calculations are repeated after appropriate scale changes.

REFERENCES

1. Bradley, J. M., Shock Waves in Chemistry and Physics, John Wiley & Sons, Inc., New York (1962).

2. Vieille, P., C. R. Acad. Sci. Paris 129, 1228 (1899).

3. Reynolds, G. T., OSRD Report No. 1519 (1943).

4. Bleakney, W., Weimer, D., and Fletcher, J., Rev. Sci. Instr. 20, 807 (1949).

5. Bleakney, W., and Taub, A. H., Rev. Mod. Phys. 21, 584 (1949).

6. Benner, S. S., Harshbarger, F., and Vali, V., Combustion Researches and Reviews 1957, p. 134, Butterworths & Co., Ltd., London (1957).

7. Ferri, A. (ed.), Fundamental Data Obtained from Shock Tube Measurements, AGARDograph No. 41, Pergamon Press, New York (1961).

8. Zel'dovich, Ya. B., Soviet Phys. JETP (Eng. Transl.) 5, 919 (1957).

9. Hurle, I. R., and Hertzberg, A., Phys. Fluids 8, 1601 (1965).

10. Kuehn, D., and Monson, D., Appl. Phys. Letters 16, 48 (1970).

11. Guderley, G., Luftfarhtforschung 19, 320 (1942).

12. Butler, D.S., Armament Research Establishment Report 54/54 (195).

13. Zel'dovich, Ya. B., and Raizer, Yu, P., Physics of Shock Waves and High-Temperature Hydrodynamic Phenomena, Vols I & II, English Translation edited by W. O. Hayes and R. F. Probstein, Academic Press, New York (1966).

14. Chester, W., Phil. Mag. (7) 45, 1293 (1954).

15. Chisnell, R. F., J. Fluid Mech. 2, 286 (1957).

16. Whitham, G. B., J. Fluid Mech. 4, 337 (1958).

17. Bird, G. A., J. Fluid Mech. 5, 60 (1959).

REFERENCES (cont.)

18. Belokon', V. A., Petrukhin, A. I., and Proskuryakov, V. A., Soviet Physics JETP (Eng. Transl.) 21, 33 (1965).

19. McEwan, A. D., Australian Defense Scientific Service Aerodynamics Note 298 (1968).

20. Russel, D. A., J. Fluid Mech. 27, 305 (1967).

21. Dvir, M., Low, W., Stricker, J., and Maniv, S., Phys. Fluids 4, 1600 (1966).

22. Storm, E., Paper presented at AIAA 20th Annual Region VI Student Conference, San Luis Obispo, California (May, 1970).

23. Smith, J. A., Ph.D. Thesis, California Institute of Technology (1967).

24. Resler, E. L., Lin, S., and Kantrowitz, A., J. Appl. Phys. 23, 1390 (1952).

25. Arave, R., and Huseby, O., Boeing Report No. D2-11238 (1962).

26. Jahn, R. G., and Grosse, F. A., Phys. Fluids 2, 469 (1959).

27. Jahn, R. G., and Weiner, D., J. Appl. Phys. 29, 741, (1958).

28. Petschek, H., and Byron, S. R., Ann. Phys. 1, 270 (1957).

29. Wong, H., and Bershader, D., J. Fluid Mech. 26, 459 (1966).

30. Whitham, G. B., J. Fluid Mech. 2, 145 (1957).

31. Whitham, G. B., J. Fluid Mech. 5, 369 (1959).

32. Wong, H., and Horn, K., Am. Phys. Soc. 5th Shock Tube Symp., U. S. Naval Ordnance Laboratory, Silver Spring, Maryland (April, 1965).

33. Heaslet, M. A., and Baldwin, B. S., Phys. Fluids 6, 781 (1963).

34. Lederman, S., and Wilson, D. S., AIAA J. 5, 70 (1967).

REFERENCES (cont.)

35. Ferrari, C., and Clarke, J. H., Supersonic Flow, Chemical Processes, and Radiative Transfer, ed. by D. B. Olfe and V. Zakkay, Pergamon Press, New York (1964).

36. Dobbins, R. A., AIAA Paper No. 68-666 (1968).

37. Hollyer, R. N., Johns Hopkins University Applied Physics Laboratory Report No. CM-903 (1957).

38. Payne, R. B., J. Fluid Mech. 2, 185 (1957).

39. Chester, W., Adv. Appl. Mech. VI, 120 (1960).

40. Polachek, H., and Seeger, R. J., Proc. Symp. Appl. Math. 1, 119 (1949).

41. Glass, I. I., and Patterson, G. N., J. Aero Sci. 22, 73 (1955).

42. Brode, H. L., Phys. Fluids 2, 217 (1959).

43. Bray, K. N. C., The High Temperature Aspects of Supersonic Flow, ed. by W. C. Nelson, Macmillan Co., New York (1964).

44. Bennett, W. R., Kindlmann, P. J., Mercer, G. N., and Sunderland, J., Appl. Phys. Letters 5, 158 (1964).

45. Liepmann, H. W., and Vlases, G., Phys. Fluids 4, 927 (1961).

46. "Piezoelectric Technology Data for Engineers," Clevite Corporation, Piezoelectric Division, Bedford, Ohio (1965).

47. Langevin, R. A., J. Acous. Soc. Am. 26, 421 (1954).

48. Morley, L. S. D., British R & M No. 3266 (1962).

49. Cole, J., and Hath, J., J. Appl. Mech. 25, 433 (1958).

50. Emrich, R. J., Am. Phys. Soc. 5th Shock Tube Symp., U.S. Naval Ordnance Laboratory, Silver Spring, Maryland (April, 1965).

REFERENCES (cont.)

51. Johnson, D. S., A.E. Thesis, California Institute of Technology (1962).

52. Clarke, J. F., and McChesney, M., The Dynamics of Real Gases, Butterworth & Co., Ltd., London (1964).

53. Skifstad, J. G., ARL 70-0343 (1970).

TABLE 1

Comparison of Exponents in Shock Velocity Power Law

γ	Cylindrical Shock		Spherical Shock	
	$(1-\alpha)/\alpha$	$jK/2$	$(1-\alpha)/\alpha$	$jK/2$
6/5	0.161220	0.163112	0.320752	0.326223
7/5	0.197294	0.197070	0.394364	0.394141
5/3	0.226054	0.225425	0.452692	0.452108

TABLE 2

Relaxation Distances and Times for Incident Shock Velocity Profiles (Ref. 29)

Test gas: 1.5 torr argon

Impurity level: $\sim 5 \times 10^{-5}$

Nomenclature: R = cone radius (cm)
ℓ = relaxation distance (cm)
τ = relaxation time (μsec)
d = distance to previous intersection point (cm)

Distances and times in laboratory frame of reference

		$M_o = 6.0$		$M_o = 10.2$		
x/L	R	ℓ	τ	ℓ	τ	d
0.46	4.13	*	*	7	17	6.8
0.73	2.07	*	*	1.2	2.1	3.8
0.86	1.07	10	23	0.6	0.8	1.9/1.5**
0.92	0.61	1.6	3.1	0.5	0.7	1.1/1.7

*Relaxation region quite long, but equilibrium conditions nearly the same as "frozen" conditions behind shock front

**First value for $M_o = 6.0$, second for $M_o = 10.2$

TABLE 3

Ratios of Relaxation Distance to Cone Radius at $x/L = 0.86$

Test gas: argon

Impurity level: $\sim 5 \times 10^{-5}$

Nomenclature: M = local shock Mach number
p_1 = initial test gas pressure
R, ℓ = same as Table 2

Relaxation distances from Ref. 29 (laboratory reference frame)

	ℓ/R	
M	p_1 = 1.5 torr	p_1 = 0.5 torr
14	5.4	16
16	2.0	5.9
18	1.0	3.0
20	0.6	1.9
22	0.4	1.3

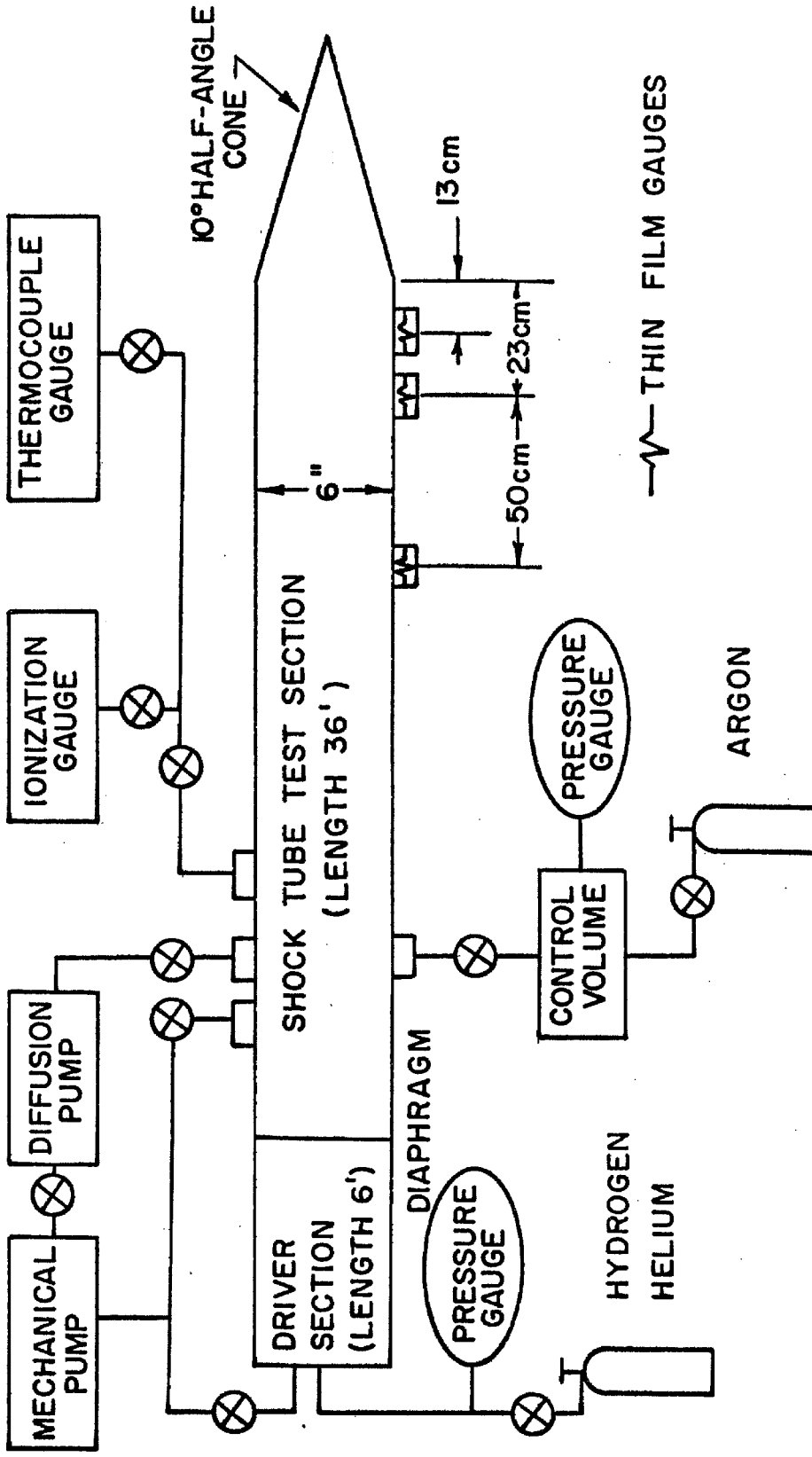

Figure 1. GALCIT Six-inch Shock Tube

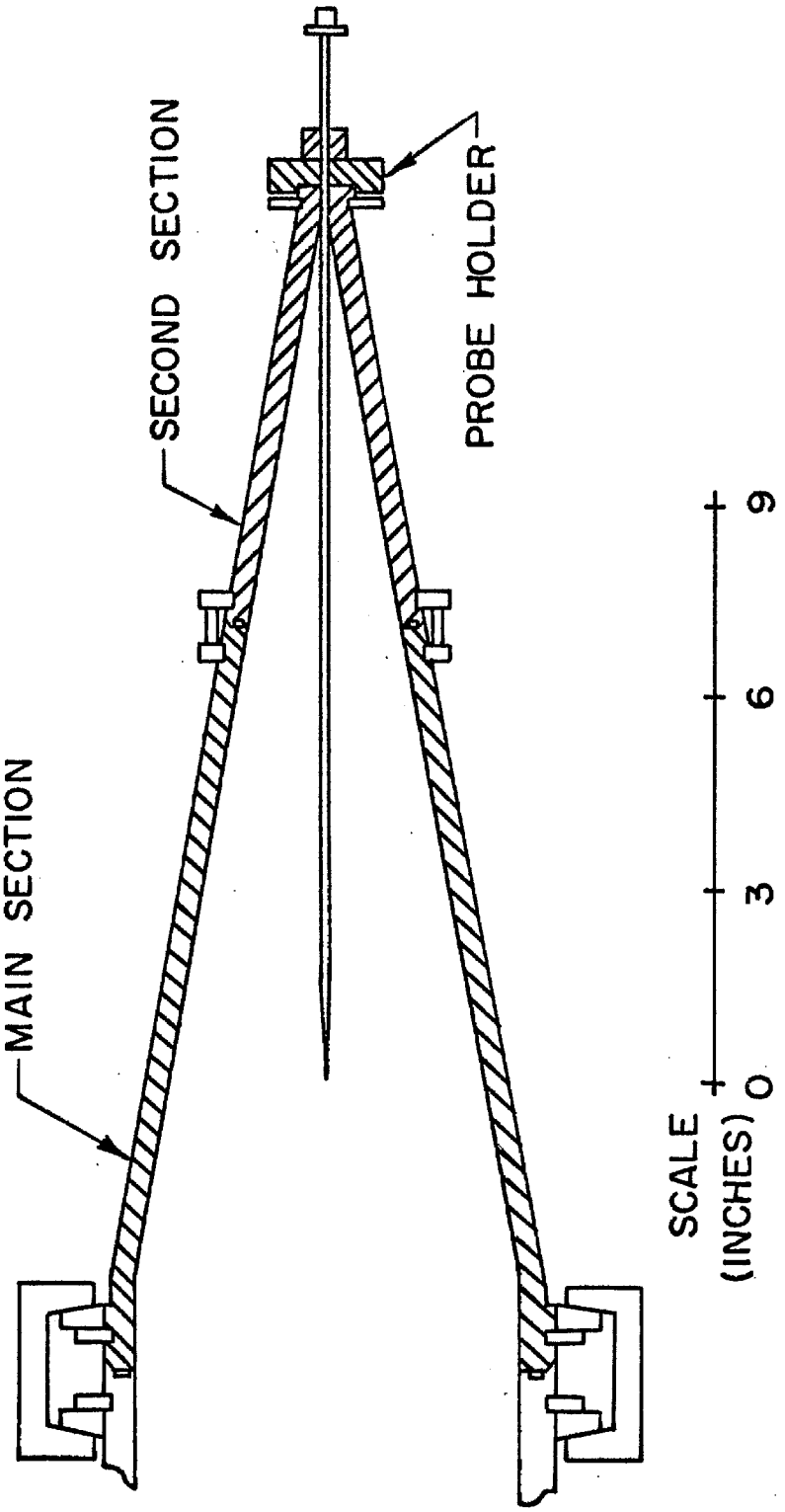

Figure 2. 10^{o} Half-angle Conical Convergence

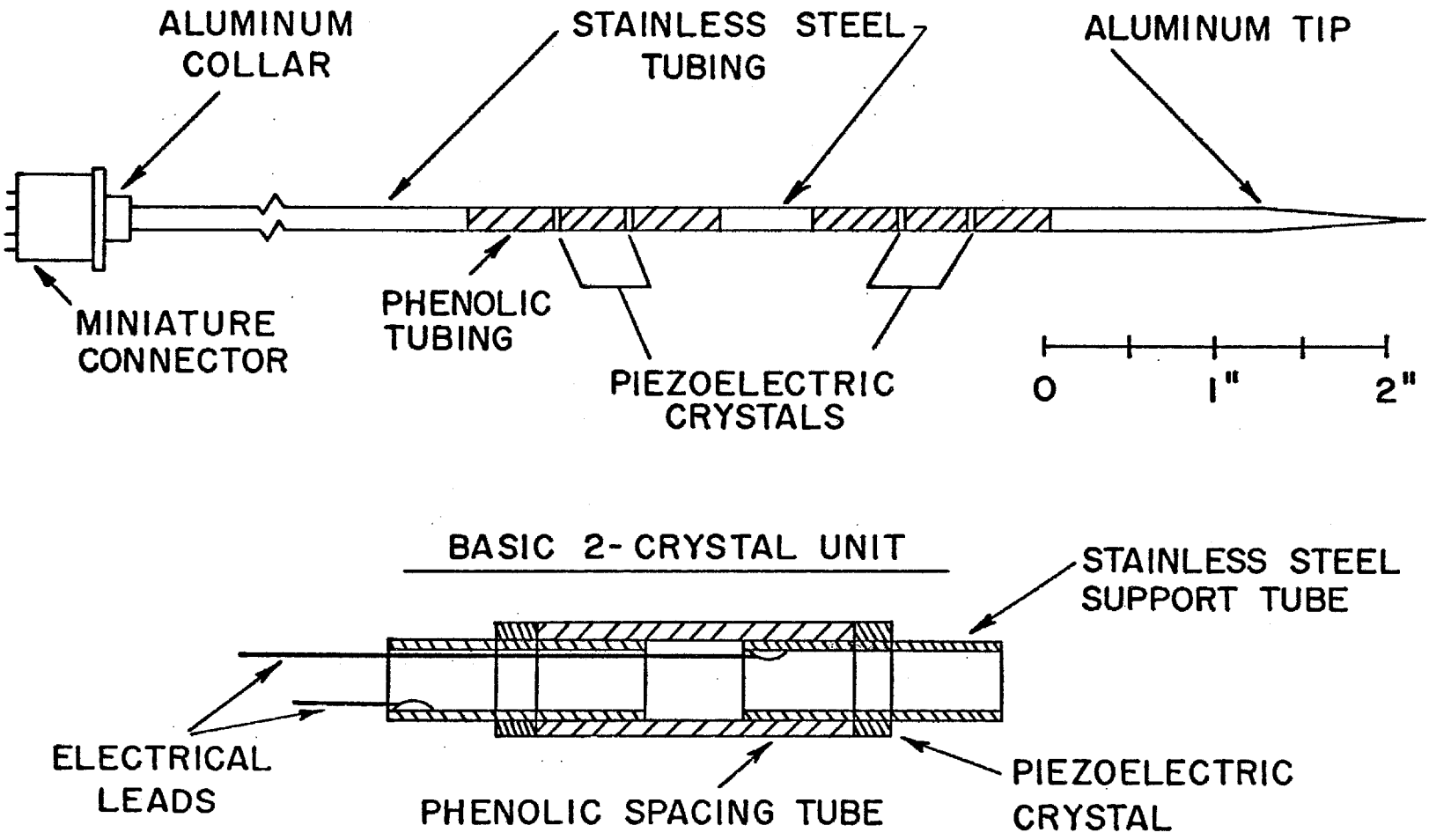

Figure 3. Multi-crystal Piezoelectric Probe

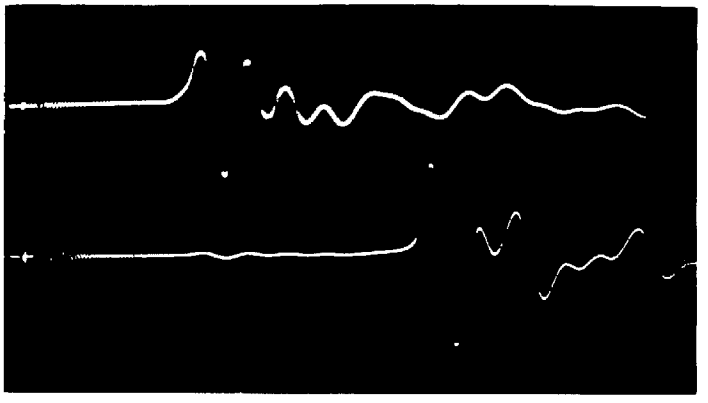

M = 10.0

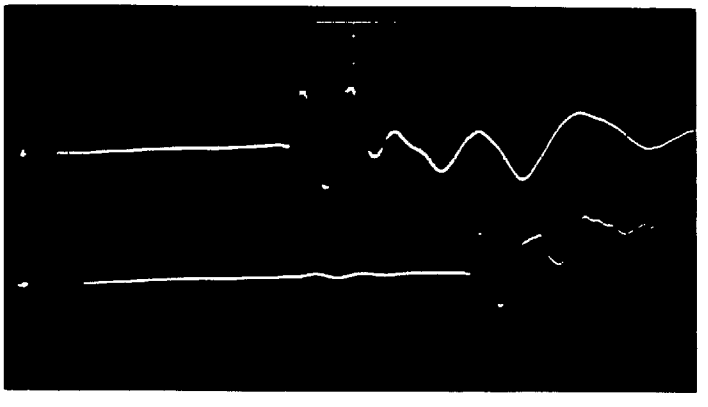

M = 13.7

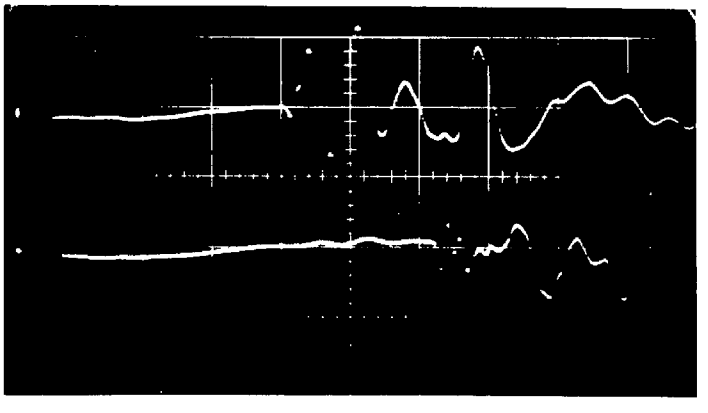

M = 17.6

Sweep Rates: 1μsec/div.

Sensitivities: Upper Beam 0.2v/div.
Lower Beam 0.1v/div.

Test gas: 1.5 torr argon

Figure 4. Characteristic Piczoelectric Probe Responses

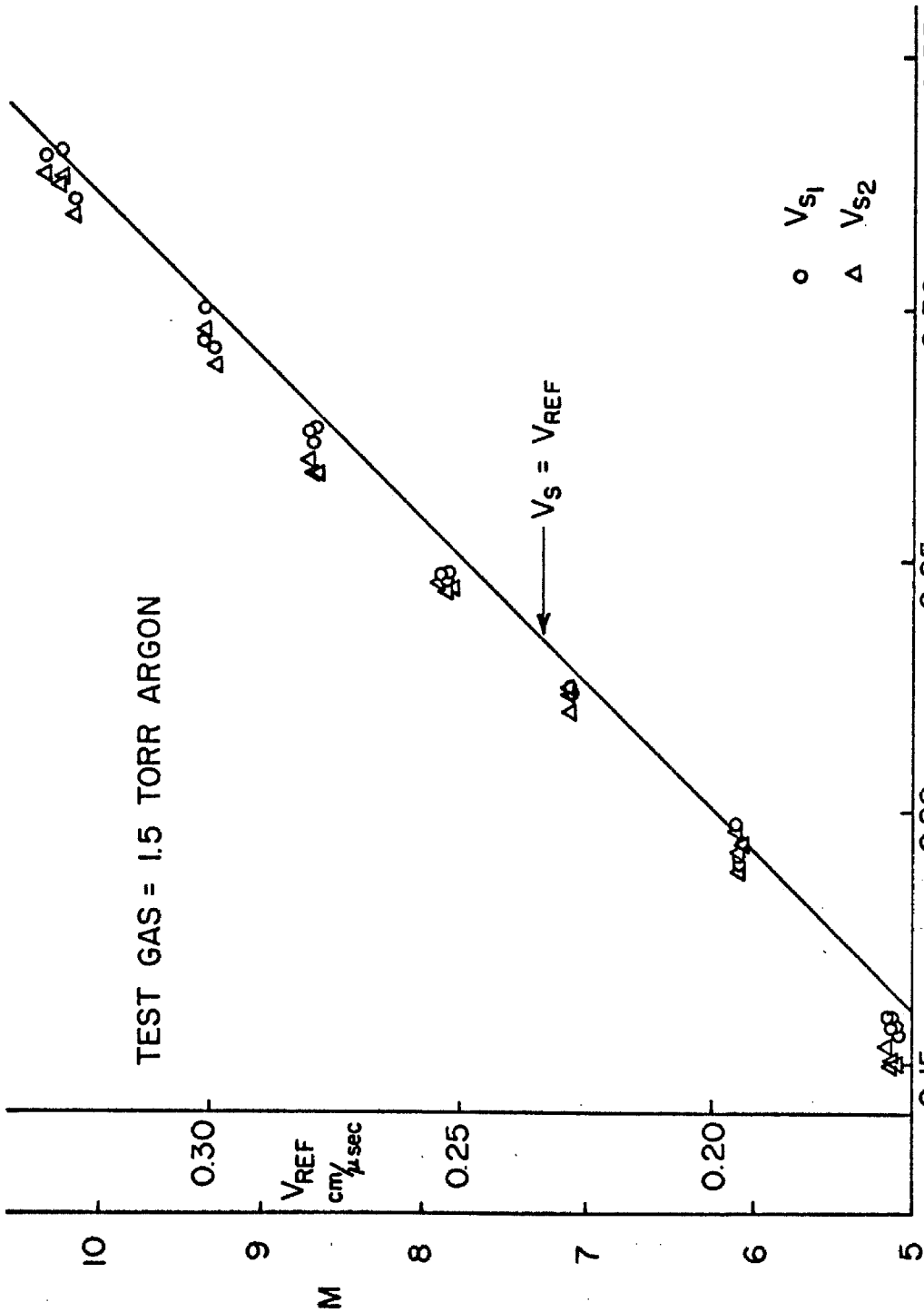

Figure 5. Shock Velocity Measurements in the Straight Shock Tube

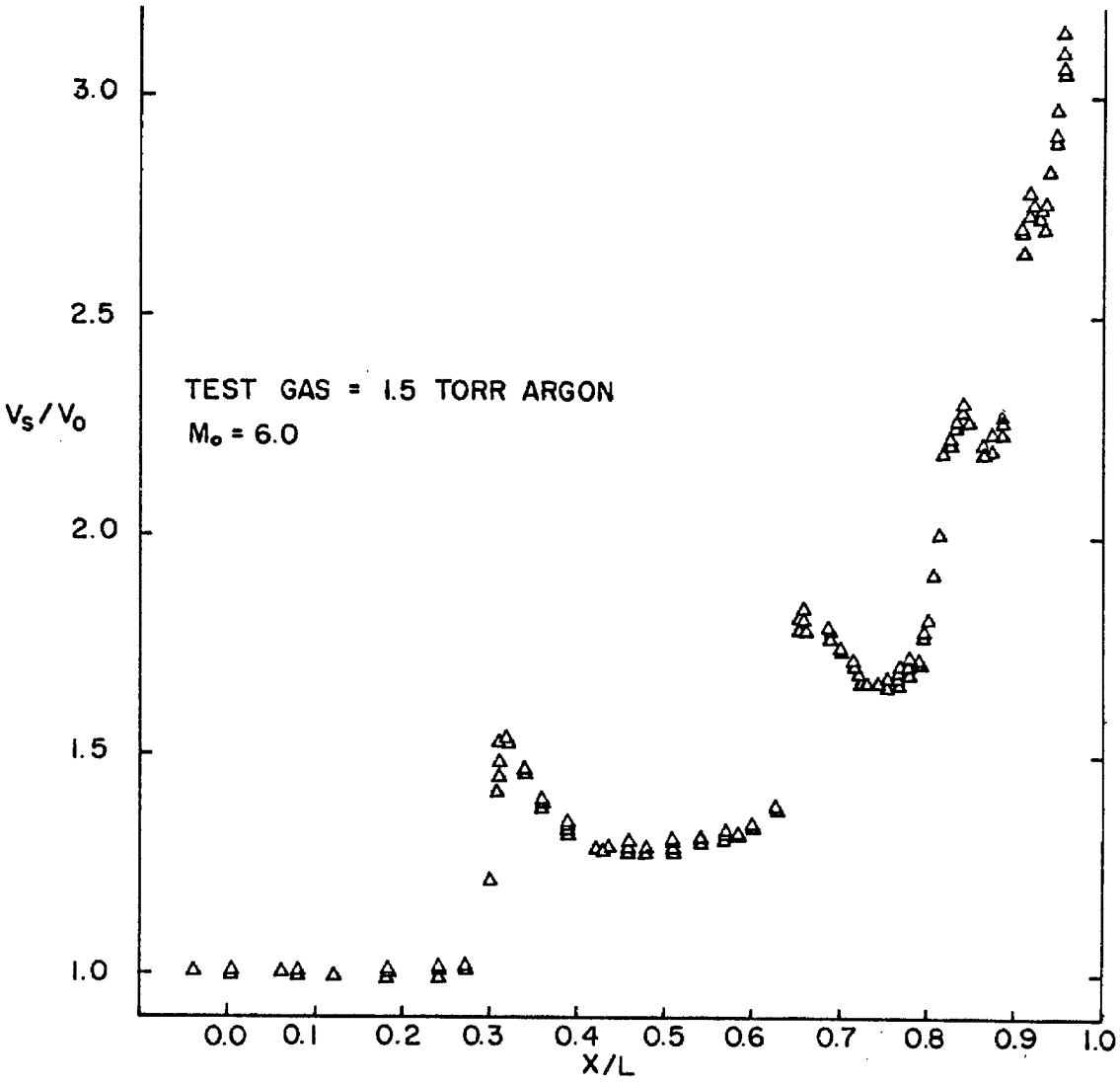

Figure 6. M_o = 6.0 Incident Shock Velocity

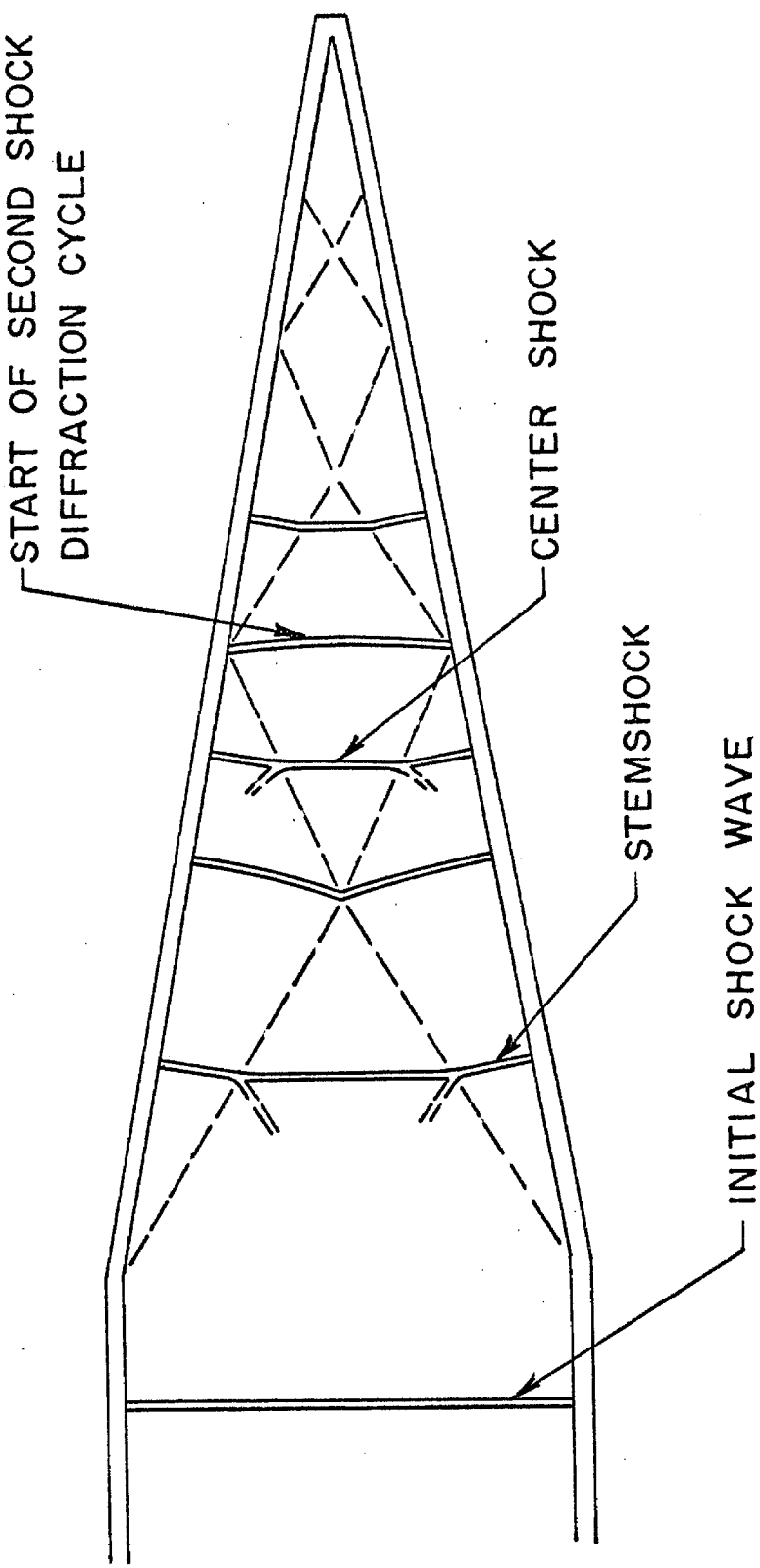

Figure 7. Diffraction of Incident Shock

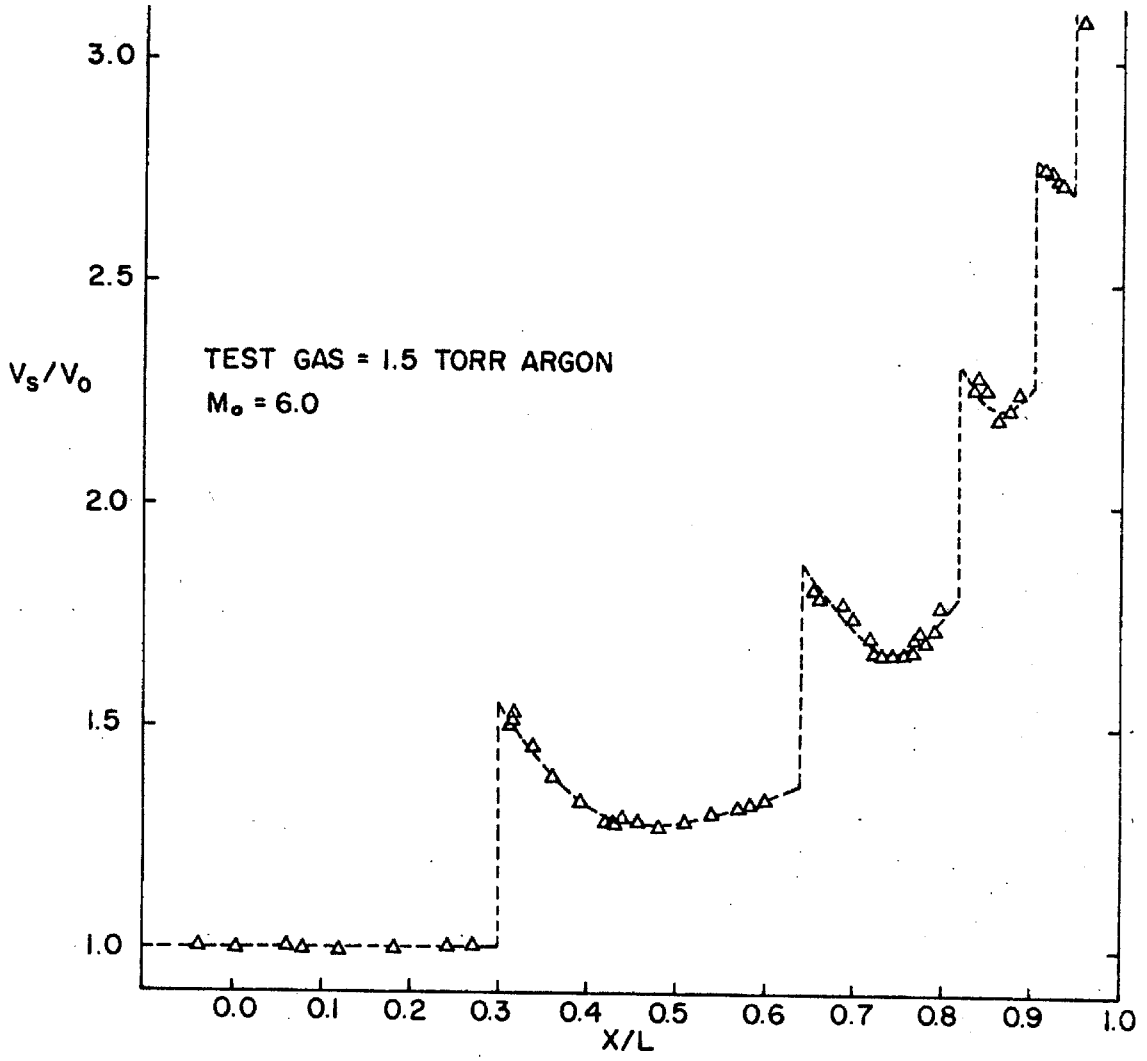

Figure 8. M_O = 6.0 Incident Shock Velocity and Stemshock Intersection Points

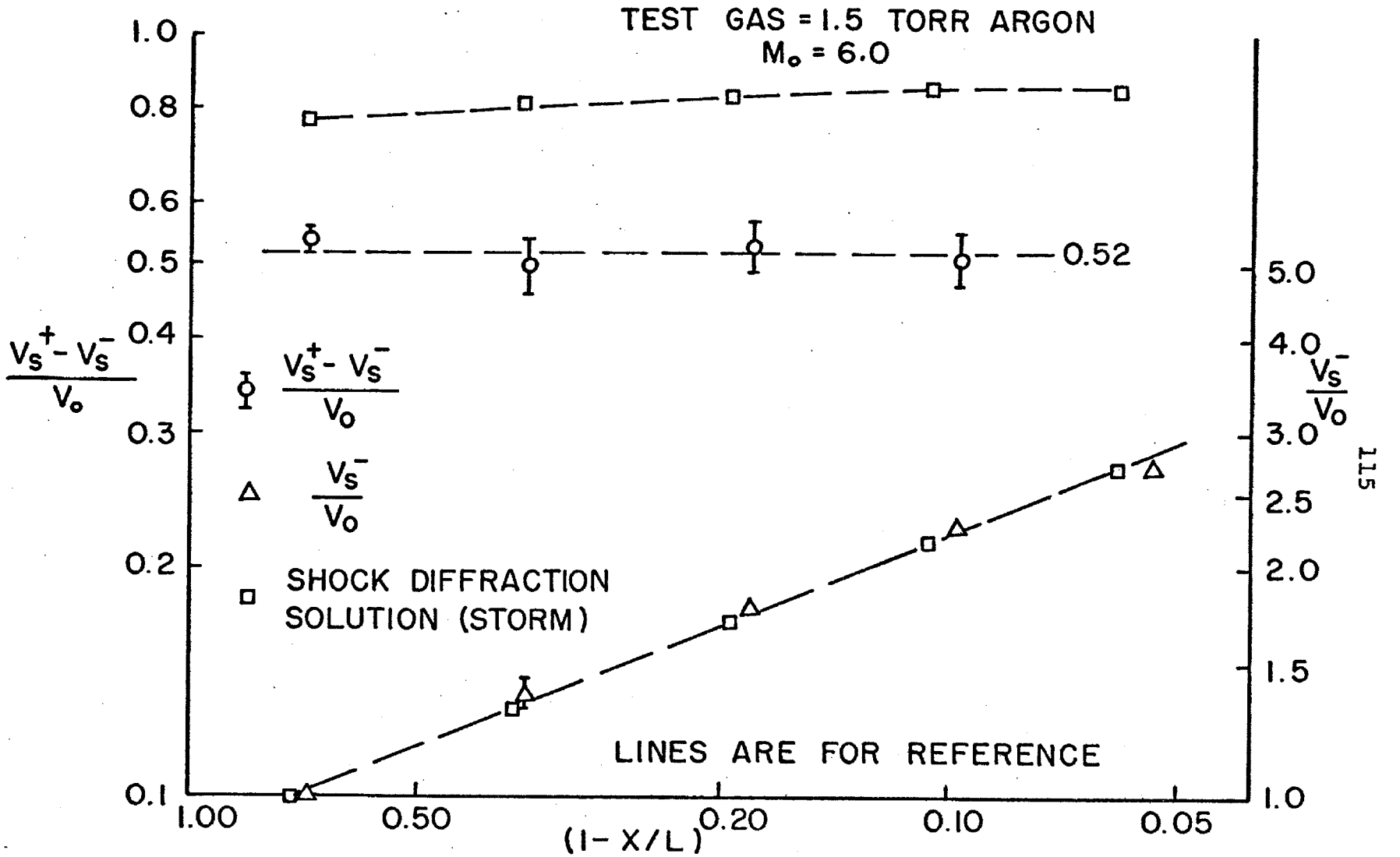

Figure 9. M_o = 6.0 Centerline Shock Velocity Jumps

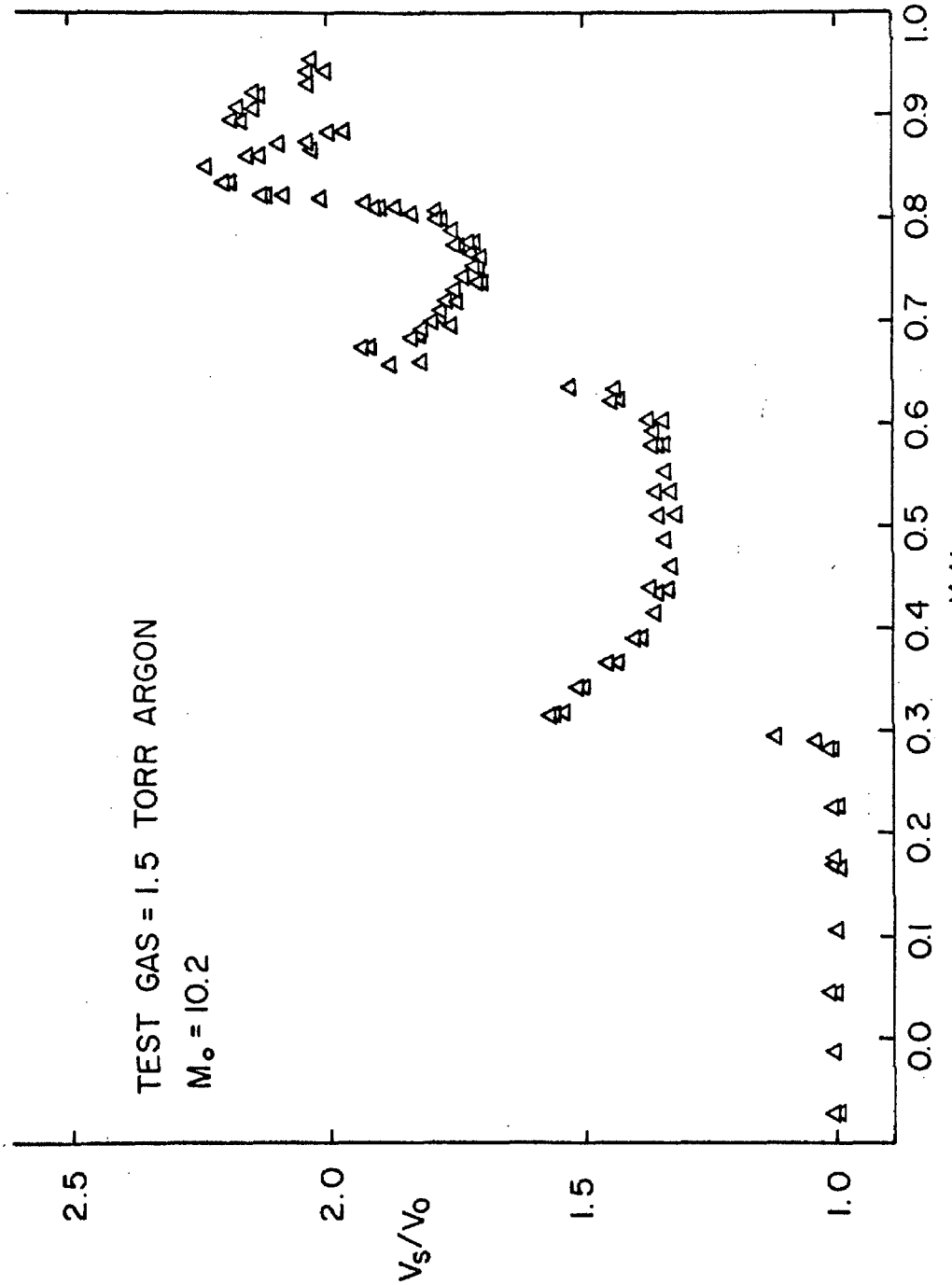

Figure 10. M_o = 10.2 Incident Shock Velocity

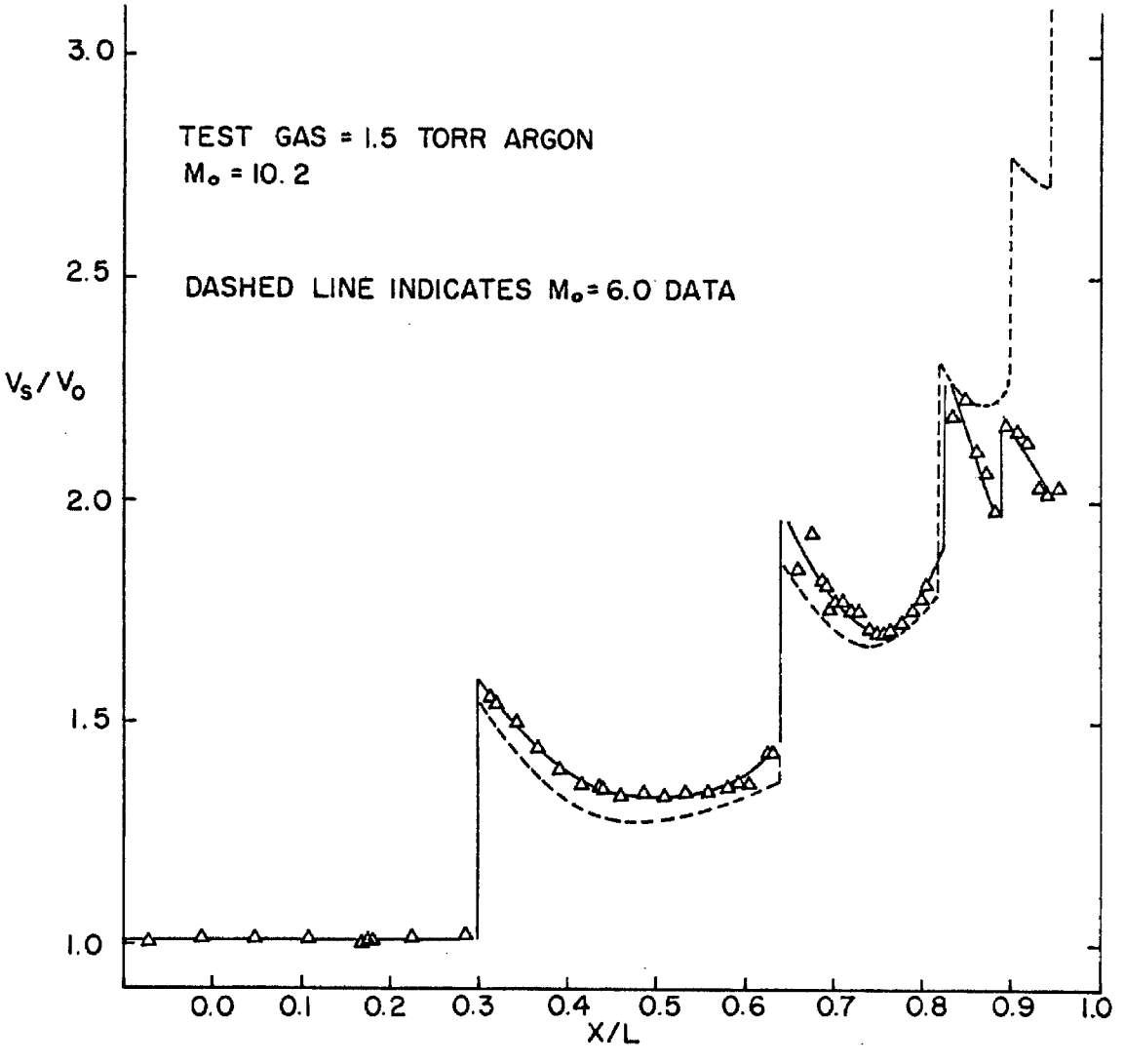

Figure 11. M_O = 10.2 Incident Shock Velocity and Stemshock Intersection Points

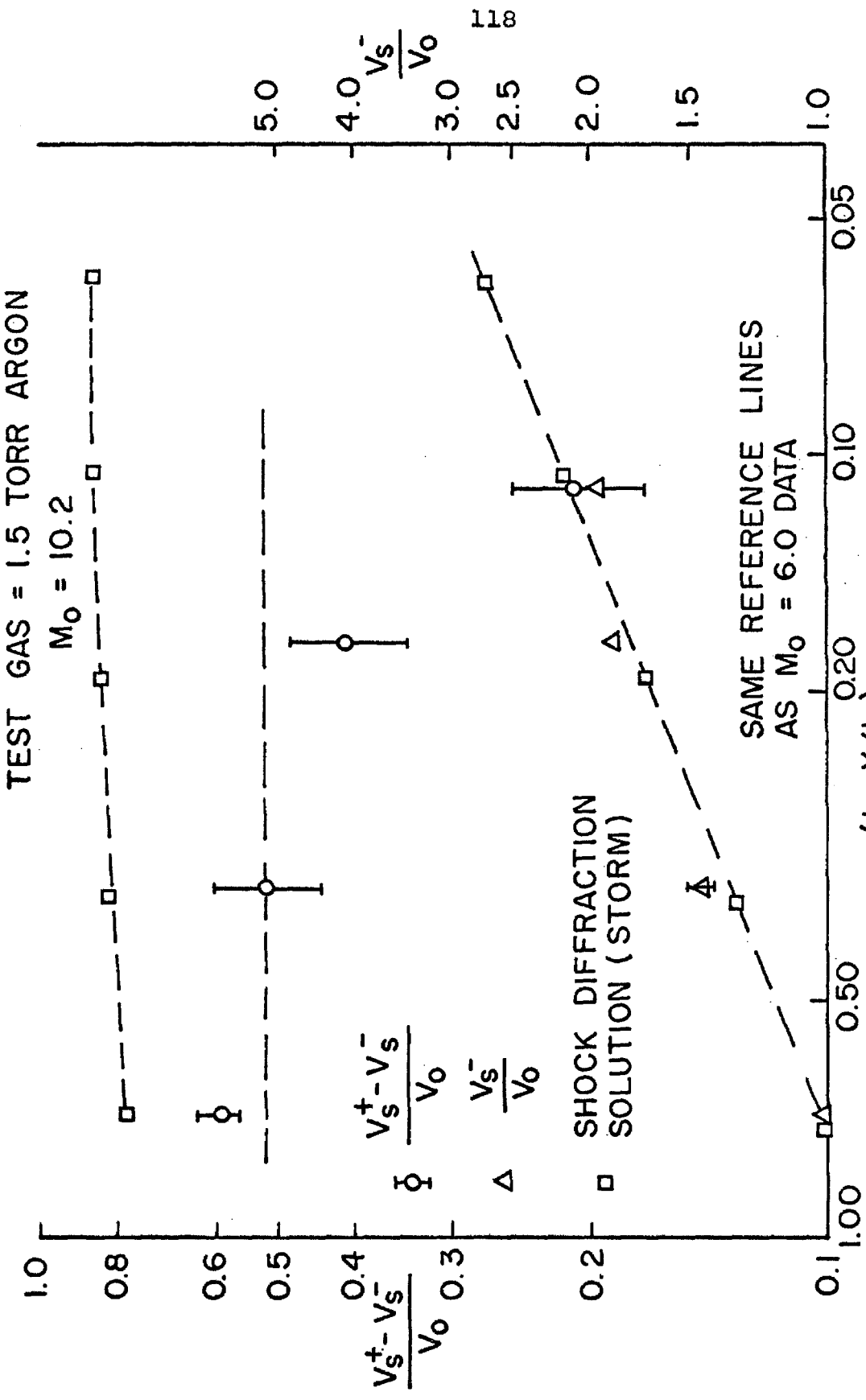

Figure 12. M_o = 10.2 Centerline Shock Velocity Jumps

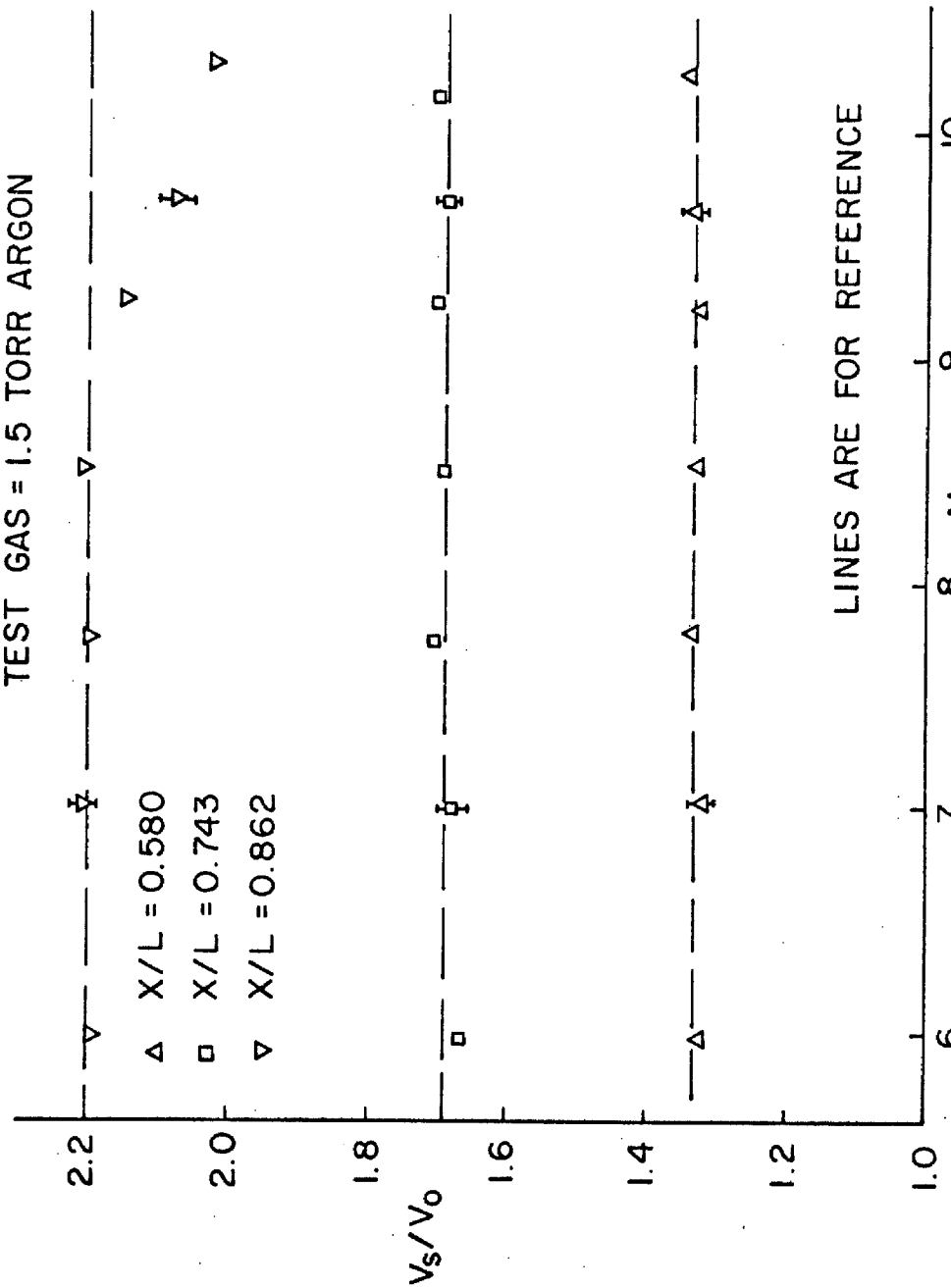

Figure 13. Effect of Varying Initial Mach Number (Initial Pressure 1.5 Torr)

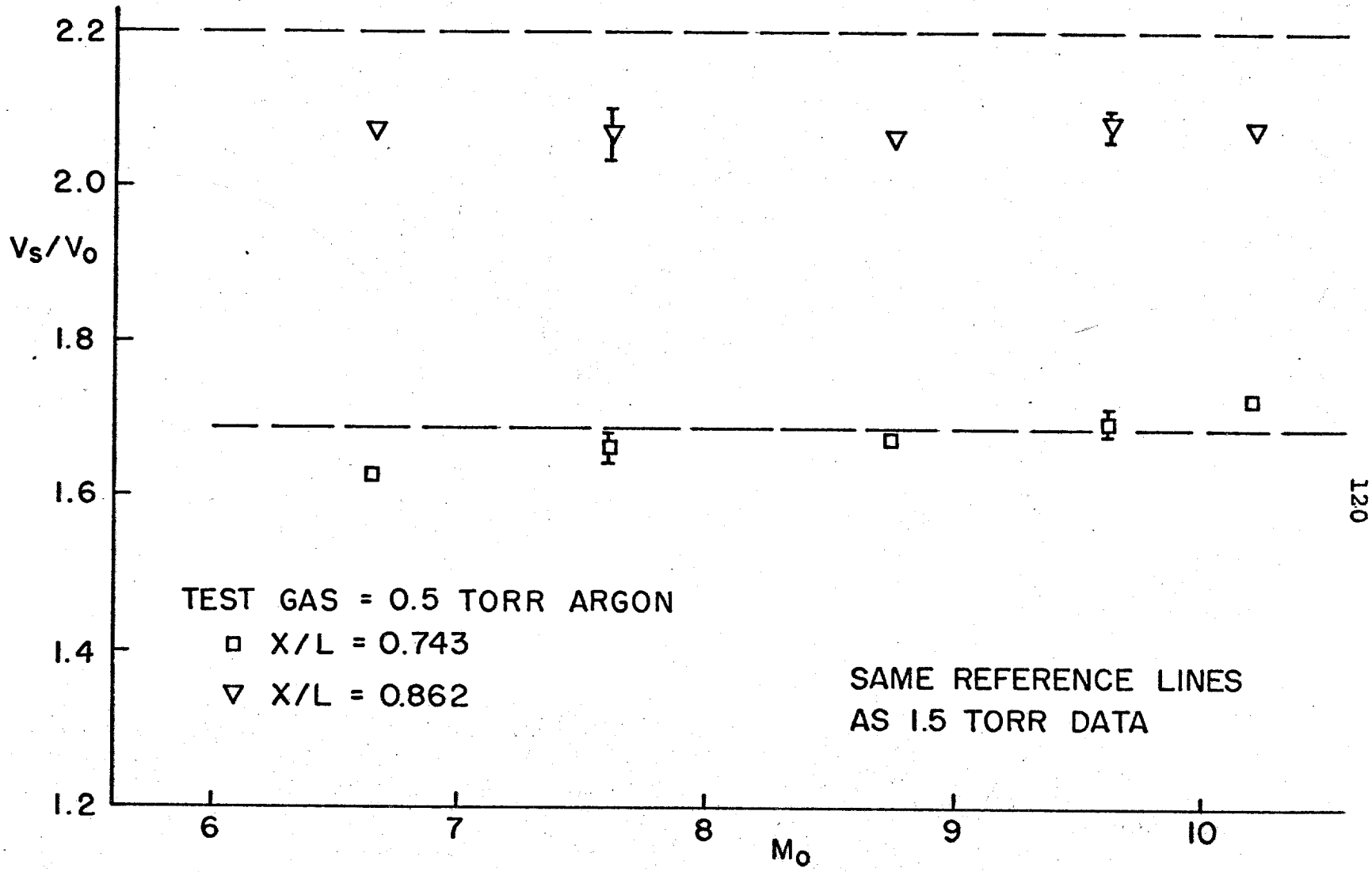

Figure 14. Effect of Varying Initial Mach Number (Initial Pressure 0.5 Torr)

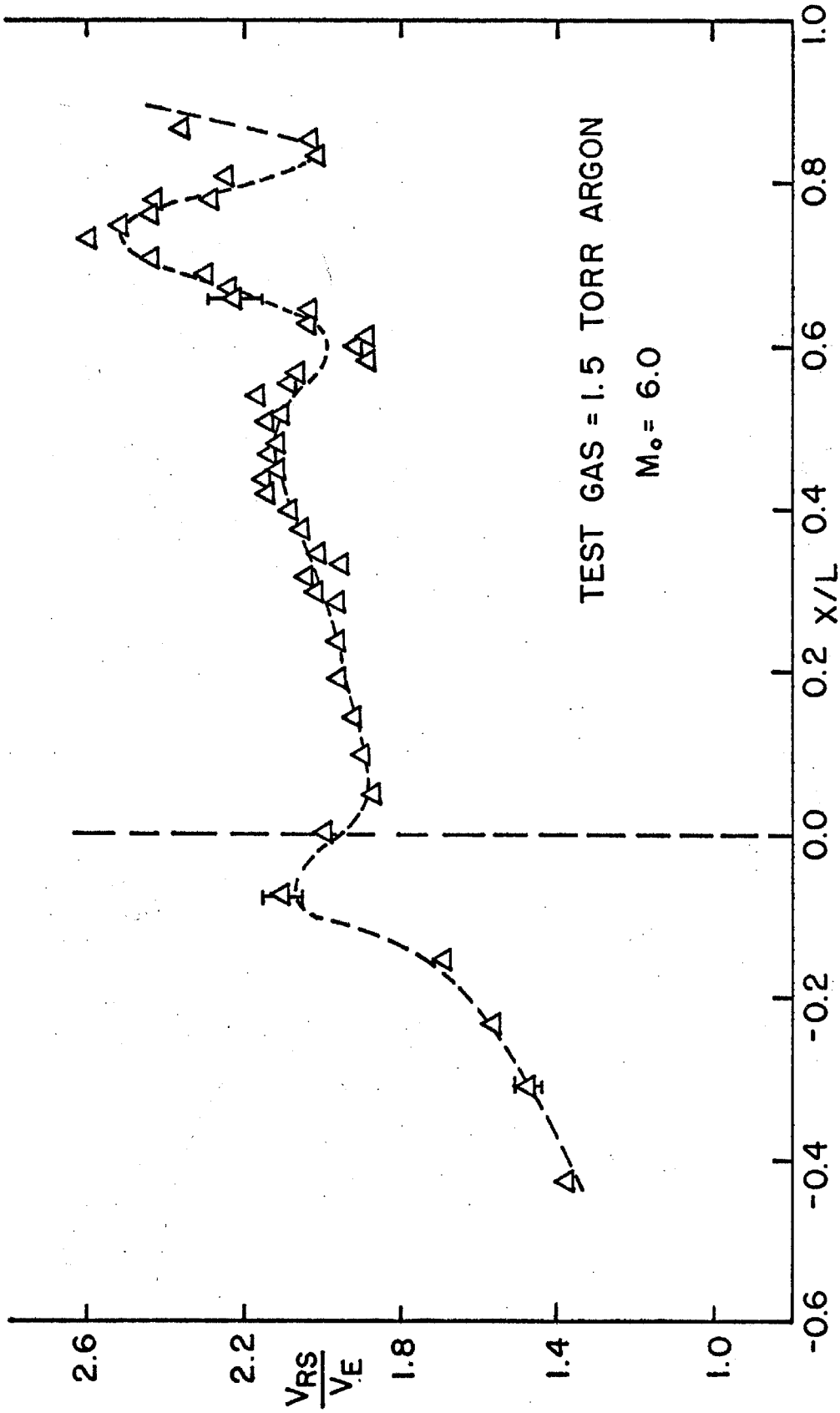

Figure 15. M_o = 6.0 Reflected Shock Velocity

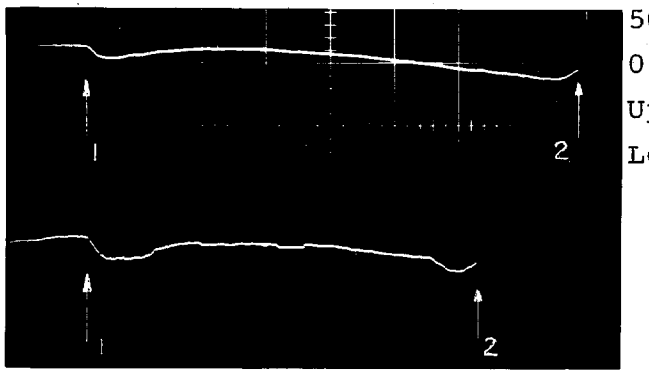

50μsec/div.
0.005v/div.
Upper beam: gauge B
Lower beam: gauge A

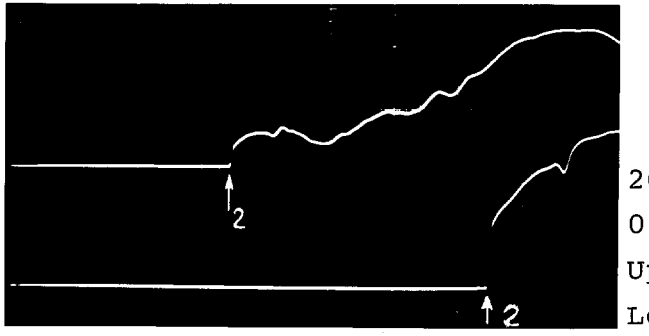

20μsec/div.
0.05v/div.
Upper beam: gauge A
Lower beam: gauge B

1: Signal Caused by Radiation from Cone Vertex
2: Reflected Shock

Figure 16a. Response of Thin Film Gauges to M_o = 6.0 Reflected Shock

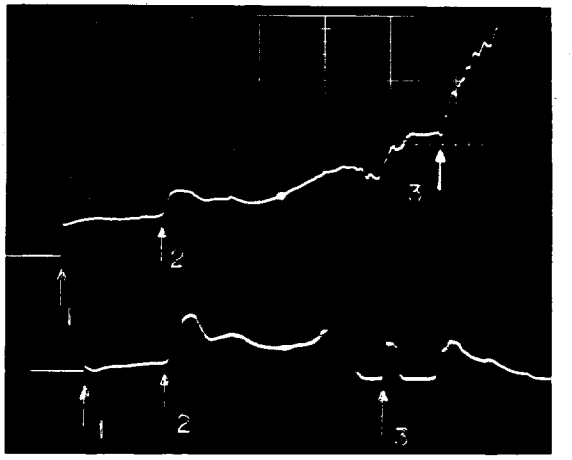

100μsec/div.
0.5v/div.
Upper: gauge B
Lower: gauge A

1: Incident Shock
2: Signal Caused by Radiation from Cone Vertex
3: Reflected Shock

Gauge A: 13.3cm from Cone Entrance
Gauge B: 23.3cm from Cone Entrance

Figure 16b. M_o = 10.2 Thin Film Gauge Responses

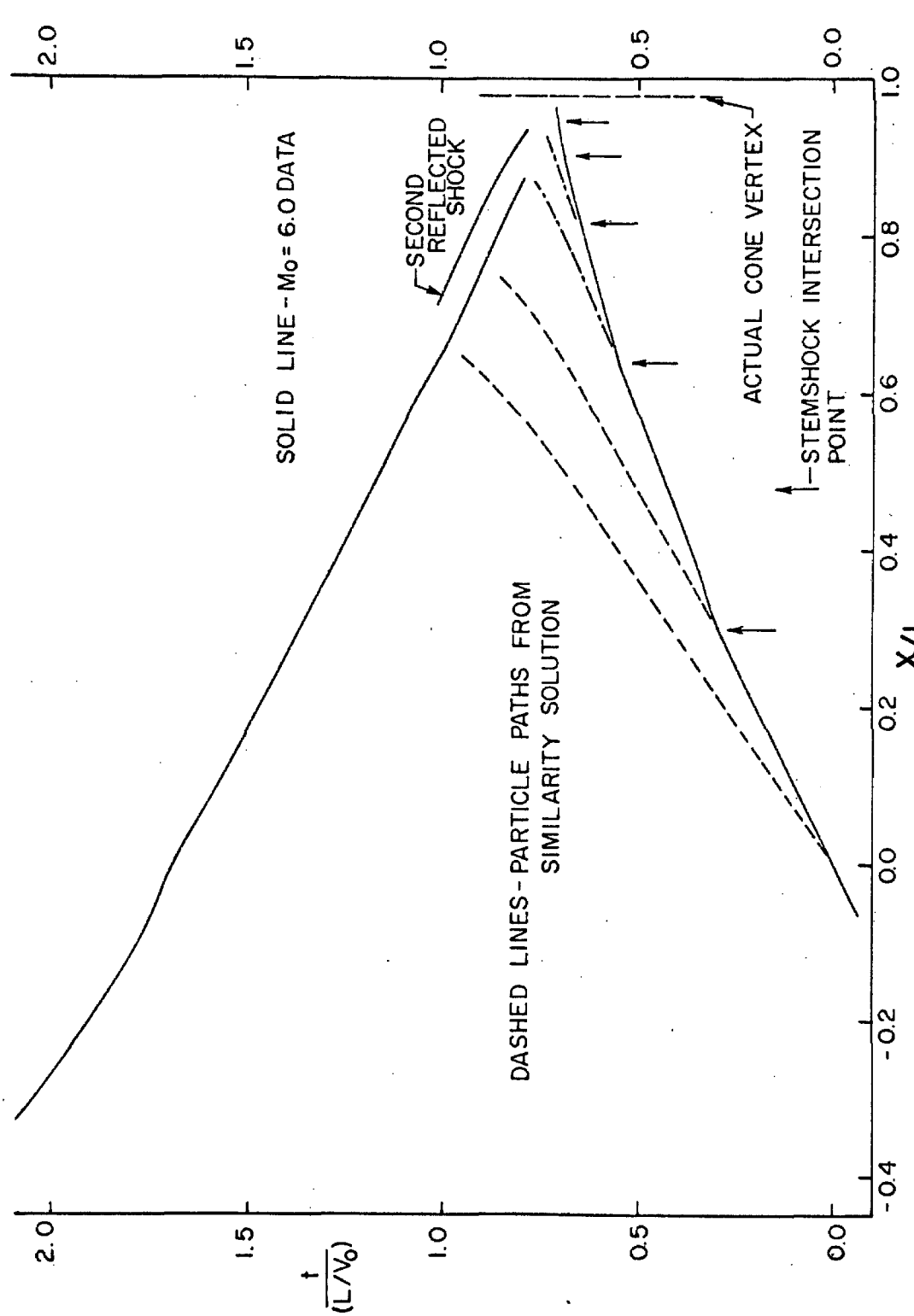

Figure 17. M_o = 6.0 Incident and Reflected Shock Trajectories

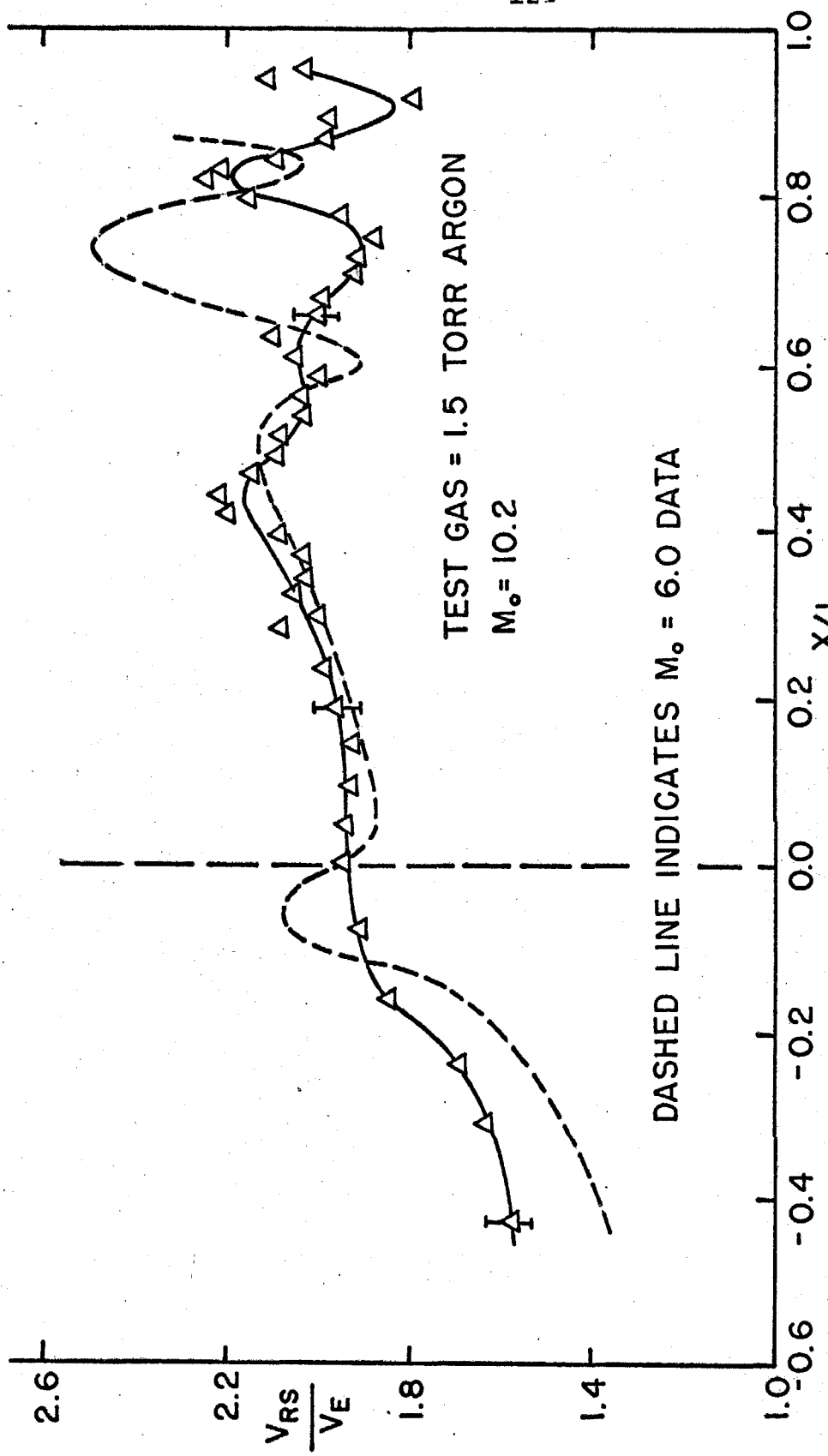

Figure 18. M_o = 10.2 Reflected Shock Velocity

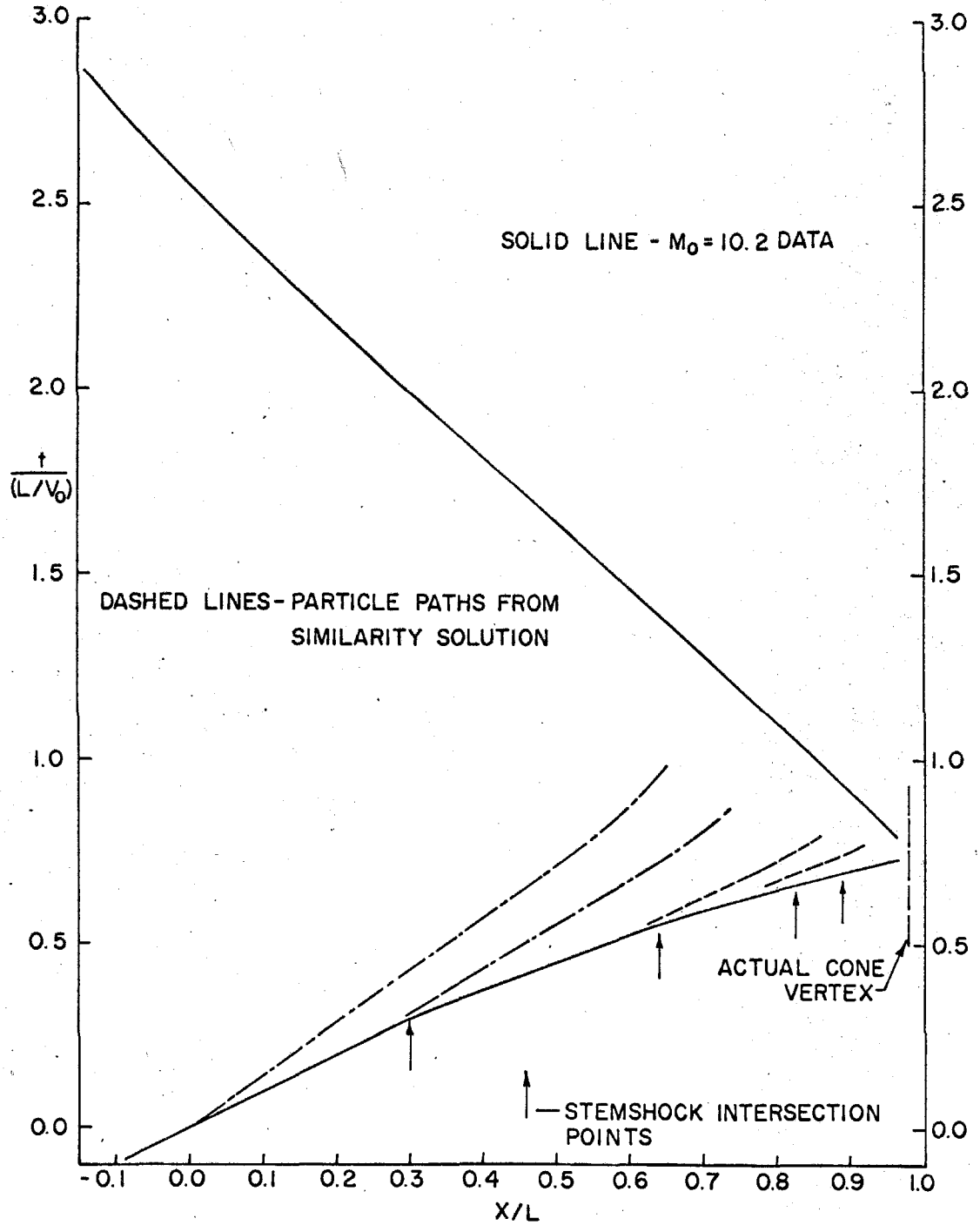

Figure 19. M_o = 10.2 Incident and Reflected Shock Trajectories

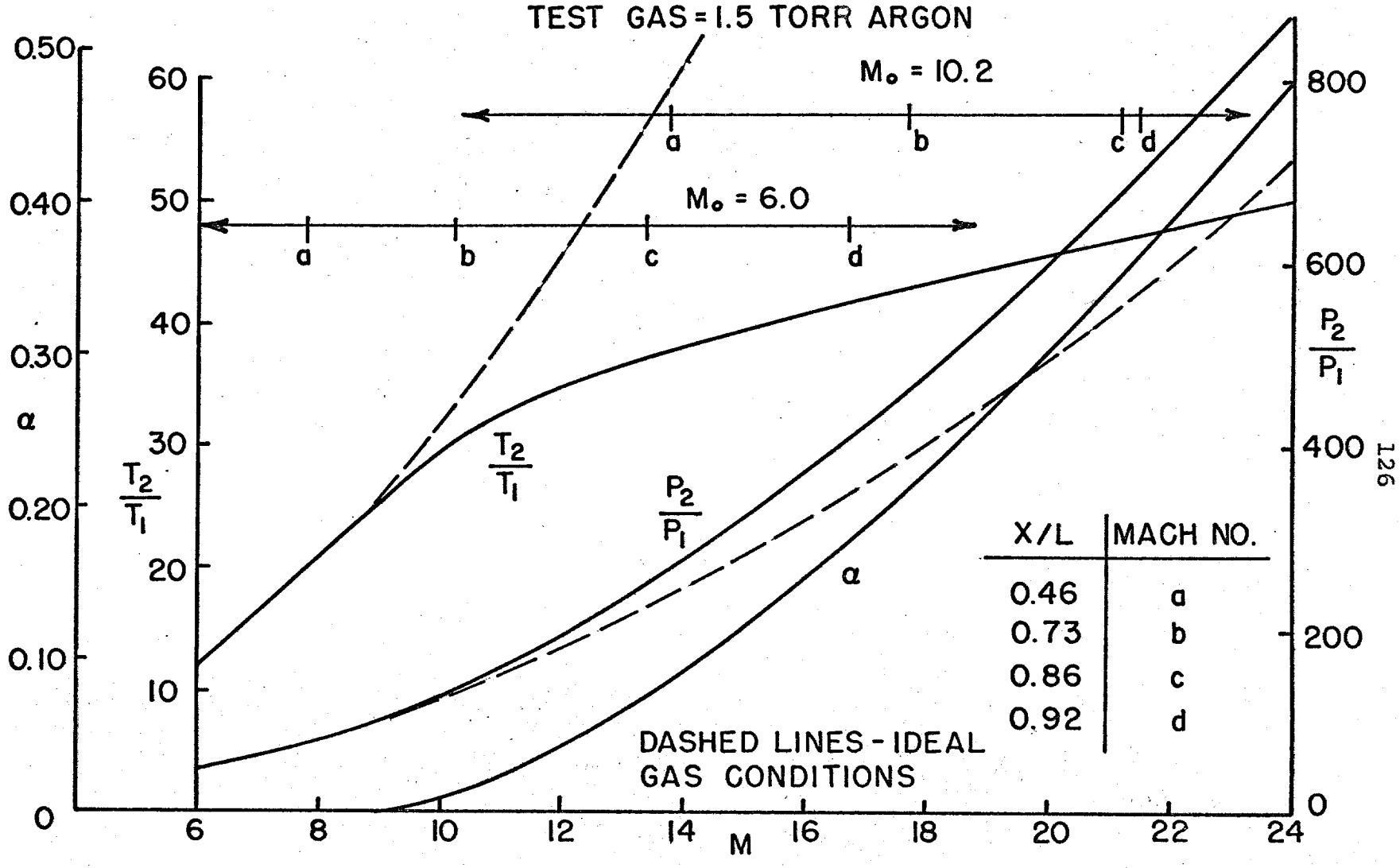

Figure 20. Equilibrium Conditions Behind Normal Shock Waves in Argon

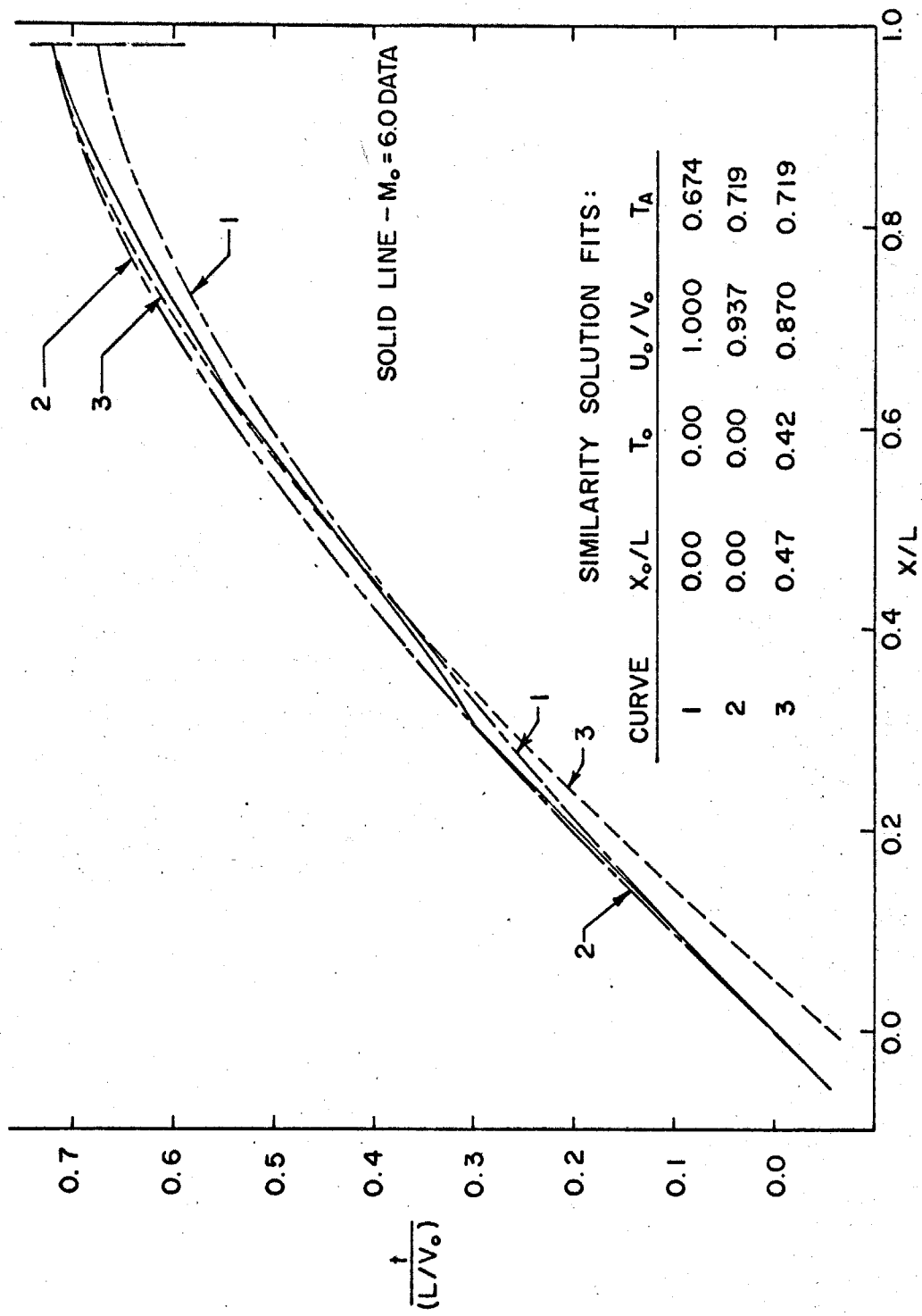

Figure 21. Similarity Solution Fits to the M_o = 6.0 Incident Shock Data

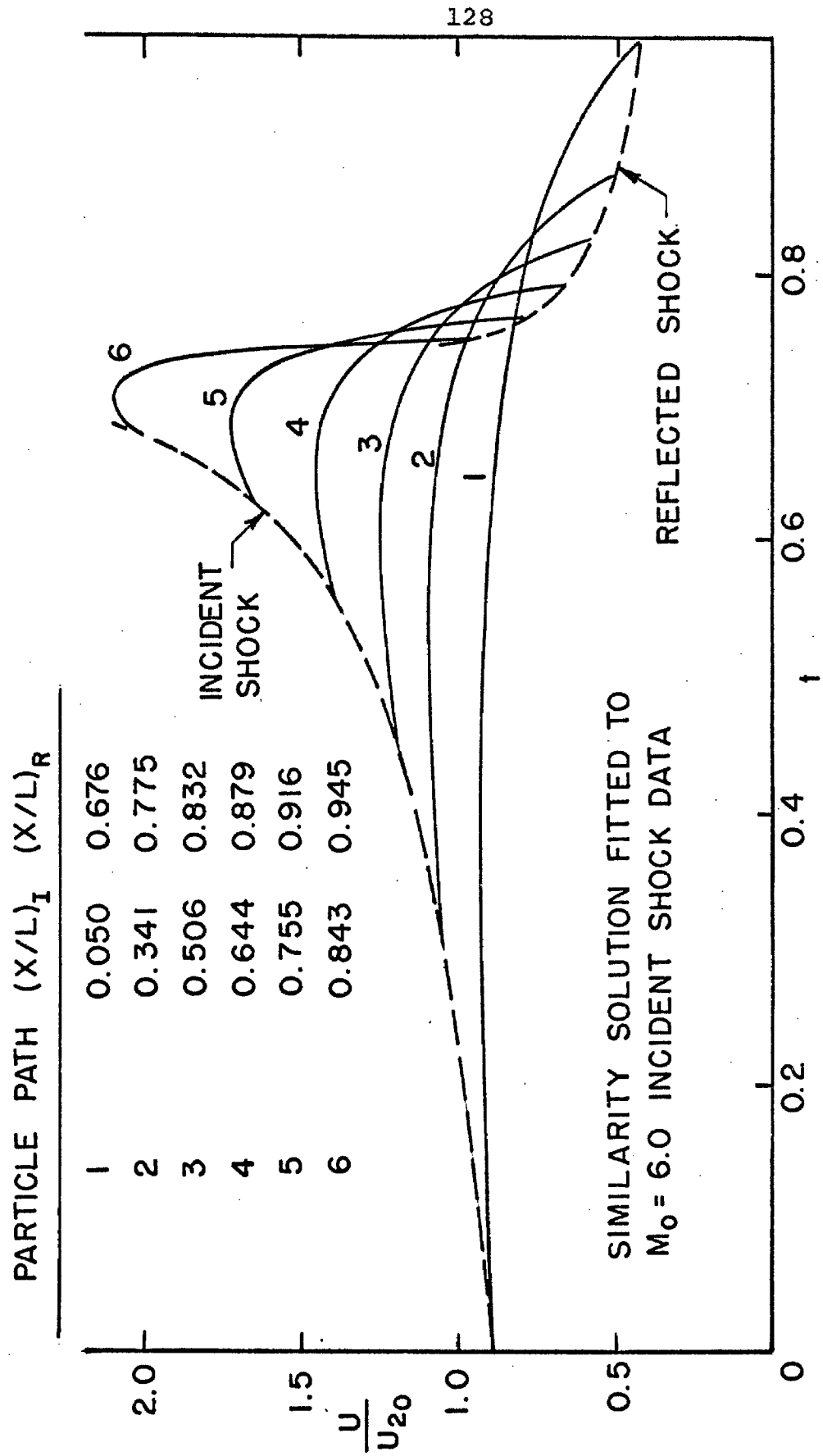

Figure 22. Fluid Velocity Along Particle Paths

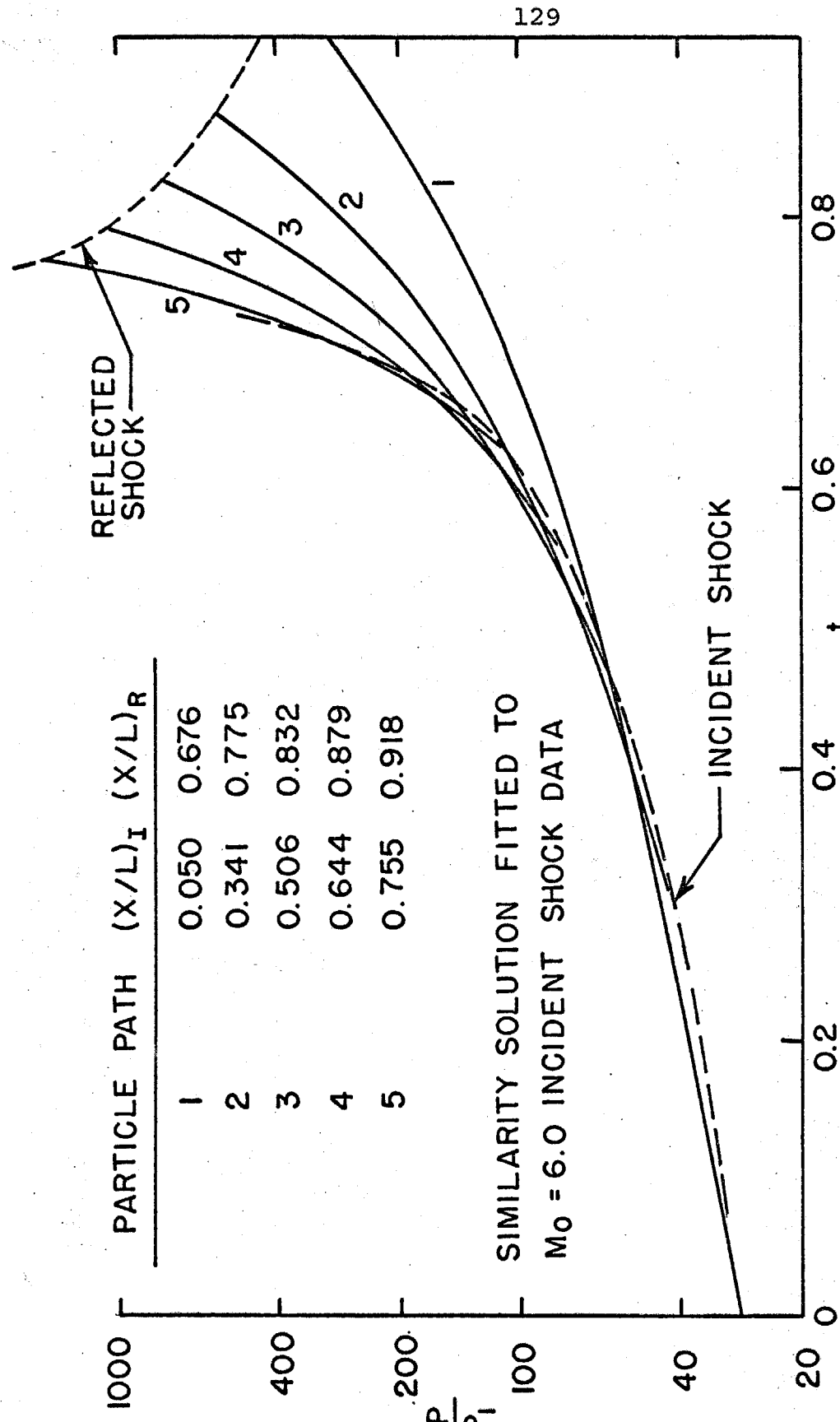

Figure 23. Fluid Pressure Along Particle Paths

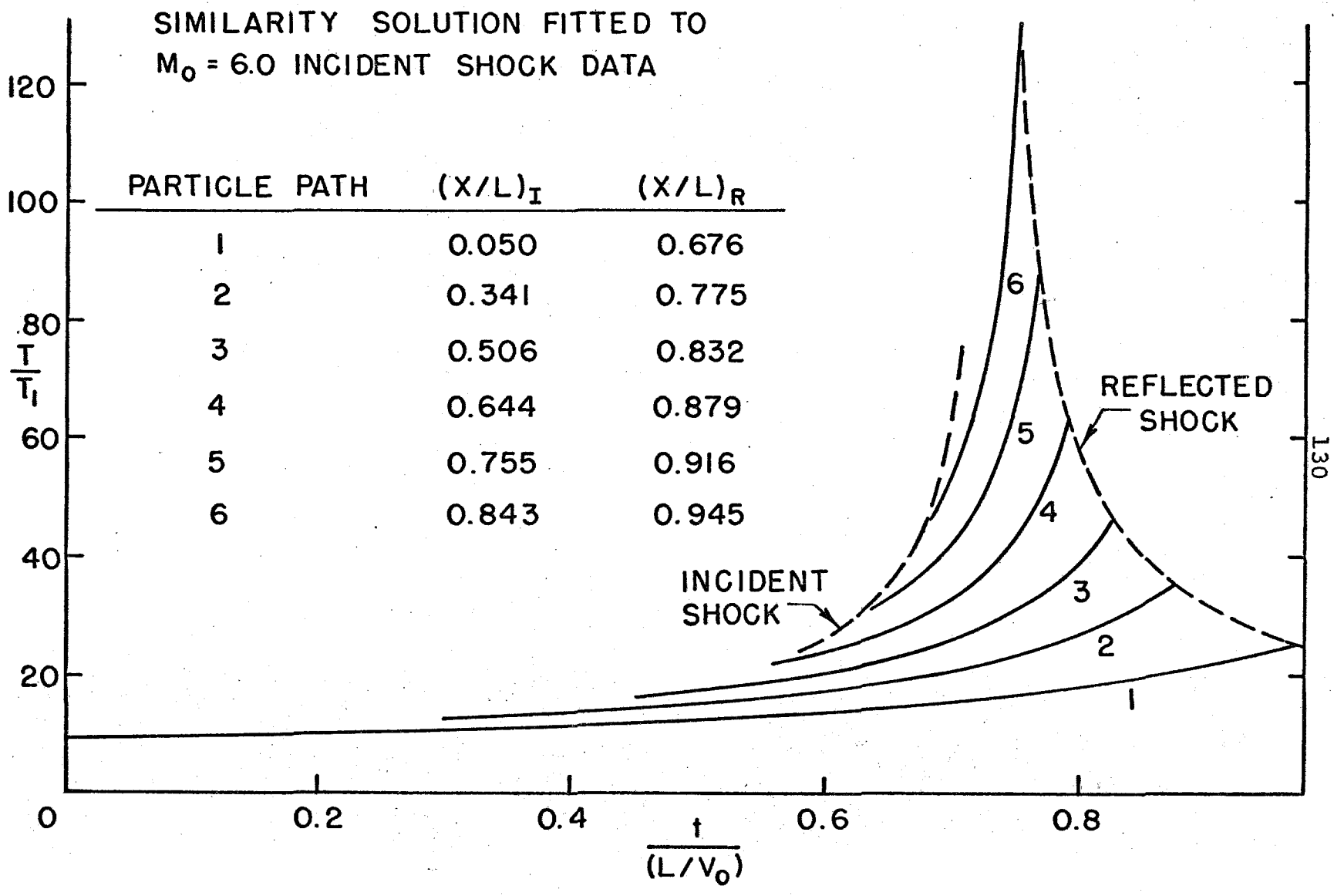

Figure 24. Fluid Temperature Along Particle Paths

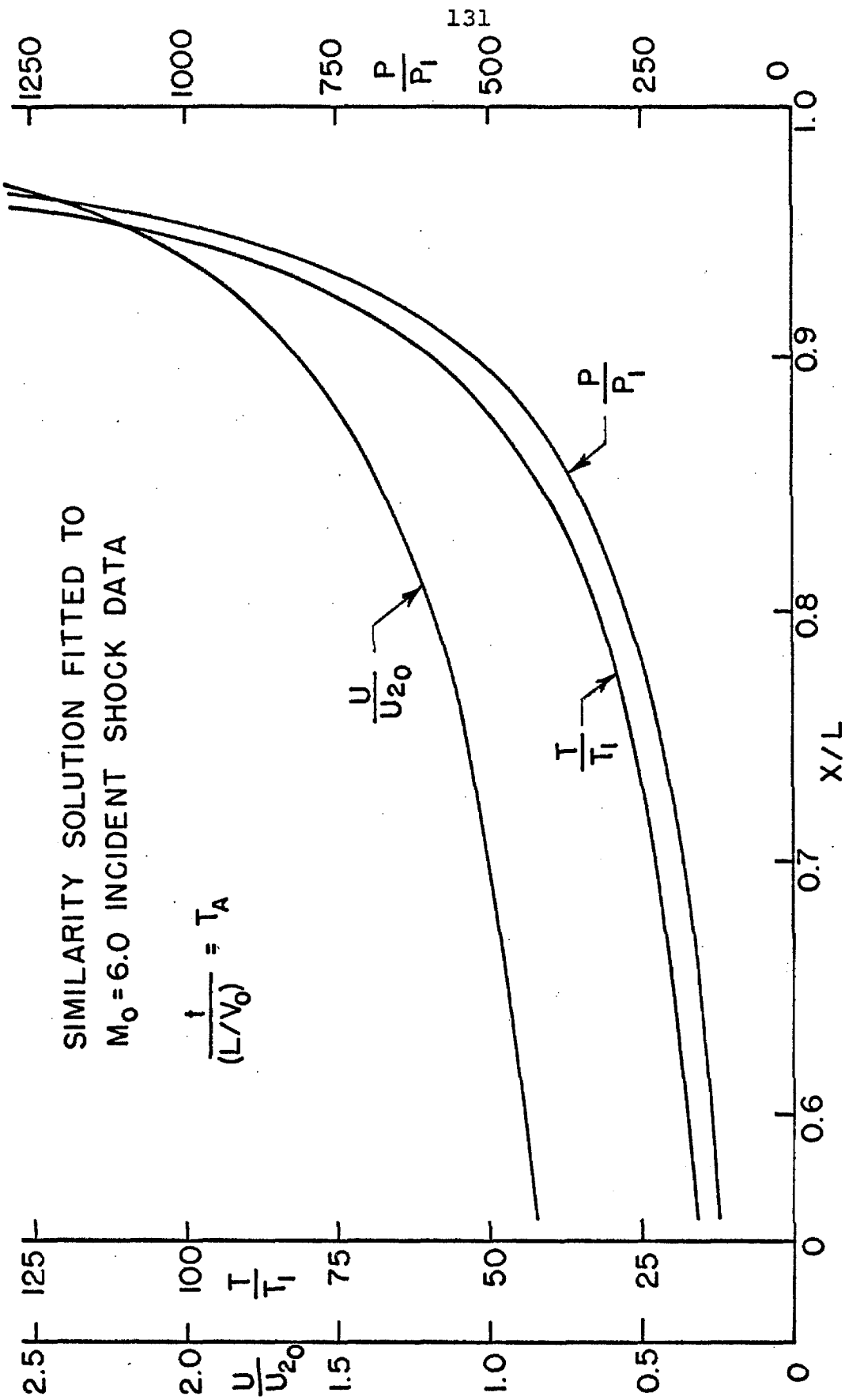

Figure 25. Fluid Velocity, Pressure, and Temperature Profiles When the Incident Shock Reaches the Cone Vertex

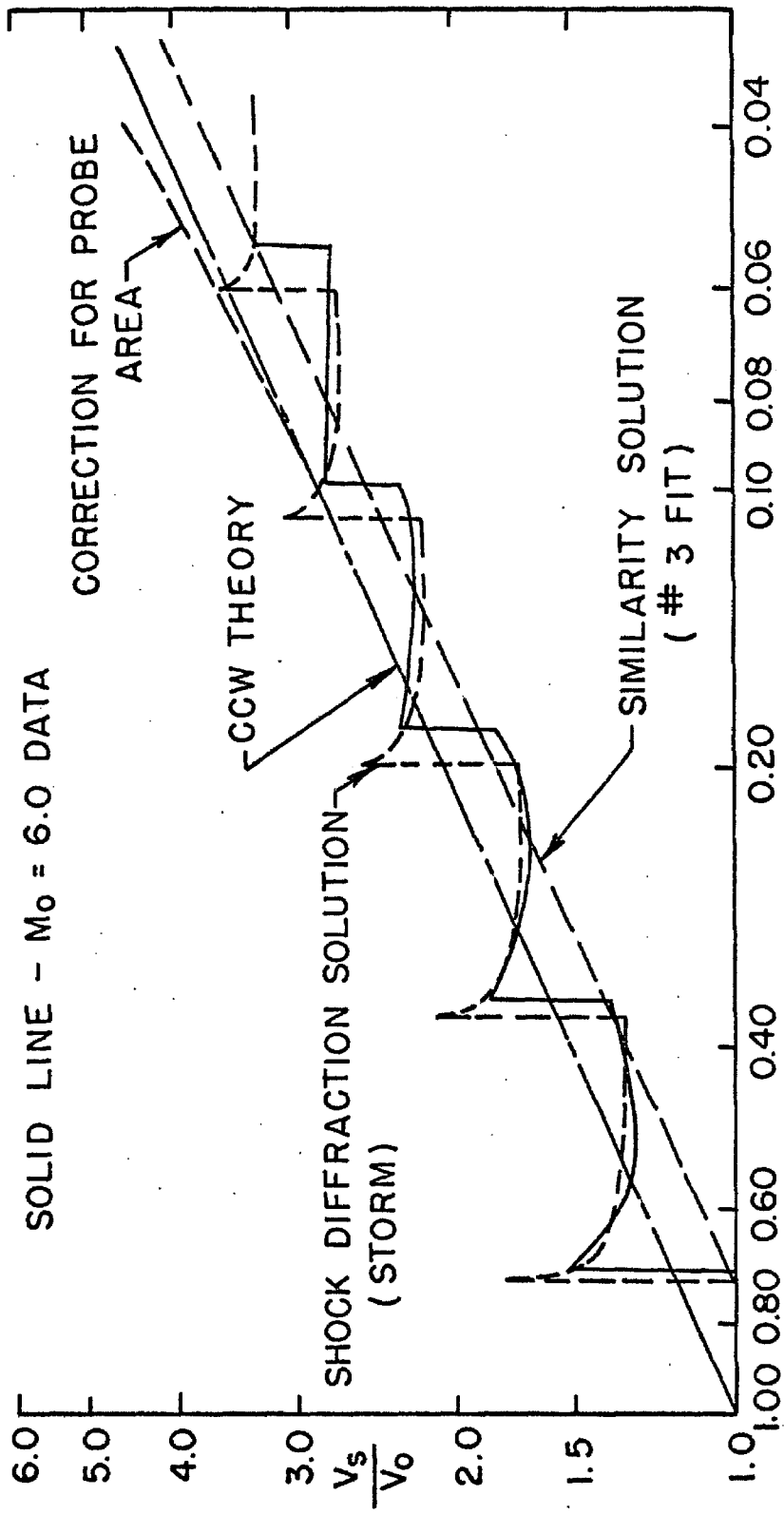

Figure 26. Comparison of M_ρ = 6.0 Incident Shock Data with Theoretical Predictions

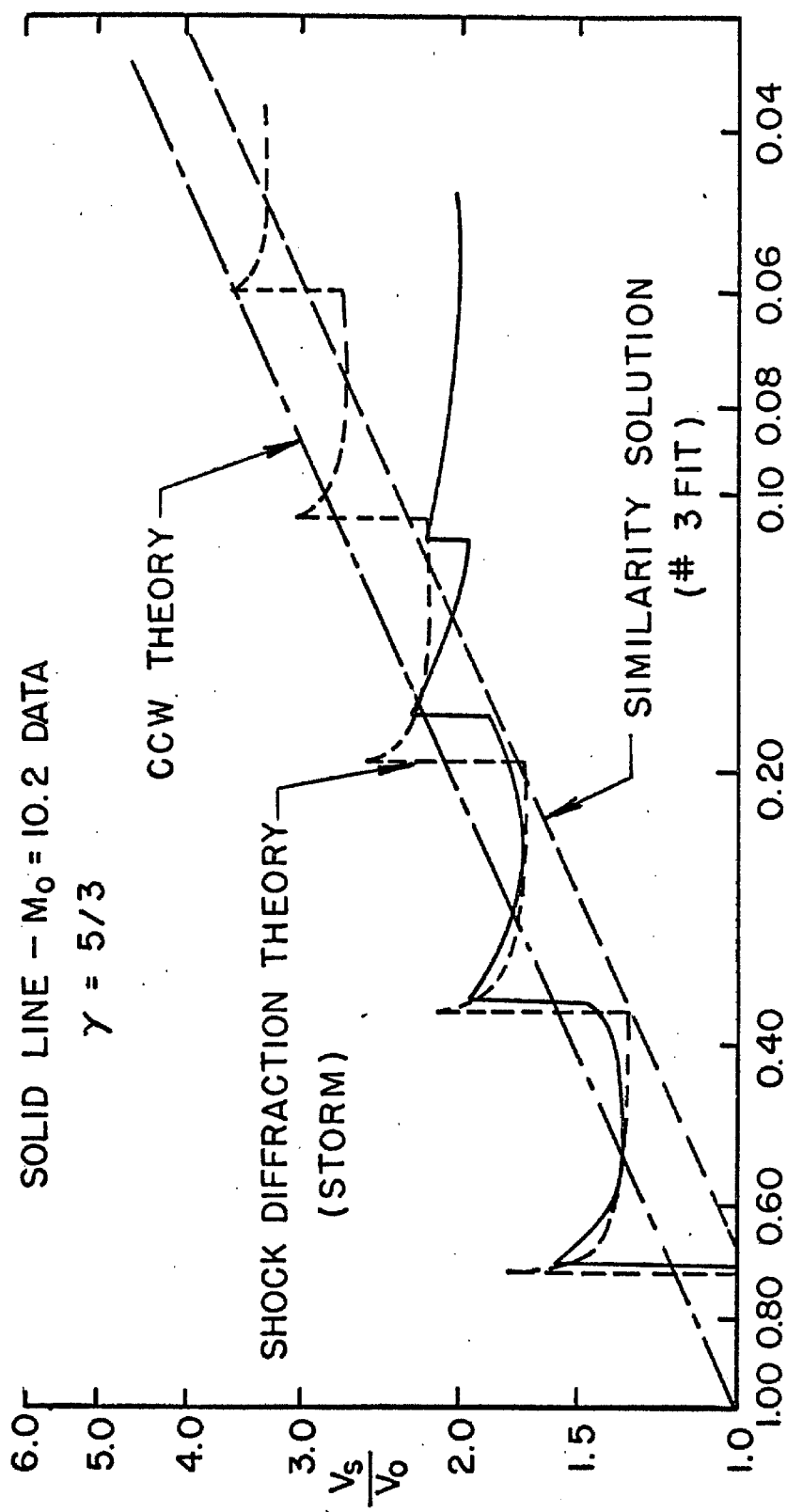

Figure 27. Comparison of M_o = 10.2 Incident Shock Data with Theoretical Predictions

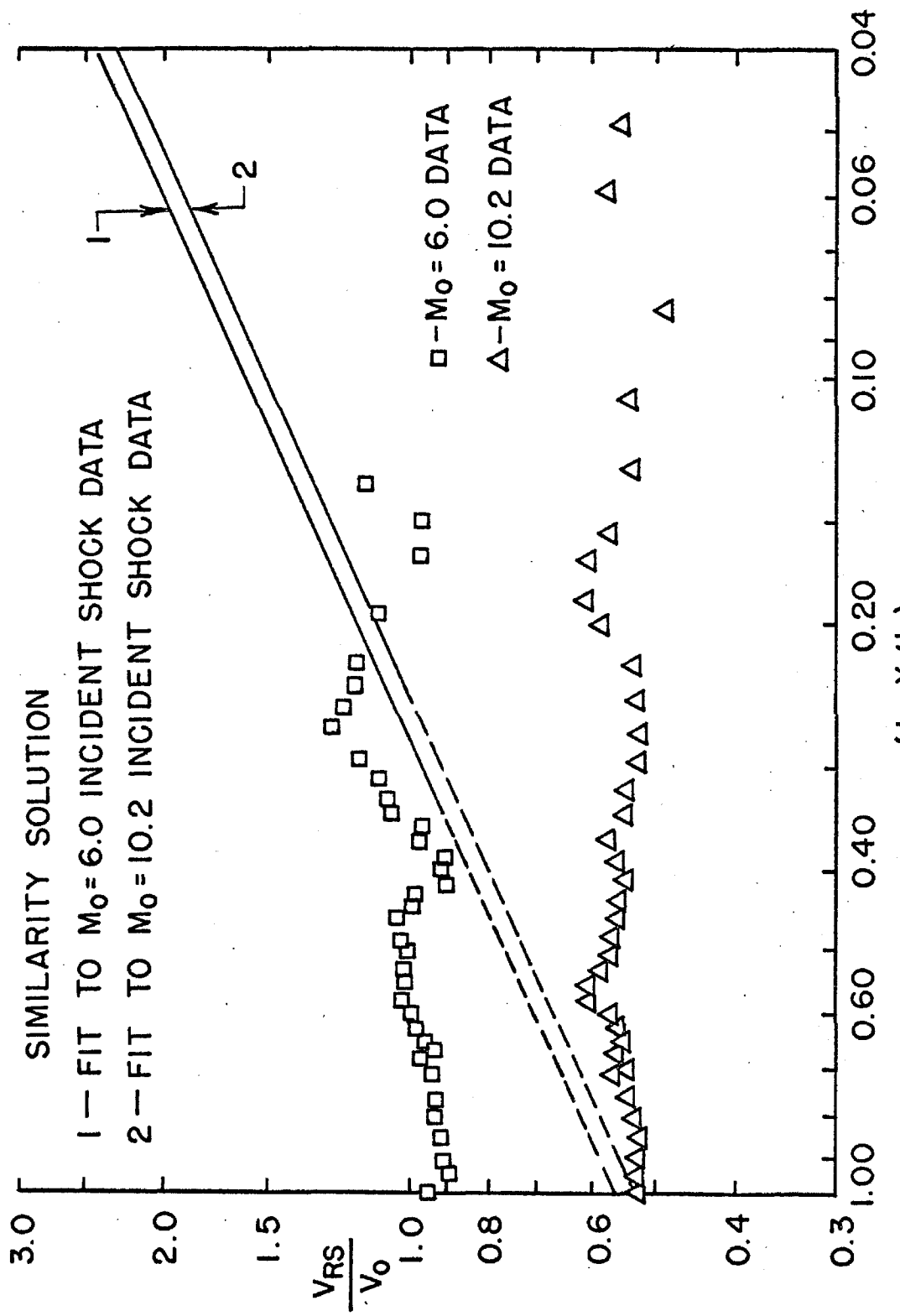

Figure 28. Comparison of Reflected Shock Data with Similarity Solution

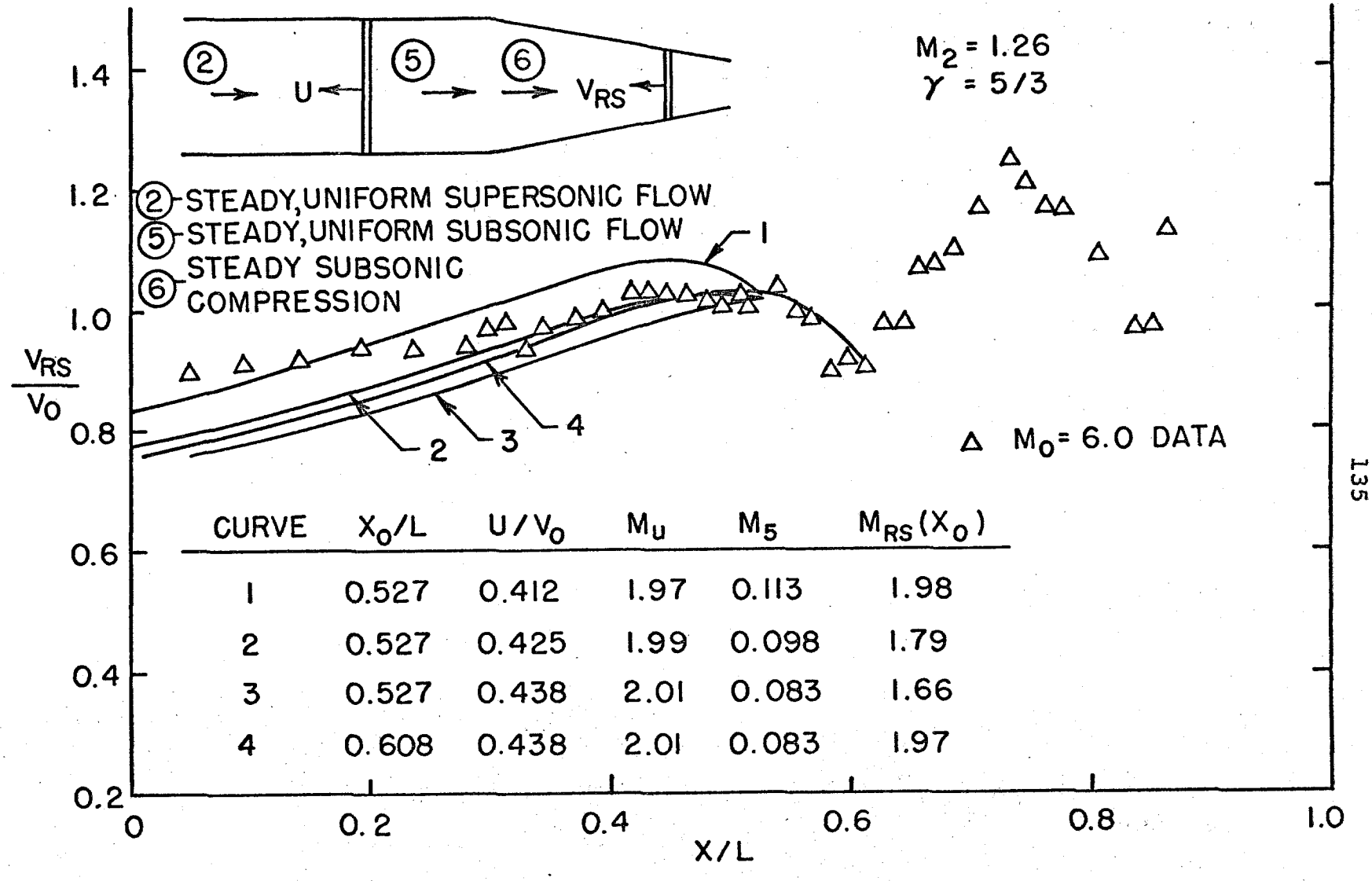

CURVE	X_0/L	U/V_0	M_u	M_5	$M_{RS}(X_0)$
1	0.527	0.412	1.97	0.113	1.98
2	0.527	0.425	1.99	0.098	1.79
3	0.527	0.438	2.01	0.083	1.66
4	0.608	0.438	2.01	0.083	1.97

Figure 29. Reflected Shock Propagating Into a Steady, Subsonic Flow

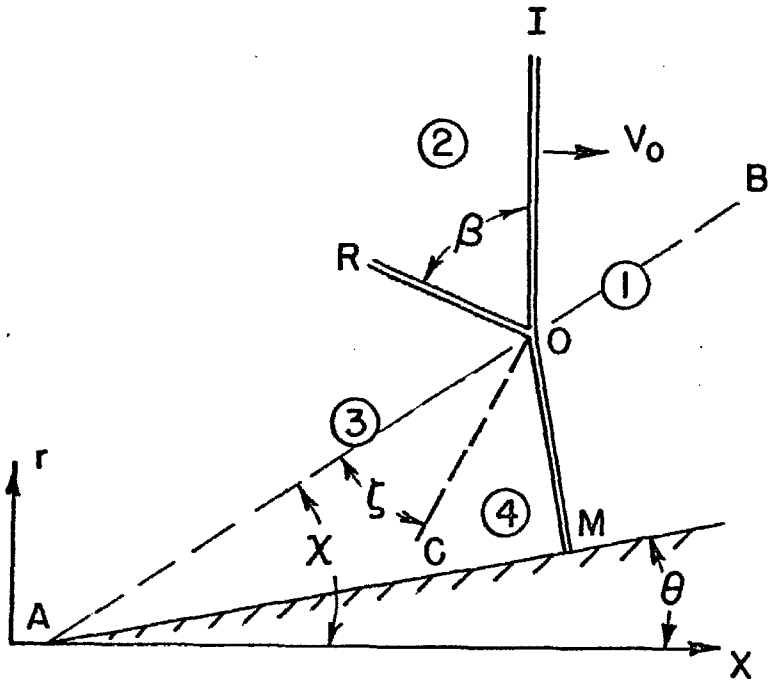

Figure 30.
Two-dimensional Mach Reflection

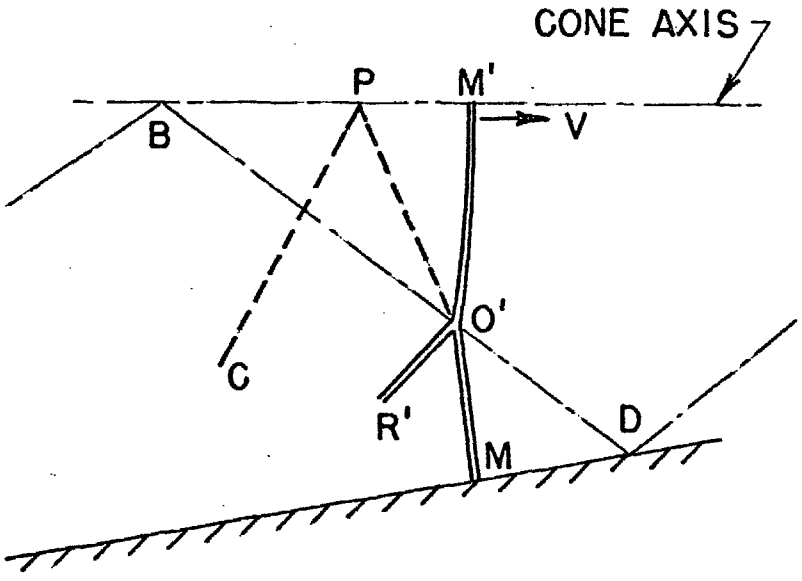

Figure 31.
Contact Surface Intersection Point